WIDE-BAND-GAP II-VI SEMICONDUCTOR HETEROSTRUCTURE MODELING AND DEVICE DESIGN

Yijun Cai

B.S. (Physics), Peking University, Beijing, China, 1986

M.S. (E.E.), Oregon Graduate Institute of Science & Technology,

Beaverton, Oregon, 1994

A dissertation submitted to the faculty of the
Oregon Graduate Institute of Science & Technology
in partial fulfillment of the
requirements for the degree
Doctor of Philosophy
in
Electrical Engineering

January 1996

The dissertation "Wide-band-gap II-VI semiconductor heterostructure modeling and device design" by Yijun Cai has been examined and approved by the following Examination Committee.

Dr. Reinhart Engelmann, Dissertation Advisor
Professor, Oregon Graduate Institute

Dr. Raj Solanki
Associate Professor, Oregon Graduate Institute

Dr. V. S. Rao Gudimetla
Assistant Professor, Oregon Graduate Institute

Dr. Peter S. Zory, Jr.
Professor, University of Florida

To

Uncle Yoxing

Acknowledgments

First, I would like to express my gratitude to my supervisor, Dr. Reinhart Engelmann, for guidance and supporting me to undertake this research. Our many discussions and his thoughtful commentary have not only enhanced my technical knowledge but also influenced the aspects of life beyond academics.

I wish to thank Dr. Raj Solanki and Dr. Rao Gudimetla for participation on my examination committee and their valuable time and comments.

It is a pleasure to thank Dr. Peter Zory for valuable and informative discussions regarding various technical problems in the project as well as for his efforts of serving on my examination committee. This work was mainly supported by ARPA/ONR through a sub-contract with the University of Florida. I also wish to thank other colleagues at the University of Florida, including Dr. R. Park and Dr. P. Holloway for their encouragement during our several pleasant contacts.

I am indebted to Dr. Nu Yu and Dr. J. Ebner for their initiative effort on the gain modeling program; to Claus Fischer of the Technical University Vienna, Austria, for courtesy of HEMT simulator; to Dr. Gary Evans of the Southern Methodist University, for courtesy of MODEIG software. I appreciate Dr. Rich DeFreez for laser lab training and helps on wave guide modeling. I thank Dr. Craig Wilson of SILVACO International for technical support of ATLAS.

I express many thanks to the faculties, T. Bell, J. Orloff and J. Parsons; the fellow students, S. Ahmed, C. Barbero, F. Chen, C. Deng, J. Ferguson, W. Kong, K. Otis, B. Rask, and C. Zhao; and secretary B. Olsen of EEAP department of OGI, for their assis-

tance and collaboration during my graduate studies. In particular, I have benefited greatly from the after-work basketball games at OGI, which have been a great source of fun, joy and energy.

Very special thanks go to my wife Zhihong for her love, patience and understanding, to our parents for their many years of support and encouragement which have helped bring me to this point.

Table of Contents

List of Tables

List of Figures

List of Symbols

a	Lattice constant of bulk material.
a_c, a_v	Hydrostatic deformation potential for conduction and valence band.
B	Radiative recombination constant.
b	Bowing parameter.
b_v	Shear deformation potential.
C_{ij}	Elastic moduli.
d	Tetrahedral band length.
$\mathbf{E}$	Electrical field.
E	Energy.
E_A	Activation energy of acceptor.
E_D	Activation energy of donor.
E_F	Fermi-energy.
E_g	Band gap energy.
G	Generation rate of carriers.
G_m	Mode gain of longitudinal mode m.
g	Local optical gain.
g_A	Degeneracy factor for valence band.
g_D	Degeneracy factor for conduction band.
h	Planck's constant, $6.626 \times 10^{-34} \mathrm{J} \cdot \mathrm{s}$.
$\mathbf{J}_i$	Current density, i = n for electron, i = p for hole.
k_B	Boltzmann's constant.
L	Laser diode cavity length.

L_{qw}	QW thickness.
L_{ba}	Barrier thickness.
m_i	Effective mass of electron (i = e), heavy hole (i = hh) and light hole (i = lh).
m_o	Electron rest mass, 9.100×10^{-31}kg.
n	Free carrier (electron) density or refractive index.
N_c	Critical dopant density of impurity conduction.
p	Free carrier (hole) density.
q	Electron charge.
Q_c	Conduction band offset ratio.
r	Tetrahedral covalent radii.
$R_{r,nr}$	Radiative (r) and non-radiative (nr) recombination rates of carriers.
R_L	Total cavity loss.
S_m	Photon density of longitudinal model m.
T	Temperature.
x	Mole fraction of element in alloy.
α	Broadening factor.
α_H	Hydrogenic Bohr radii.
α_m	Mirror losses.
α_{int}	Internal losses.
ΔE_c	Conduction band offset.
ΔE_v	Valence band offset.
σ	Net space charge.
β	Effective wave factor.
Γ	Optical confinement factor.
γ_i	Luttinger parameters, i= 1, 2, 3.

μ_i	Mobility, i = e for electron and i = hh for heavy hole.
ω_m	Angular frequency of longitudinal mode m.
ρ_i	Density of states function, i = n for electron, i = p for hole.
λ	Light wavelength.
ε_{ij}	Strain tensor, i, j = x, y, z.
ε_o	Static dielectric constant.
ε_∞	High frequency dielectric constant.
τ_i	Non-radiative minority carrier life time, i = n for electron, i = p for hole.
τ_s	Intraband relaxation time.

List of Acronyms

ALE	Atomic Layer Epitaxy
BA	Barrier Layer
CAD	Computer aided design
CW	Continuous Wave
DD	Drift/diffusion
DH	Double hetero (structure)
HBT	Heterojunction Bipolar Transistor
HEMT	High Electron Mobility Transistor
II-VI	Two-Six Compounds
III-V	Three-Five Compounds
LD	Laser diode
LED	Light emitting diode
MBE	Molecular Beam Epitaxy
MOVPE	Metal-Organic Vapor Phase Epitaxy
QW	Quantum Well
RF	Radio frequency
RT	Room Temperature
SCH	Separate confinement heterostructure
UV	Ultra violet
WZ	Wurtzite
ZB	Zinc blende
1-D	One-Dimensional
2-D	Two-Dimensional

ABSTRACT

WIDE-BAND-GAP II-VI SEMICONDUCTOR HETEROSTRUCTURE MODELING AND DEVICE DESIGN

Yijun Cai

Supervising Professor: Reinhart Engelmann

This dissertation is about the design and simulation of wide-band-gap II-VI heterostructure devices. Particular interest has been placed on design and modeling of a quantum-well (QW) laser diode, which is now the major driving force of the investigation on the wide-band-gap II-VI materials. The potential of wide-band-gap II-VI semiconductors for transistor application has also been explored. The material and heterojunction properties including strain effect have been evaluated and estimated based on the solid-state bond picture. A device simulation tool for QW lasers which combines physical and phenomenological methods involving different levels of physical approximations has been developed. For the QW region, where the quantum confinement effect is important and the optical field change can be neglected, a one-dimensional model based on solving the coupled Schrödinger and Poison equations is used. In this model, the long-range Coulomb interaction between electrons and holes can be taken into account through modeling the injection induced carrier confinement. For simplification of the numerical method, an effective-band-offset approach has been developed. The the bulk regions including cladding and

barrier, where quantum effect can be neglected and optical field change becomes significant, are analyzed using a modified two-dimensional drift-diffusion model including coupled Poisson and Helmholtz (Maxwell) equations. The quantum effect influence on gain and spontaneous recombination is incorporated by phenomenological parameters obtained from the QW model. The optimized structure parameters for low threshold current operation of gain-guided CdZnSe/ZnMgSSe based QW lasers have been obtained in a systematic way for a large range of compositions. A novel laser diode based on ZnMgSeTe has been proposed and designed for improving both p-type doping and Ohmic contact. For a possible future transistor application, a ZnS/Si heterojunction transistor has been proposed and simulated. The approach developed in this work can be also applied to other wide band-gap heterostructures.

Chapter 1 OVERVIEW

II-VI compounds in a broad sense include the compounds formed from elements of group IIa or IIb and group VI of the periodic table, encompassing the oxides, sulphides, selenides and tellurides of beryllium, magnesium, calcium, zinc, cadmium and mercury. For semiconductor applications, the general interests center around the sulphides, selenides and tellurides of the IIb elements - zinc, cadmium and mercury. Chalcogenides of IIa element beryllium have received little attention so far. Chalcogenides of mercury have negative band gap semi-metal characteristics and some of them play a very important role in applications such as infrared sensor [1]. In this research work, the study has primarily focused on the wide band-gap semiconductors ZnS, ZnSe, ZnTe and their alloys with possible incorporation of magnesium or cadmium. An important feature of these wide band gap II-VI compounds is the direct energy band gap which covers the entire visible spectrum. This feature makes them ideal candidates for device applications requiring efficient absorption or emission of radiation in the short wavelength region. Research in these II-VI compounds has a very long history. For example, ZnS has been the most important material in luminescence research and applications since 1920's [2]. Due to the difficulties in forming pn junctions, the II-VI compounds have made only a very modest technological impact compared to the group IV (Si) and III-V (GaAs) semiconductors. However, ZnSe based materials have received renewed interest recently as promising materials for the fabrication of blue-green light-emitting devices [3,4]. With the advent of new crystal growth technologies, such as molecular beam epitaxy (MBE) and metal-organic vapor phase epitaxy (MOVPE), high quality layers of these wide band gap II-VI materials can now be deposited at relatively low temperature. The background impurity concentration

has been reduced substantially, and incorporated concentrations of active acceptors and donors have been increased to a level of 10^{17} to 10^{19} cm^{-3}. This has resulted in well conducting p and n type wide band-gap semiconductors. The breakthroughs in the area of p-n junction formation in these material demonstrate that several new types of semiconductor devices such as compact UV/blue/green LEDs and lasers will be commercially available in the not too distant future. This field of research has suddenly become explosive.

In this work, computer aided design (CAD) and device simulation techniques have been applied for design and optimization of existing devices, as well as proof-of-concept and performance evaluation of new devices, based on studies of advanced device physics and numerical methods. A device simulation tool which combines physical and phenomenological methods involving different levels of physical approximations has been developed. Both electrical and optical behaviors can be modeled self-consistently in one-dimensional or in two-dimensional fashion depending on the scale of the simulated device areas. For the QW region, where the quantum confinement effect is important and the optical field change can be neglected, a one-dimensional (1-D) model based on solving the coupled Schrödinger and Poison equations is used. In this model, the long-range Coulomb interaction between electrons and holes can be taken into account through modeling the injection induced carrier confinement. For simplification of the numerical method, an effective band offset approach has been developed. The bulk regions, including cladding and barrier, where quantum effects can be neglected and optical field change becomes significant, are analyzed using a modified two-dimensional (2-D) drift-diffusion model including coupled Poisson and Helmholtz (Maxwell) equations. The quantum effects influence on gain and spontaneous recombination is incorporated by phenomenological parameters obtained from the QW model. Based on this tool, the well-known, recently developed, CdZnSe/ZnMgSSe based laser diodes have been simulated and optimized in a systematical way for a large range of compositions.

To over come the still insufficient p-type doping and Ohmic contact problems, a novel laser diode based on ZnMgSeTe has been proposed and designed. For a possible future transistor application, a ZnS/Si heterojunction bipolar transistor (HBT) has been proposed and simulated. The large band gap difference and close lattice match of this material combination may lead to some very interesting features of device performance. The approach developed in this work can be also applied to other wide band gap hetero-structures, such as GaN based devices.

The dissertation is organized as follow. Chapter 2 provides basic aspects of the wide band gap II-VI semiconductor material, heterojunction and device properties. Important material issue such as doping problem, strain effect and band alignment are discussed, and important material parameters such as band gap energy and lattice constant are derived or evaluated and summarized. Device applications of laser diodes and HBTs are also briefly reviewed. Next, two electrical models used for device simulation in this work are introduced in chapter 3. The first one is based on the conventional drift-diffusion formula for bulk material property simulation. The second one is based on the envelope function Schroedinger equation for quantum well modeling. The injection induced carrier confinement effect has been evaluated and an effective band offset approach is derived based on the more rigorous quantum effect model. The widely investigated CdZnSe/ ZnMgSSe based QW laser diode is used as an example to demonstrate the model. In chapter 4, a combined optical wave-guide model and local optical gain model are introduced. Then a full-simulation and optimization of the above mentioned laser diode is performed. Starting from 1-D transverse simulation, the gain and spontaneous emission spectra, as well as the peak gain vs. and injected carrier density relation of such a device is obtained, from which semi-phenomenological gain and radiative recombination (spontaneous-emission) coefficients are established. These phenomenological gain and spontaneous-emission coefficients are then combined with a comprehensive double heterostructure (DH) laser simulator (SILVACO LASER),[6] which is based on solving the

coupled Poisson and Helmholtz equations, to perform a full 2-D simulation including lateral effects. Chapter 5 describes the two novel heterostructure devices proposed in this thesis. A laser diode based on the ZnMgTeSe material system and a HBT based on ZnS/Si are introduced and analyzed. Finally, conclusions of this work and suggestions for future work are presented in chapter 7.

Chapter 2 II-VI MATERIAL, HETEROSTRUCTURE AND DEVICE

2.1 Introduction

The accurate design and simulation of semiconductor devices rely on correctly using both physical principles and material parameters. The device physical models will be the central topic of chapter 3 and 4. This chapter presents the fundamental material and heterojuntion properties of II-VI wide band gap materials, along with a brief review of material processing technology as well as an introduction of fundamental device structures and applications.

2.2 Growth and doping of wide band gap II-VI semiconductors

As mentioned in the introduction, MBE and MOVPE are the most widely used methods for modern II-VI compound growth. In hetero-epitaxial growth, lattice match is a very important factor in determining what can be grown with high crystal quality in a reliable way. Perfect lattice match means that high-quality epitaxial layers can be prepared with any thickness. However, if the lattices do not match, then strain energy builds up in an epitaxial structure until, at a particular thickness (the so-called critical thickness[21]) misfit dislocations are introduced to release the strain. An example of a good lattice match is the combination of GaAs and AlAs, exhibiting only 0.11% mismatch. The lattice mismatch between ZnSe and GaAs is also quite small, about 0.26%. In fact, since GaAs substrates are easily available in sufficiently good quality, ZnSe layers are usually grown on (100) GaAs substrates. Ideally, ZnSe is the natural-choice substrate for the growth of

ZnSe films in a homo-epitaxial growth technique. However, it is still difficult to find commercially available ZnSe substrates of good quality. Other wide band gap II-VI compounds such as ZnS and ZnTe have also been grown on a GaAs substrate, despite the large (about 5%-8%) lattice mismatch [7,8]. For high-quality ZnS thin-film growth, GaP or Si will be a substrate with a better lattice match (only about 0.7% mismatch); InAs or GaSb will be a better lattice-matched substrate for ZnTe growth (less than 0.1% mismatch). Desired lattice matching in combination with the preferred band gap can be realized by growing ternary or quaternary alloys. For example, the ternary $ZnS_{0.06}Se_{0.94}$ is exactly lattice matched with GaAs.

High quality ZnSe-based compounds with controlled low background impurity concentration have been obtained by studying the growth kinetics and by employing purer source materials.[5] However, difficulties have been experienced in controlling the electrical properties of the bulk materials to attain both p-type and n-type doping. It is well known that all II-VI compounds with energy gaps in excess of 2 eV are, unfortunately, subject to strong compensation effects because of the partial ionic character in the bond type. Some of them (ZnSe, CdSe etc.) are found to be primarily n-type while others (ZnTe) are only p-type. The ionic character in the bonding can be described by the difference of electronegativity between the two constituent elements, as shown in Figure 2-1. Doping of ZnSe has been extensively studied, and a breakthrough in p-type doping has been demonstrated by applying the nitrogen radical doping technique [9], which lead Haase et al.[10] to successfully fabricate the first blue-green laser diode operating at 77 K. Even though, due to the deep activation energy (~ 100 meV) of the nitrogen acceptor, the acceptor doping is still remains quite moderate and further improvements of doping techniques may still expected.

The difficulty of p-type doping in ZnSe has been attributed to the solubility limitation of the dopants [11]. In case of the most successful p-type dopant in ZnSe which appears to be atomic nitrogen produced by a plasma source, a typical N concentration is limited

about 10^{19} cm^{-3}. [12] It is interesting to compare the doping of ZnSe with the that of another wide band-gap material, GaN which usually crystallizes in a hexagonal (Wrutzite) structure. In the case of Mg doped GaN, the solubility of Mg in GaN seems fairly high. An impurity doping level as high as 1.5 - 5 x 10^{20} cm^{-3} has been reported.[13] A simple explanation can be obtained by noticing that the metallic form of Mg also has a hexagonal close-packed structure and the lattice constants are a = 3.21 Å, c = 5.21 Å,[65] very close to those of the GaN (a = 3.19 Å, c = 5.18 Å). Thus, the two materials can be relatively easily mixed and the solubility of Mg can be very high in GaN. In the ZnSe case, unfortunately no such dopant has been found. This implicates that, if the acceptor doping level in ZnSe, unlike in GaN, remain limited, an impurity band which might be the main conduction mechanism for deep acceptor levels in these materials can not be formed. According to the impurity band theory,[14] the impurity conduction is originated from the fact that there is a small but finite overlap of the wave function of an electron (or hole) on one donor (or acceptor) with its neighboring donors (or acceptors), a conduction process is possible in which the electron (or hole) moves between impurity centres by tunnelling without activation into the conduction band. As the concentration N_{imp} of impurities increases, the activation energy for conduction in the temperature range for impurity conduction decreases and at a critical value N_c vanishes. N_c can be roughly estimated by

$$N_c = (2.2\alpha_H)^{-3} \exp[-(\varepsilon_o - 1)] \qquad (2.1)$$

where α_H is the hydrogenic Bohr radius and ε_o is the static dielectric constant of the pure host material. For GaN, N_c is estimated about 1.2 x 10^{20} cm^{-3}, which is somewhat below the current Mg doping concentration levels. For ZnSe N_c is about 8 x 10^{20} cm^{-3}, which is almost two order of magnitude higher than the value that current nitrogen radical doping technique have reached.

2.3 Material properties of wide band gap II-VI semiconductors

Compared with group IV and III-V materials, reliable data for II-VI materials are not readily available in the literature. Due to the multi-modification of crystal structure that often occurs in II-VI materials, even the available data need to be used with caution. For the device modeling in this work, a data collection of relevant wide band gap semiconductors, i.e. IIa (Be, Mg, Ca)-VI, IIb-VI and the III-V Nitrides has been obtained by combining carefully evaluated literature data and data derived by simple theoretical calculations based on the solid-state bond picture. (See Appendix C)

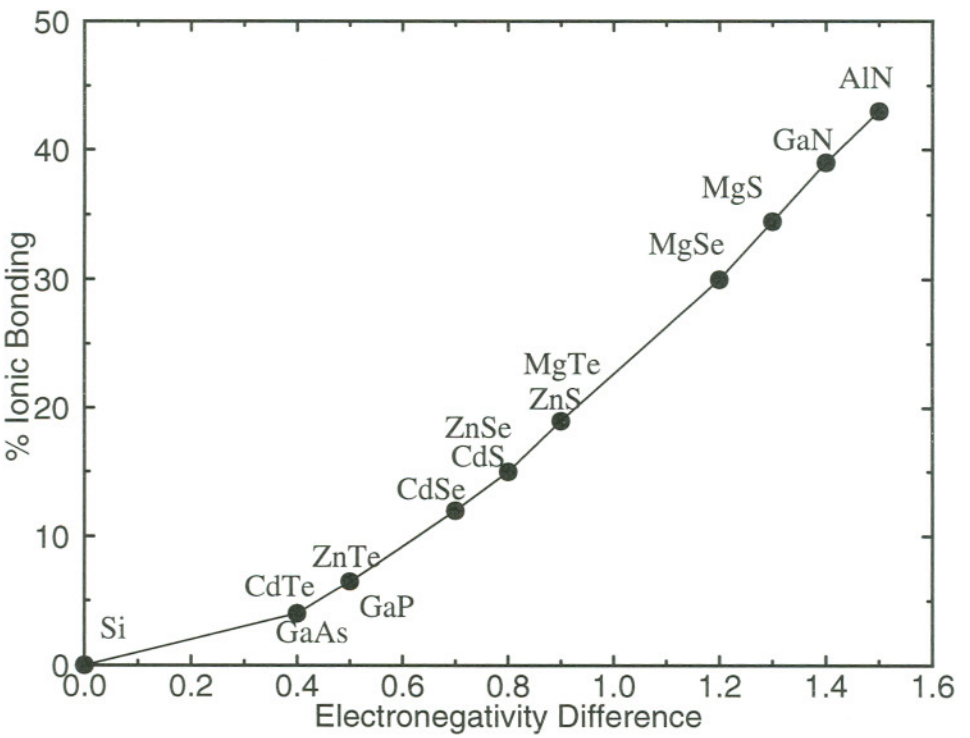

Figure 2-1: Percentage of ionic bonding vs. electronegativity difference of two elements of common II-VI and some III-V binary semiconductors. (Data from Ref. [15].)

2.3.1 Band and lattice parameters

Band gap and lattice constant are the most important parameters in device design and modeling. A general feature of II-VI semiconductors is their direct energy gap and they often crystallize in two possible modifications, the cubic zinc blende (ZB) structure and hexagonal wurtzite (WZ) structure. Usually, for both optical and electronic device applications, the cubic crystal structure is preferred, because it has a higher mobility and can be cleaved more easily. Most of the II-VI compounds have a strong covalent bond. However, the ionic character increases as the atomic weight decreases[15]. Figure 2-1 shows the percentage of ionicity in the bond vs. the difference of electronegativity of the two elements forming the compound which is directly related to their atomic weight.

Table 2-1: Tetrahedral Covalent Radii (in Å)

Element	Pauling[16]	Phillip[17]
S	1.04	1.127
Se	1.14	1.225
Te	1.32	1.405
Zn	1.31	1.225
Cd	1.48	1.405
Hg	1.48	1.403
Mg	1.40	1.301

A simple method can be applied to estimate the lattice constant, based on the covalent bonding. The lattice constant a for the zinc-blend structure follows from the length of the tetrahedral bond d as

$$a = \frac{4}{\sqrt{3}}d \tag{2.2}$$

and the bond length d is given as the sum of the two covalent radii r of the participating

group-II and group-VI elements:

$$d = r_{II} + r_{VI} \tag{2.3}$$

Values for covalent radii have been given by Pauling[16] and were later modified by Phillips[17]. For the elements of interest, both values are listed in table2-1.

Reasonable good results have been obtained by this simple method. Table 2-2 shows some examples.

Table 2-2: Lattice constant of major II-VI compounds (in Å)

Compound	Measured data	Calc. from Pauling's data	Calc. from Phillips' data
ZnS	5.410[b]	5.427	5.432
ZnSe	5.668[b]	5.658	5.658
ZnTe	6.10[b]	6.074	6.074
CdS	5.825[b]	5.820	5.847
CdSe	6.052[b]	6.05	6.07
CdTe	6.482[b]	6.466	6.48
MgS	5.62[a]	5.635	5.607
MgSe	5.89[a]	5.866	5.834
MgTe		6.28	6.249

a: data taken from Ref. 63; b: data taken from Ref. 34.

A calculation of band gap is more difficult and published experimental data were used as long as they were available. A band structure calculation approach based on the semi-empirical extended Hükel theory[18] has been evaluated for the other cases. Band gap versus lattice constant diagrams were generated for the II (Mg, Zn, Cd)-VI (S, Se, Te)

material systems at room temperature, as shown in Fig.2-2. Because of the importance of ternary and quaternary alloys in II-VI heterostructures, the accurate band gap versus lattice constant of the ternary and quaternary alloys for any arbitrary composition have also been determined according to the following approach.

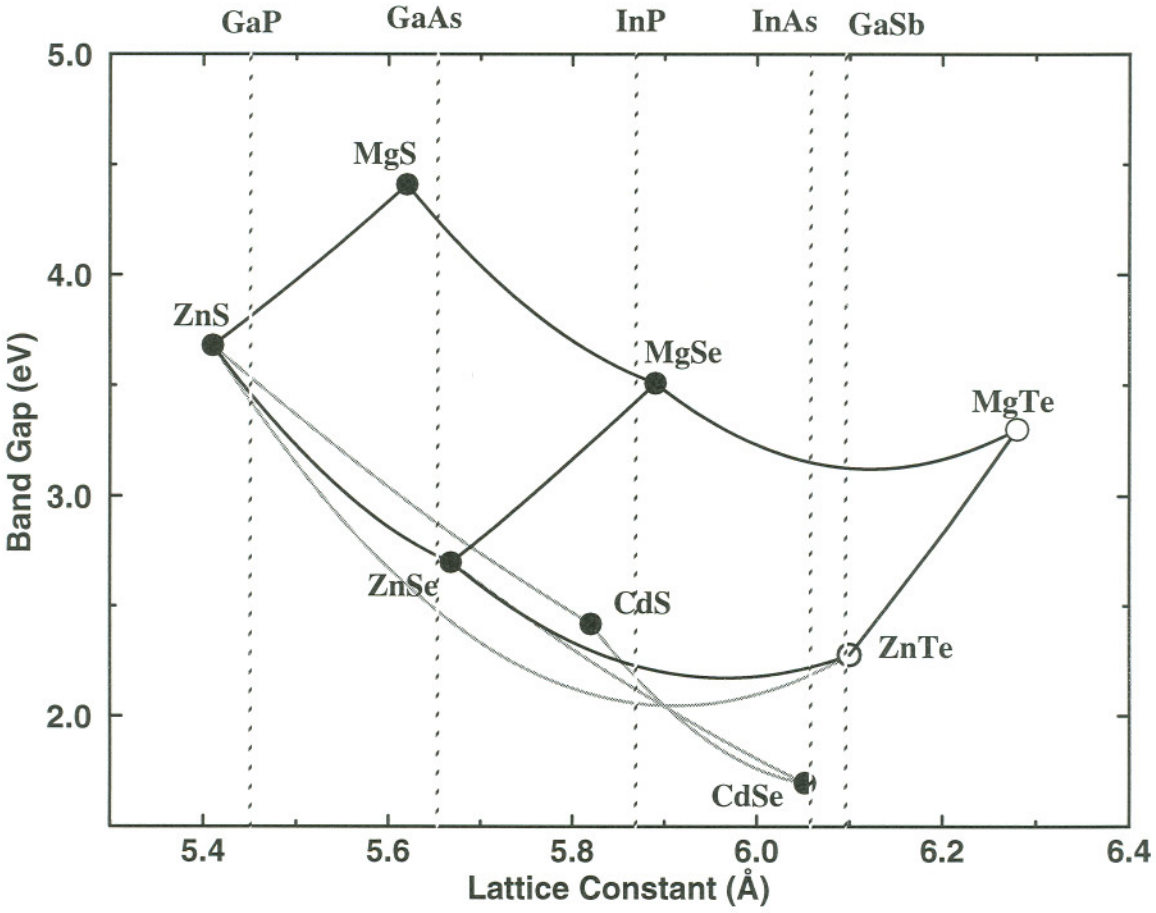

Figure 2-2: Band gap vs. lattice constant of wide-band-gap II-VI material at 300 K; closed circles stand for binary with n-type residual conductivity; opened circles stand for binary with n-type residual conductivity; shaded lines stand for the III-V substrate.

For ternary alloys, $A_xB_{1-x}C$, band gap and lattice constant are obtained from the respective binary values. The lattice constant follows from Vegard's law

$$a(x) = xa_{AC} + (1-x)a_{BC}, \tag{2.4}$$

Due to the relative large ionicity, band gap bowing is very significant in wide band gap II-VI alloys. The band gap E_g can be described by the equation[20]

$$E_g(x) = [xE_g^{AC} + (1-x)E_g^{BC}] - bx(1-x), \tag{2.5}$$

where b, the so-called bowing parameter, can be calculated from

$$b = (Ze/8\pi\varepsilon_0)\,(1/r_A - 1/r_B)^2\,(r_A + r_B)\,\exp(-s\,d_M/2). \tag{2.6}$$

Here, Z is the valence number, Z = 2 or 6 for II-VI compounds (Z=2, when A, B refer to group II; and Z=6, when A, B refer to group VI elements); r_A and r_B are Pauling's covalent radii of the two substitutional elements (e.g. A and B above) which can be found in table 2-1; e is the electron charge; ε_0 is the permittivity of free space; s = 0.25 (1/Å) is a screening constant; and d_M is the tetrahedal bond length at mid-composition ($d_M = \frac{\sqrt{3}}{4}a_M$). The data for the quaternaries are obtained by interpolation from the corresponding ternaries.

Table 2-3: Bowing parameters of II-VI compounds

Alloy	Experimental[19] b	Calculated b
ZnSSe	0.43	0.49
ZnSeTe	1.23	1.11
ZnSTe	3.0	3.11
ZnCdSe	0.30	0.22

Based on the above considerations, a computer program to calculate the bowing parameter as well as the band gap and lattice constant of ternary or quaternary alloys at a

given composition has been generated, as a part of the simulation tool. For some alloy systems for which experimental bowing parameters are available, the results are compared with calculated data as shown in Table 2-3.

2.3.2 Other parameters used in the simulation

For the II-VI compounds that we are interested in, such as ZnS, ZnSe and ZnTe, electronic properties of the cubic modification have been studied both theoretically and experimentally[63]; however for CdSe most data are available for the WZ modification only[63]. A few reports on alloys containing Mg have been published recently[34]. A collection of data for most II-VI compound can be found in Appendix C. Here the major material parameters of the CdZnSe/ZnSSe/MgZnSSe system, widely investigated for blue/glue diode lasers, which will be used in later chapters of this thesis are listed in table 2-4

Most the binary data for ZnSe and CdSe and ZnS can be found in Ref. 63. Data of transport and optical properties of the ZnSe/(Mg)ZnSSe system are taken from Refs. 63, 64 and 4.

2.4 Heterojunction properties of wide band gap II-VI materials

A heterostructure is defined as a semiconductor structure in which the chemical composition changes with position. Heterostructures are able to improve the performance of semiconductor devices because they permit the device designer to modify locally the energy-band structure and so control the motion of the charge carriers. In the heterojunction bipolar transistor, as will be discussed in chapter 5-2, a heterojunction is used to encourage the transport of electrons while suppressing the transport of holes. In the quantum-well lasers, both electrons and holes are confined by the heterojunction to regions comparable to their quantum-mechanical wavelength, which leads to finer control over the optical interactions.

Table 2-4: Parameters of ZB CdZnSe/ZnSSe/MgZnSSe material system @RT

	$Cd_{0.2}Zn_{0.8}Se$; (Strained QW)	ZnSe	$ZnS_{0.06}Se_{0.94}$	$Mg_{0.1}Zn_{0.9}S_{0.14}Se_{0.86}$
a (Å)	5.744, (5.66)	5.668	5.652	5.652
E_g (eV)	2.46, (2.51 HH)	2.70	2.73	2.85
m_e (m_0)	0.140	0.149	0.149	0.18
m_{hh} (m_0)	(0.18^a , 1.16^b)	0.57	0.6	0.61
m_{lh} (m_0)	(0.32^a , 0.14^b)		0.23	
γ_1	4.3	4.3	4.3	
γ_2	1.14	1.14	1.14	
γ_3	1.84	1.84	1.84	
C_{11} (10^{10} N/m^2)	8.42	9.0	9.04	
C_{22} (10^{10} N/m^2)	5.26	5.34	5.34	
C_{44} (10^{10} N/m^2)	3.88	3.96	3.69	
a_v (eV)	-5.04	-5.82	-5.82	
b_v (eV)	-1.12	-1.2	-1.2	
μ_e (cm^2/Vs)	600	500	479	250
μ_{hh} (cm^2/Vs)	60	30	66	10
ε_0	10.6	7.6	8.5	
ε_∞	8.2	5.4	5.3	
n (@500nm)	2.88	2.8	2.74	2.62
E_A (meV)		100 (N)	100 (N)	110 (N)
E_D (meV)		20 (Cl)	20 (Cl)	20 (Cl)

a: along vertical z direction. b: in xy plane (see Fig. 2-5).

There are several basic considerations for making heterostructure devices. First, the mismatch between the lattice constants of the two constituent materials; second, the type of doping that can be usefully attained in a given semiconductor; third, the offset in the band edges in going from one material to the other. From Fig.2-2 one can see that the lattice parameters fall into a few clusters within each of which the match is rather good but between different clusters which the match is poor. Doping characteristics are also indicated in Fig.2-2. A filled circle represents material which can be easily n-type doped while a unfilled circle represent materials which can be easily p-type doped. The doping of II-VI compounds has been already discussed in chapter 2.2, in the following the discussion is focused on heterojunction related properties, including strain effect and band alignment.

2.4.1 Strain effect

From Fig.2-2, one can see that it is very hard to get a large band gap difference between QW and barrier in standard lattice matched IIb-VI heterostructures. So, incorporation of strained, rather than unstrained QWs in II-VI alloy systems is inevitable. In addition, both biaxial compressive and tensile strain in the QW is expected to reduce lasing threshold current, which has already been demonstrated in III-V devices.[23]

When growing a thin QW layer of material (along z) with lattice constant a_1 on top of the substrate material with lattice constant a_2, below a certain critical thickness[22], rather than forming misfit dislocations, biaxial (x, y) elastic strain accommodates the strain energy associated with the mismatch. The strain tensor is given by[23]

$$\varepsilon_{xx} = \varepsilon_{yy} = 1 - \frac{a_1}{a_2} \tag{2.7}$$

$$\varepsilon_{zz} = -2\frac{C_{12}}{C_{11}}\varepsilon_{xx} \text{ ; and } \varepsilon_{xy} = \varepsilon_{yz} = \varepsilon_{zx} = 0. \tag{2.8}$$

C_{11}, C_{12} are the elastic moduli of the bulk material.

The distortions in the crystal lattice leads to alterations in the band structure of the strained layer. The valence band becomes anisotropic with different effective masses parallel and perpendicular to the strain direction and also the light-hole and heavy-hole band at the G point start to split. The effective masses in specific directions at the Brillouin zone center are certain functions of the Luttinger parameters γ_1, γ_2 and γ_3,[24] (the values are listed in table 2-4 for CdZnSe.) which are material constants and give a complete description of the parabolic band structure near the edge. One can define the light-to-heavy-hole (average) splitting parameter as[23]

$$\gamma = (2\gamma_2^2 + 2\gamma_3^2)^{1/2} \tag{2.9}$$

The effective masses for the heavy- and light-hole bands in the x-y plane are then given by (in units of m_o)

$$m_h^{\parallel} = (\gamma_1 - \gamma)^{-1} \tag{2.10}$$

$$m_l^{\parallel} = (\gamma_1 + \gamma)^{-1} \tag{2.11}$$

The effective masses for the heavy- and light-hole bands along the z-direction are given by

$$m_h^{\perp} = (\gamma_1 + \gamma/2)^{-1} \tag{2.12}$$

$$m_l^{\perp} = (\gamma_1 - \gamma/2)^{-1} \tag{2.13}$$

The shift in band-gap due to hydrostatic strain is:

$$E_{shift} = -2(a_v - \alpha_c)\varepsilon_{xx}\frac{C_{11} - C_{12}}{C_{11}} \tag{2.14}$$

The valence band splitting due to the tetragonal shear deformation is:

$$E_{split} = -b_v\varepsilon_{xx}\frac{C_{11} + 2C_{12}}{C_{11}} \tag{2.15}$$

where a_v and b_v are the hydrostatic and shear deformation potentials, respectively.

In the biaxially strained QW layer the total band-gap energy changes are thus given by:

$$E_{g,h} = E_g + E_{shift} - E_{split}, \tag{2.16}$$

$$E_{g,l} = E_g + E_{shift} + E_{split} \tag{2.17}$$

For compounds such as CdSe and GaN, for which only the data of WZ elastic moduli (C_{ij}) (six independent parameters) are available at the current time, the cubic ZB data (only three independent parameters) can be derived from these WZ data, by following the method given by R. M. Martin[25].

According to Martin, although the transformation from WZ to ZB is not unique, the ZB data can be estimated by a least-square fit to the six WZ constants weighted equally. These so-called effective ZB cubic elastic moduli are given by the following equation:

$$C_i^{eff} = \sum_{k=1}^{6} S_{ik} C_k^{WZ} \tag{2.18}$$

where, the matrix S is found numerically to be

$$S = \begin{bmatrix} 0.603 & -0.515 & -0.103 & 1.015 & 1.470 & 0.353 \\ 0.015 & 0.426 & 0.485 & 0.074 & -0.647 & -0.235 \\ 0.118 & 0.412 & -0.118 & -0.412 & -0.176 & 0.118 \end{bmatrix}.$$

For example, the WZ data for CdSe are (in unit of 10^{10} N/m^2) C_{11}=7.41 C_{33}=8.36 C_{12}=4.52 C_{13}=3.93 C_{44}=1.317 C_{66}=1.445. The derived ZB data become C_{11}=6.13 C_{12}=4.96 C_{44}=2.10. In comparison for GaN, the WZ data are C_{11}=29.6 C_{33}=26.7 C_{12}=13.0 C_{13}=15.8 C_{44}=2.41 C_{66}=3.0 and the derived ZB data become C_{11}=23.40 C_{12}=17.02 C_{44}=6.38.

This procedure has been used for obtaining the C_{ij} data listed in table 2-4. Using a linear interpolation between CdSe and ZnSe data, a compressively strained $Zn_{0.8}Cd_{0.2}Se$/

ZnSe quantum-well band structure has been calculated based on the equations (2.5)-(2.14); E_{shift} is estimated at about 65 meV and E_{split} at about 80 meV, as shown in Figure 2-4. The band-gap under biaxial compressive strain, referring to the heavy-hole to electron band-edge, is 2.51 eV.

2.4.2 Band alignment

The band alignment at a semiconductor heterojunction (so called heterojunction band offset) is a very important property for the characterization and design of novel heterostructure devices. The steps in energy between the conduction band edges and the valence band edges are called the conduction band offset ΔE_c and the valence band offset ΔE_v, respectively. Several different experimental methods are used to obtain band offsets. They are based on optical determinations, electrical measurements in devices and photo emission experiments[26]. From the theoretical point of view, there is a large variety of approaches. They go from the simple 'electron affinity rule', to fully self-consistent calculations of the interface electronic structure. A comprehensive review of the semiconductor band offsets has been given by Yu, McCaldin and McGill[27]. Among the most notable theories for the II-VI hetero-junctions are the so-called common anion rule[27], based on the concept of meaningful relative positions of the valence band edges as gauged by the tight binding atomic term values due to Harrison,[28] and the concept of a neutral charge position, originated by Tersoff[29] and extended by Harrison and Tersoff [30]. In spite of considerable effort, a thorough and precise understanding of the physics of band offsets has yet to be attained. To be of use in the quantitative evaluation and design of a semiconductor hetero-structure device, a band offset must typically be known to an accuracy of approximately ±0.01 eV or better; however, predicted band offset values for many hetero-junctions of current interest extend over a range of 1 eV or more, rendering them of limited use in determining the viability of various device structures in these material systems.

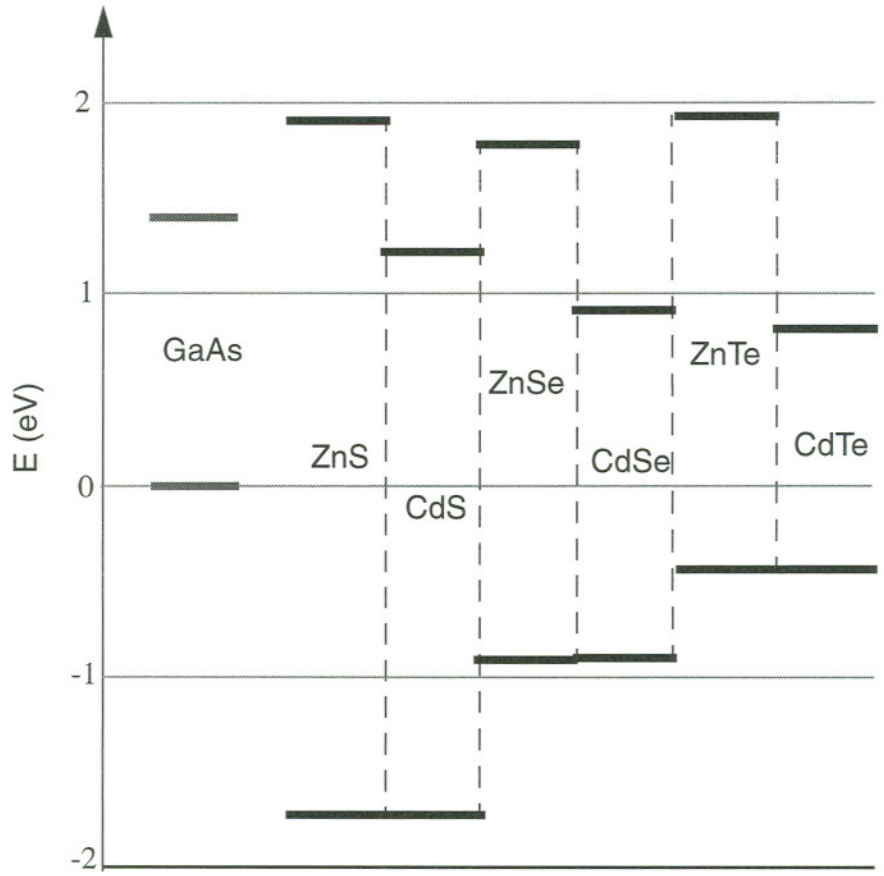

Figure 2-3: General band alignment of wide-band-gap II-VI materials based on the common anion rule.[27]

A rough picture of II-VI semiconductor band offsets can be obtained by using the common anion rule, which have been presented in Figure 2-3. Due to the strain effect, however, the band alignment can be quite different in a real heterostructure. The strain

effect on band alignment can be calculated from the hydrostatic deformation potential for the valence band a_v and conduction band a_c, according to van de Walle[31], as follow:

$$\delta E_v = a_v(\varepsilon_{xx} + \varepsilon_{yy} + \varepsilon_{zz}) \; ; \; \delta E_c = a_c(\varepsilon_{xx} + \varepsilon_{yy} + \varepsilon_{zz}) \tag{2.19}$$

where $\delta E_c + \delta E_v = E_{shift}$, see equation (2.11).

Figure 2-4 shows the band diagram of a $Cd_{0.2}Zn_{0.8}Se$/ZnSe QW structure under the compressive strain in the QW. The hydrostatic deformation potentials are found to be $a_v = 1.65$ and $a_c = -4.17$ in this case[31], which means both conduction and valence band shift upwards. Because of this energy shift due to strain, the valence band offset of the heavy hole has been substantially increased compared to the unstrained case.

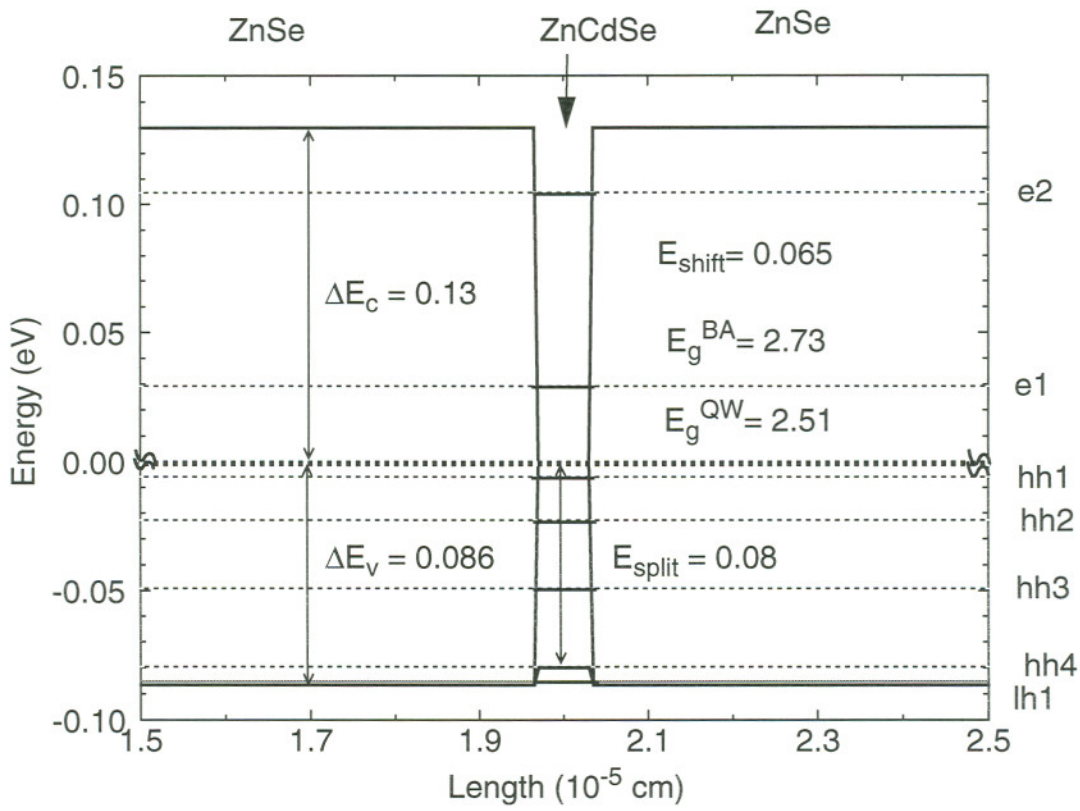

Figure 2-4: Band diagram of compressively strained $Zn_{0.8}Cd_{0.2}Se$/ZnSe QW structure with conduction band offset ratio $Q_c = 0.6$.

2.5 Wide band gap II-VI semiconductor devices

Presently, the most exciting device application possibilities for II-VI materials are photonic devices such as light emitting diodes (LED) and laser diodes (LD) at wavelengths throughout the visible spectrum. Wide-band semiconductors are also attractive candidates for high temperature transistor application. In this work, particular interest has been placed on design and modeling of blue-green laser diodes. The potential of wide band-gap II-VI semiconductor for transistor application has also been exploited.

2.5.1 Laser diode and light emitting device

Simulated emission of photons can be produced in semiconductors by the recombination of carriers (electrons and holes) injected, e.g. across a forward biased p-n junction. In order to achieve high carrier densities at low currents, it is necessary to confine the recombining carriers to as small a volume as possible. Also, the optical field or photons need to be guided to the recombination region. In the semiconductor laser diode, both carrier(electrical) and photon (optical) confinement are realized by sandwiching different materials with sufficient band gap and refractive index difference. As shown in Fig.2-5., a so called separate-confinement heterostructure (SCH) is often used to achieve low threshold current density operation. The carrier confinement is realized by the band gap step between the center layer and the barrier layer(BA). The size of the lowest band-gap center layer is usually in the range of 50-100 Å, where the quantization of the electron levels becomes significant, so this layer is often called quantum-well (QW). The barrier layers also act as the guiding layer of the optical field. The cladding layers with the largest band gap, and hence, a smallest refractive index are used to confine the optical field. The cladding layer need to be electrically active so the electron and hole can be easily transported. An ohmic contact has to be formed to each of the cladding layers.

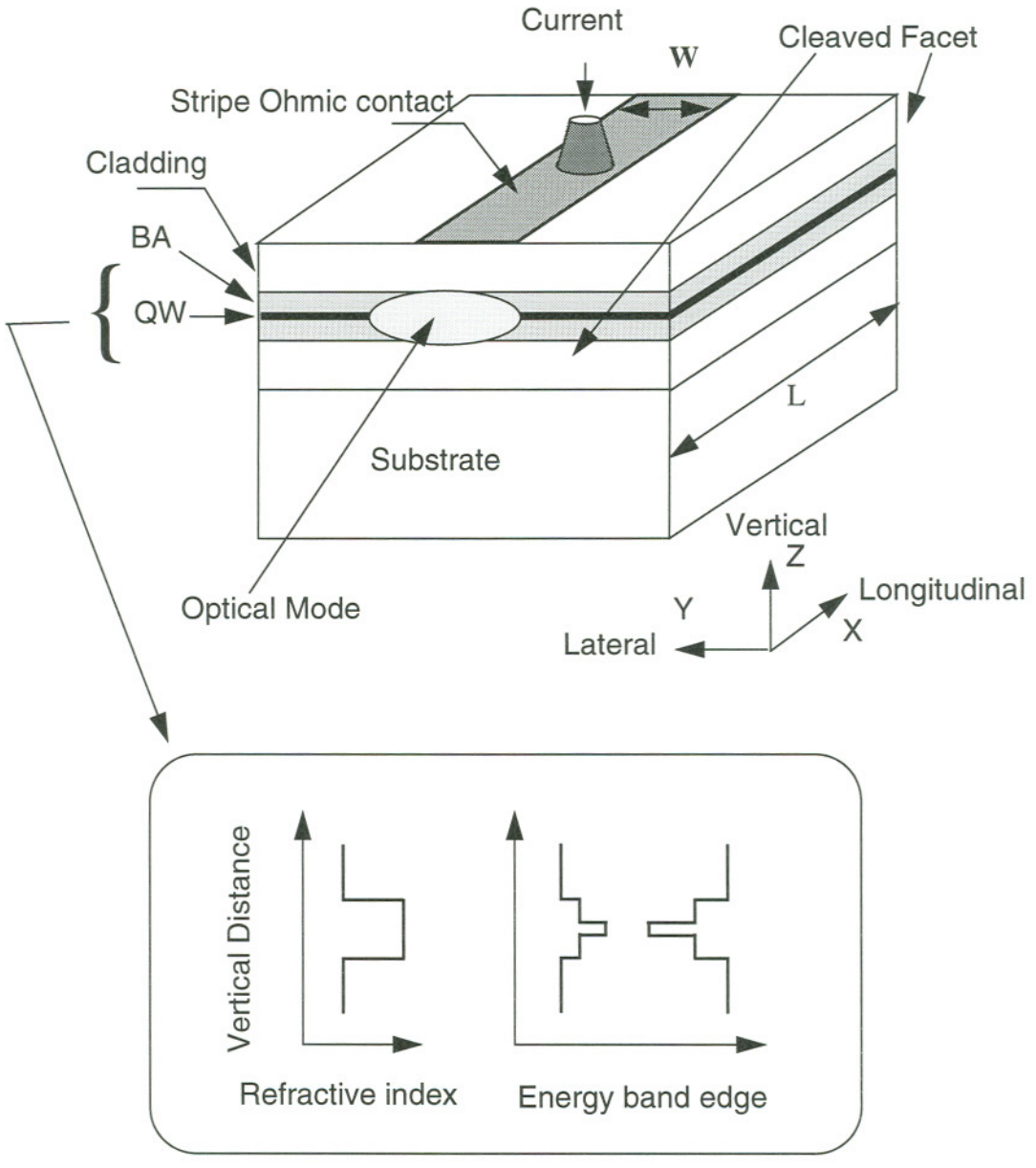

Figure 2-5: Gain guided SCH QW laser diode device structure and transverse electrical and optical confinement (flat band condition).

Figure 2-5 shows an Ohmic top contact with stripe-geometry configuration of width W, which provides a means of localizing the gain in the lateral direction. Such a configuration is called gain-guided device. In a conventional Fabry-Perot laser, the optical resonator is formed by cleaving the facet. When the carrier density within the QW reaches a certain value at which the gain of the photon mode is equals the total loss, the light generated by amplification will be sufficient to yield laser emission.

Since the first successful room-temperature operation of a laser diode was demonstrated using a GaAs/AlGaAs double heterostructure (DH),[32] many direct band gap semiconductor materials such as AlGaAs, InGaAs, InGaAsP, GaInP and InAsP and many others were used to obtain semiconductor lasers at different wavelengths. Since the photon energy is approximately equal to the band-gap energy, the lasing wavelength λ (in μm) is given by

$$\lambda \cong \frac{1.24}{E_g} \ (\mu\text{m}) \tag{2.20}$$

where E_g is expressed in electron volts. The human eye visible response spectrum is roughly in the wavelength region of 700 nm to 400 nm, with the corresponding band gap is from 2.5 eV to 3.0 eV. Thus, wide band II-VI materials such ZnSe, ZnTe and CdS are good candidates for visible laser application.

In early works, solid solutions and later heterostructures of the CdTe/ZnTe and ZnTe/ZnSe systems have been investigated for light emitting device application.[2] CdTe is the only II-VI binary that can be easily made both n-type and p-type. The band gap of CdTe is only 1.4 eV, however. It was thought that by forming solid solution of MgTe and CdTe, visible electroluminescent p-n junctions can be made for an adaptable composition range [33].

The most extensively studied II-VI materials are ZnSe and its related alloys, due to the effort of developing a blue/green light emitting device. From Fig.2-2, these materials are among the cluster whose lattice constants are very close to that of GaAs. It appears that

several different heterostructures with ZnSe can be formed in this group using, e.g., ZnSTe, ZnSeTe, ZnCdSe and ZnCdS. From the general band alignment picture based on the common anion rule (Figure 2-3), we know that the alloys which contain S will have a lower valence band than that of ZnSe, thus, only ZnCdSe and ZnSeTe can be used for the QW layer in a ZnSe barrier. In the ZnCdSe/ZnSe heterostructure, only a small valence band offset is expected, while in the ZnSeTe/ZnSe heterostructure, a small conduction band offset is expected. However, due to the strain effect and the injection induced carrier confinement effect, as will be discussed in detail in the next chapter, the hole confinement in the ZnCdSe/ZnSe heterostructure is much better than it appears. The first blue-green diode laser by Haase et al. was fabricated as a $Cd_{0.2}Zn_{0.8}Se/ZnSe/ZnS_{0.07}Se_{0.93}$ separate confinement quantum well structure.[10] In this structure, the light emitting region is a compressively strained $Cd_{0.2}Zn_{0.8}Se$ QW of about 100 Å thickness sandwiched between two ZnSe barrier (light guiding) layers. The cladding layers are $ZnS_{0.07}Se_{0.93}$ which is lattice matched to the GaAs substrate at the growth temperature of 300 °C. The n-type layers were doped with Cl and the p-type layers with N from an RF plasma source using N_2 gas, yielding a net acceptor concentration of about $2x10^{17}$ cm^{-3}. The diode laser is gain guided using a Au-evaporated stripe-geometry electrode. Pulsed operation at 77K was demonstrated. The idea of introducing the IIa element Mg into IIb-VI system has been applied to the ZnSSe system first by Okuyama et al.[34], which substantially increased the band gap range of these GaAs lattice matched alloys. This is clearly evident from Fig.2-2. The ZnCdSe/ZnSSe diode laser[47, 68] using MgZnSSe as cladding can effectively improve the carrier and optical confinement. Also the barrier ZnSSe can now be perfectly lattice matched to the GaAs substrate, thus the misfit dislocations have been greatly reduced.[47] Room temperature cw operation has been achieved in such a device,[68] although the short life time of these device is still a serious problem.[47, 68] The detailed design and optimization of such device will be presented in chapter 4 and 5.

2.5.2 Transistor application

The close lattice matching of ZnSe/GaAs has been utilized in a n-p-n heterojunction bipolar transistor (HBT), which has been demonstrated first by Gaeser et al[35]. In this device, the substrate, collector and base are GaAs and an n-type ZnSe layer is used as wide gap emitter. The use of a wide band gap emitter increased the design flexibility with regard to the base and emitter doping. Further improvement of the above HBT may be achieved by using ZnSSe which is lattice matched with GaAs to replace the ZnSe emitter. The cross doping in these devices may be a problem. In chapter 5, a ZnS/Si heterojunction transistor will be proposed and analyzed.

2.6 Summary

In summary of this chapter, a material and heterojunction parameter data base for II-VI device simulation has been established, especially for the GaAs lattice matched ZnMgSSe system. Strain effects on band parameters have also been evaluated. Based on the bond picture of solid-state compounds, the solubility limitation of the N-acceptor in ZnSe is explained, and simple methods for determining the lattice constants and bowing parameters as well as converting ZB elastic moduli from WZ data have been developed. The device development of II-VI laser diodes and HBTs has been reviewed.

Chapter 3 ELECTRICAL MODEL OF HETEROSTRUCTURE AND QW

3.1 Introduction

With the enormous progress and reduced cost in computer performance, computer simulation is used on a regular basis for reducing the development time and the costly expense of semiconductor device fabrication. In this work, particular interest has been placed on design and modeling of quantum-well (QW) laser diode, which is now the major driving force of the investigation on the wide-band-gap II-VI materials. For sophisticated heterostructure devices such as the separate confinement heterostructure (SCH) QW laser, accurate versatile device models are needed in device design and optimization.

For most of the semiconductor electrical behavior simulations, the macroscopic transport properties can be described by the so-called drift-diffusion (DD) method (the zero-order approximation of the Boltzmann equation), or by modifications of this method through parameterized phenomenological models. The DD relations for the current densities, the current continuity equation, and Poisson's equation, are forming the so-called conventional model as described in Ref. 36. As a first step in the development of an accurate simulation program for a heterojunction device, we adopt a well developed numerical approach based on the modified DD model which takes into account a position dependent band structure,[36,37] as will be described in chapter 3.2.

An improved physical description beyond the above DD methods becomes increasingly desirable as the device dimensions scale down to sub-micron or even smaller. Especially, when quantum-size effects become significant such as in the inversion and accumulation layers at semiconductor-insulator interfaces, heterojunctions, and quantum-wells. In chapter 3.3, a numerical model for quantum confinement effect will be intro-

duced based on the one-electron effective-mass Schrödinger equation. The accurate carrier distribution in the QW structure is obtained and an injection induced carrier confinement effect is evaluated based on self-consistently solving the coupled Schrödinger and Poisson equations.

The models developed in this chapter will be applied to a particular example - a CdZnSe/ZnSSe/MgZnSSe SCH laser diode, throughout the chapter. Important electrical behaviors especially along the transverse direction are discussed in this chapter. A more detailed analysis including lateral effects of such device and complete electrical and optical simulation will be presented in chapter 4.

3.2 Bulk material model of heterostructure

The conventional DD model has been expanded to describe heterostructure device by introducing position-dependent dielectric constant, band gap and density-of-states, as formulated by Lundstrom.[37] As a first step in the development of an accurate simulation program, a similar approach is adopted here.

3.2.1 Conventional model with position dependent band structure

The electrical properties of semiconductor devices can be fully described by the electrostatic potential V, electron density n, and hole density p. Following the approach of Ref. 37, in the steady state, these variables are governed by the following basic equations.

Poisson equation:

$$\nabla\bullet(\varepsilon_o \nabla V) = -q(p - n + N_D^{+} - N_A^{-}), \tag{3.1}$$

where, N_D^{+} and N_A^{-} are the concentrations of ionized donors and acceptors, respectively. ε_0 is the dielectric constant which has spatial dependence in heterostructure devices.

Continuity equations for electrons and holes:

$$\frac{1}{q}\nabla\bullet\boldsymbol{J}_n + G - R = 0 \ ; \tag{3.2}$$

$$\frac{1}{q}\nabla\bullet\boldsymbol{J}_p + R - G = 0 \ , \tag{3.3}$$

where G and R are electron-hole pair generation and recombination rates, respectively. The electron current density $\boldsymbol{J_n}$ and the hole current density $\boldsymbol{J_p}$, combining both drift and diffusion terms, can be written as functions of the gradient of the quasi-Fermi potential, as:

$$\boldsymbol{J}_n = -q\mu_n n\nabla E_F^c \ , \tag{3.4}$$

$$\boldsymbol{J}_p = -q\mu_p p\nabla E_F^v \ . \tag{3.5}$$

Here, μ_n and μ_p denote the carrier mobilities for electron and hole, and $E_F{}^c$ and $E_F{}^v$ are the electron and hole quasi-Fermi levels, respectively.

Generally, the quasi-Fermi levels are related to the electron density n and hole density p, according to:

$$n = \int \rho_c(E_c) f_c(E_c, E_F^c) dE_c \tag{3.6}$$

$$p = \int \rho_v(E_v)[1 - f_v(E_v, E_F^v)] dE_v \tag{3.7}$$

where the integral goes from respective band-edges to infinity; the Fermi-Dirac distribution function should be used for $f_c(E_c, E_F{}^c)$ and $f_v(E_v, E_F{}^v)$ in the degenerate case, as in QW; while the Maxwell-Boltzmann distribution is a good approximation in the nondegenerate case as in the ordinary cladding and barrier layers, which makes the integral easy to solve. Fortunately, a closed analytic form can also be obtained for the Fermi-Dirac distribution in two-dimensional carrier gases, which is just the case of the QW.

3.2.2 Carrier ionization, recombination and generation

In II-VI semiconductors, due to the relatively deep impurity energy level often observed, incomplete ionization of dopants cannot be ignored. Specifically, the following equations have been used[6] for N_D^+ and N_A^-

$$N_D^+ = \frac{N_D}{1 + g_D \exp\left(\frac{E_F^c - E_D}{kT}\right)} \tag{3.8}$$

$$N_A^- = \frac{N_A}{1 + g_A \exp\left(\frac{E_A - E_F^v}{kT}\right)}. \tag{3.9}$$

Where, N_D and N_A are net compensated donor and acceptor concentrations on the n- and p- side, respectively; E_D and E_A are the donor and acceptor energy levels; and g_D and g_A are the degeneracy factors for donor and acceptor; respectively.

The carrier recombination and generation rates R and G in equations (3.2) and (3.3) are determined as follows. Three types of recombination processes which are important in laser diode simulations are considered in this work: Shockley-Read-Hall (SRH) nonradiative recombination[6], spontaneous-emission recombination and stimulated-emission recombination.[6] The radiative recombinations (spontaneous and stimulated emissions) will be discussed in chapter 4. For SRH recombination, the following equation is used:

$$R_{SRH} = \frac{np - n_{ie}^2}{\tau_p\left[n + n_{ie}\exp\left(\frac{E_t - E_i}{kT}\right)\right] + \tau_n\left[p + n_{ie}\exp\left(\frac{E_i - E_t}{kT}\right)\right]} \tag{3.10}$$

where, n_{ie} is the effective intrinsic concentration, E_i is the intrinsic Fermi energy, and E_t is the trap energy level, which is assumed to be the same as the donor or acceptor energy

level. The electron and hole life times, τ_n and τ_p, may be concentration dependent.

The carrier generation due to absorption of simulated photons is included in R_{st} (see equation (4.4)). Carrier generation due to absorption of spontaneous photons and impact ionization is assumed to be small. Thus we use G = 0.

3.2.3 Electrical modeling of the CdZnSe/ZnSSe/MgZnSSe SCH QW laser

The above model has been implemented in a comprehensive 2-D device simulator - SILVACO ATLAS[6], which is used as the simulation platform in this work. We consider a particular device structure - a SCH SQW laser diode, as shown in Figure 2-5. (This type of structure has been used by several groups throughout the world for fabricating blue-green laser diodes.) The vertical and lateral structure parameters chosen for the simulation of such a device are shown in Figure 3-1. This is a SCH with a compressively strained $Cd_{0.2}Zn_{0.8}Se$ SQW of size L_{qw} = 6.5 nm and a $ZnS_{0.06}Se_{0.94}$ barrier and $Mg_{0.1}Zn_{0.9}S_{0.14}Se_{0.86}$ cladding. The size of each barrier and cladding are shown in Figure 3-1. The (Mg)ZnSSe barrier and cladding layers are lattice matched to the GaAs substrate. The QW is assumed to be undoped. The same doping levels are assumed in barrier and cladding layers. The acceptor level is set at $N_A = 5 \times 10^{17}$ cm^{-3}, the donor level at $N_D = 1 \times 10^{18}$ cm^{-3}. The nonradiative minority carrier life times of the electrons and holes, τ_n and τ_p, are assumed to be equal to 1 ns. A constant spontaneous emission coefficient $B = 9.8 \times 10^{-11}$ (cm^3 s^{-1}), as derived in section 4.4.1, is used for radiative recombination calculation. A conduction band offset of $Q_c = 0.6$ is used in this simulation. Other input parameters are taken from table 2-4. Considering the strain effect, a higher heavy hole mobility results in the lateral direction inside the QW due to the reduced lateral effective hole mass. For simplicity, the GaAs substrate and the transition layer for the p-type contact are neglected. Ideal Ohmic contacts both at the 10 μm top stripe and bottom layer are assumed. Figure 3-2 shows the mesh generated for the structure. The grid system is locally refined near the

regions such as heterojunctions where physical quantities abruptly change. The total number of mesh points is 4698. (The software limitation is 4800). For all the simulations room temperature (300 K) is assumed, unless particularly specified. The two-carrier Newton iteration method is used for the drift-diffusion calculations. The bottom contact (cathode) is assumed grounded throughout the simulations. When the top stripe contact (anode) voltage increases positively, the device enters forward bias operation. The I -V characteristic curve is plotted in Figure 3-3. The turn-on voltage is about 2.5 v in this case, which is about the same value as the QW band gap. The energy band diagrams along the vertical-direction for various biases are shown in Figure 3-4. Figure 3-4 shows that, at forward bias above the turn-on voltage, the flat-band assumption is a good approximation in the barrier and QW regions. This assumption will be used later in the QW modeling. The carrier density distributions under different biases along the vertical direction are plotted in Figure 3-5 and compared with the doping levels. At zero bias, i.e. at the thermal equilibrium, due to the incomplete ionization of dopants, free carrier densities are lower than the doping densities every where and the regions near the QW are depleted. As the forward bias increases, due to the smaller band gap in QW, the carrier density in QW increases very rapidly, even though the carrier densities in barrier and cladding remain low. The electrical potential and field distribution along vertical-transverse direction is plotted in Figures 3-6 and 3-7. The accumulation of carriers in QW at high forward bias can be clearly seen in Figure 3-6. Figure 3-7 shows that, a very high field of a magnitude near 1.1×10^5 V/cm may occur under intermediate bias in the barrier layer very close to the QW region. Such a high field may generate impact ionization effect, a phenomena which has not been considered in the current model.

Stimulated emission has been included at high forward bias (> 2.5 v) in the above calculations. In chapter 4, more detail on electron-photon interaction and above-threshold operation will be discussed.

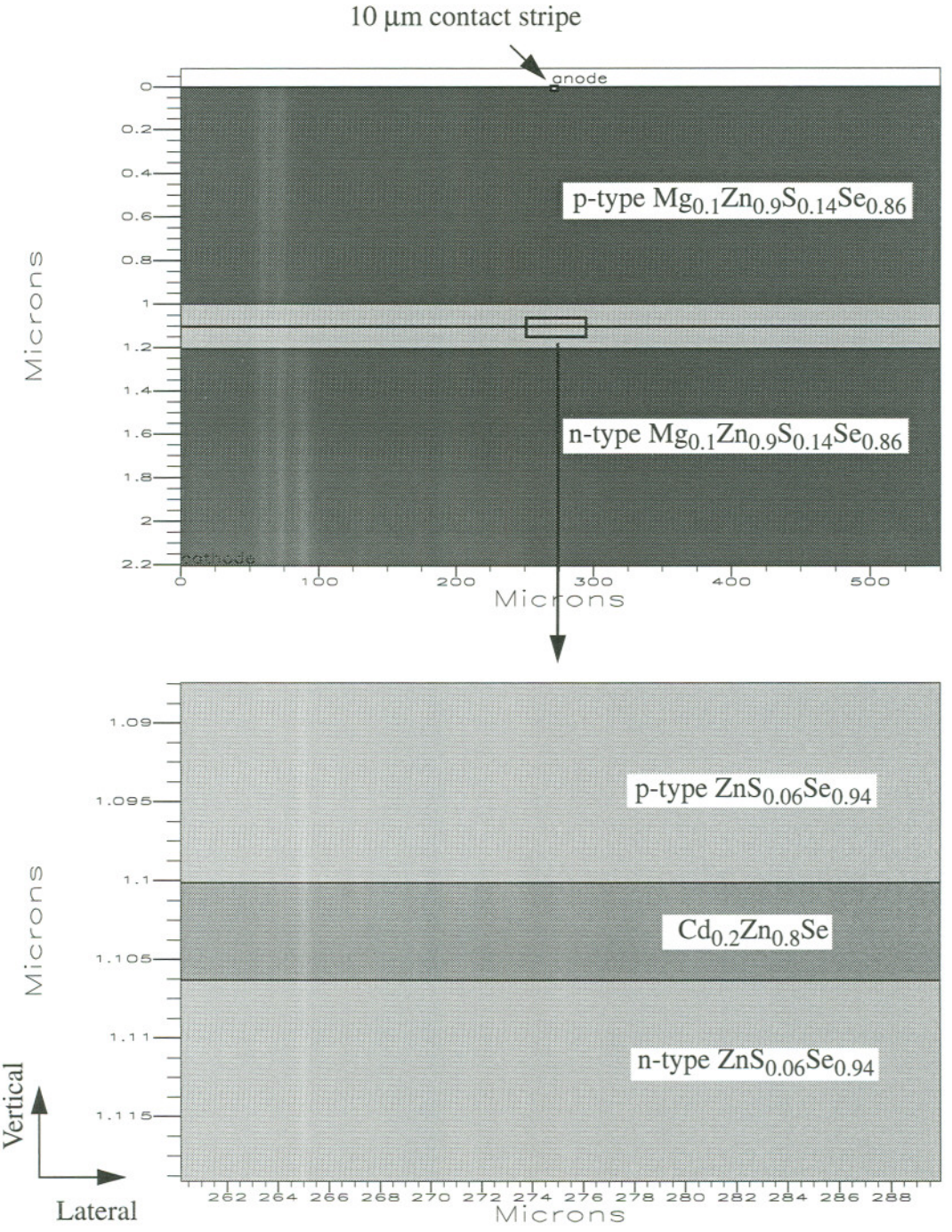

Figure 3-1: $Cd_{0.2}Zn_{0.8}Se/ZnS_{0.06}Se_{0.94}/Mg_{0.1}Zn_{0.9}S_{0.14}Se_{0.86}$ SCH QW laser structure cross section (vertical and lateral).

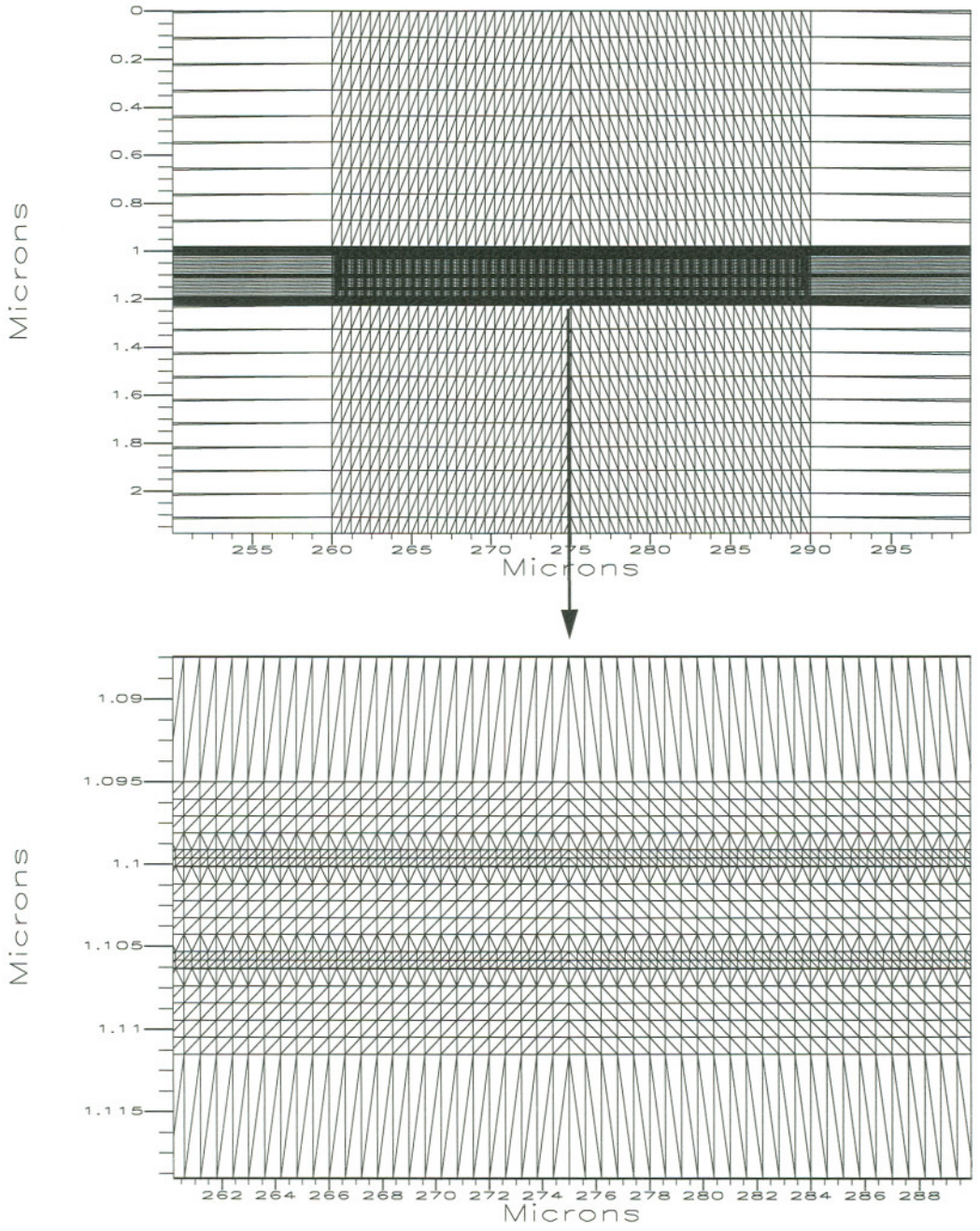

Figure 3-2: Mesh structure for device simulation.

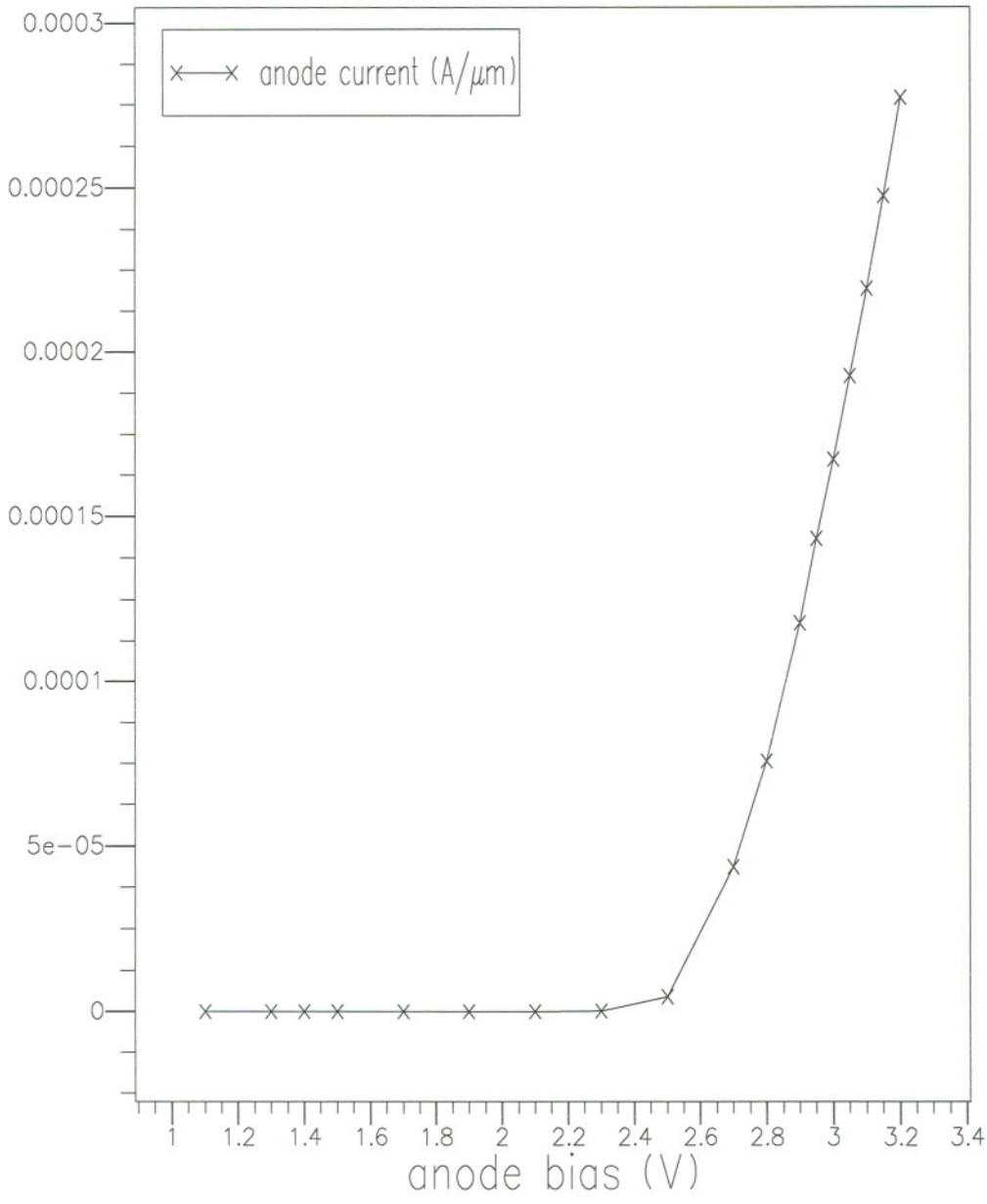

Figure 3-3: Voltage - current relation of CdZnSe/ZnMgSSe SCH QW laser diode. Current normalized to longitudinal dimension (L = 1 mm).

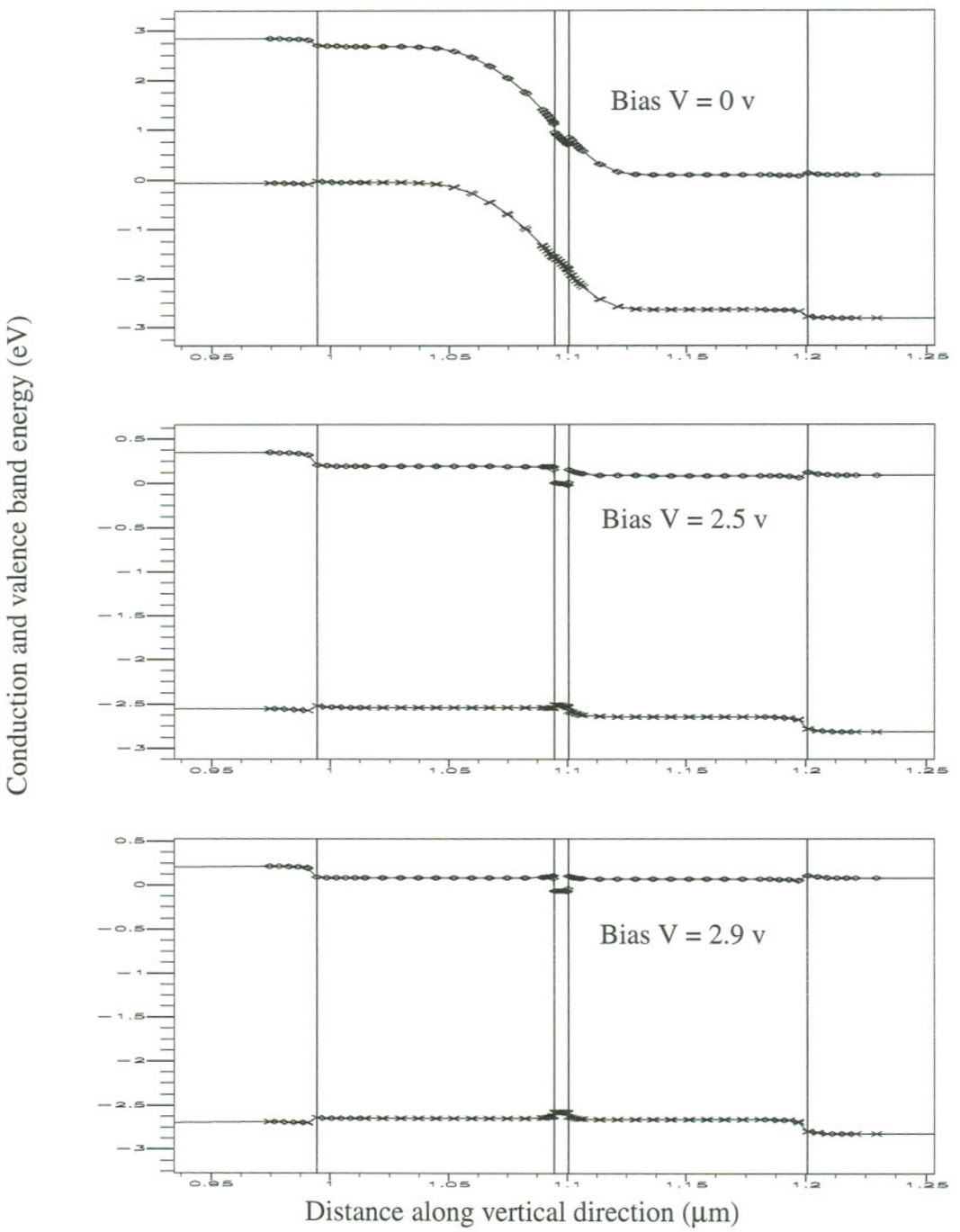

Figure 3-4: Band diagram under different bias voltages.

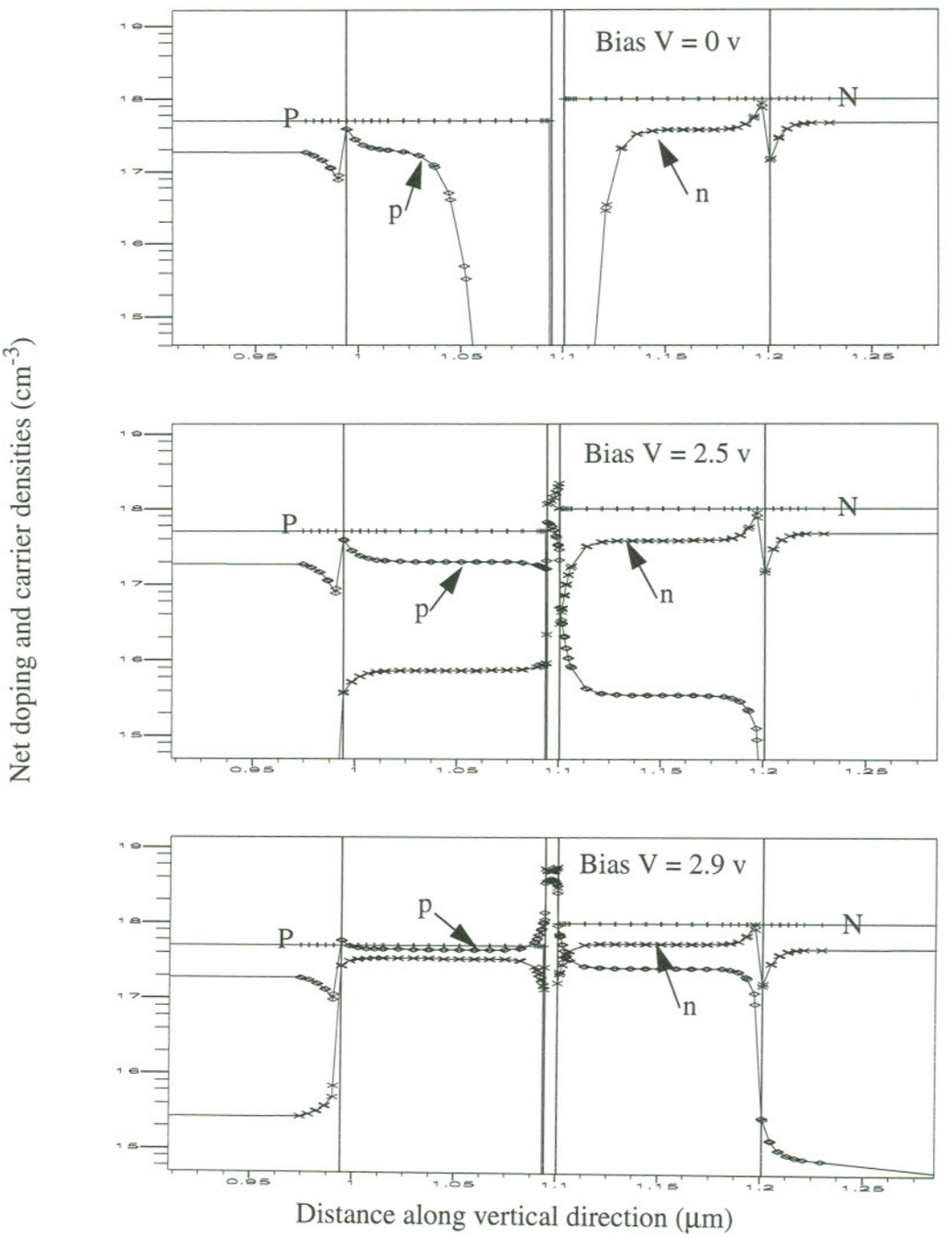

Figure 3-5: Net doping profile and carrier concentrations.

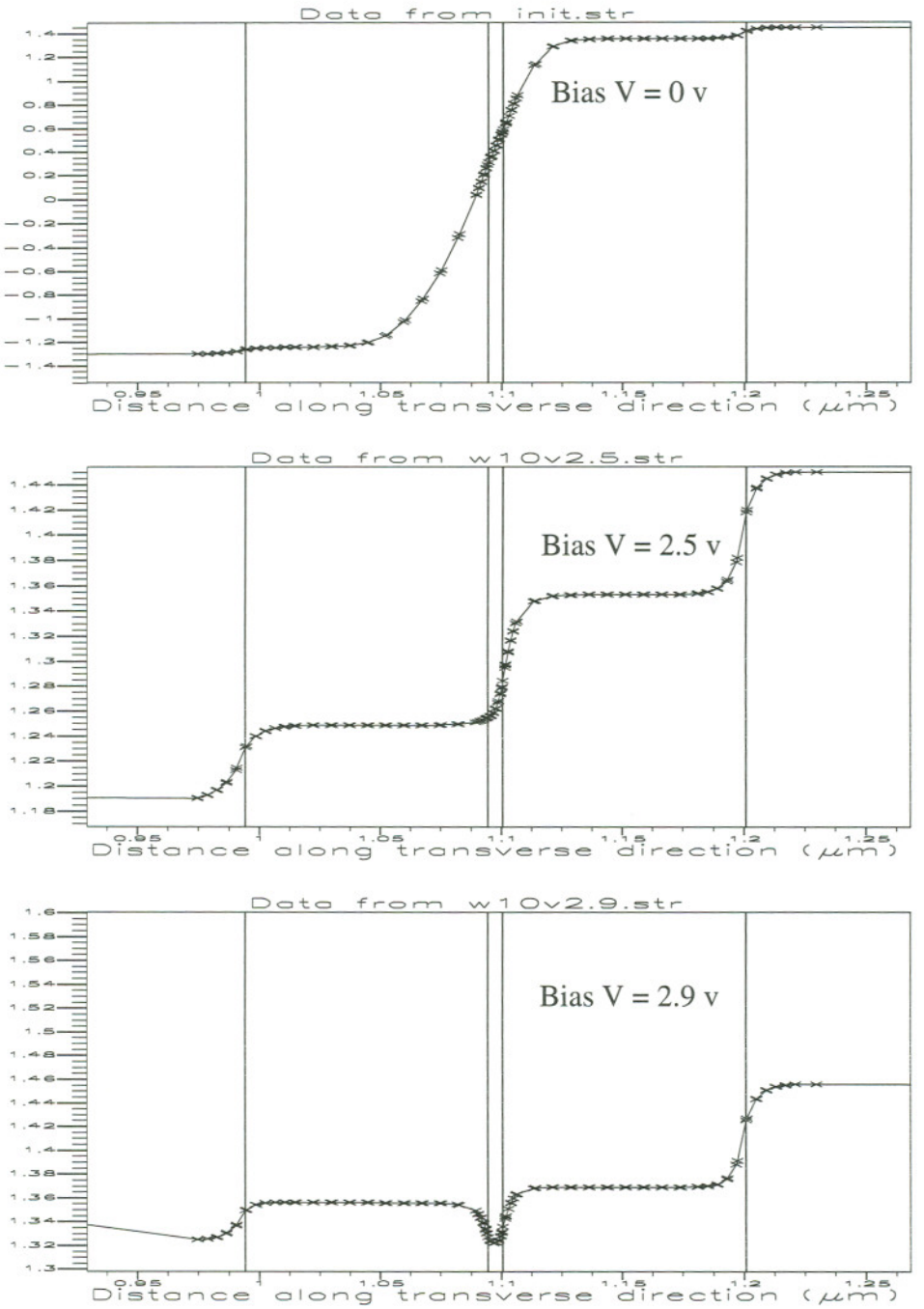

Figure 3-6: Potential distribution along vertical direction

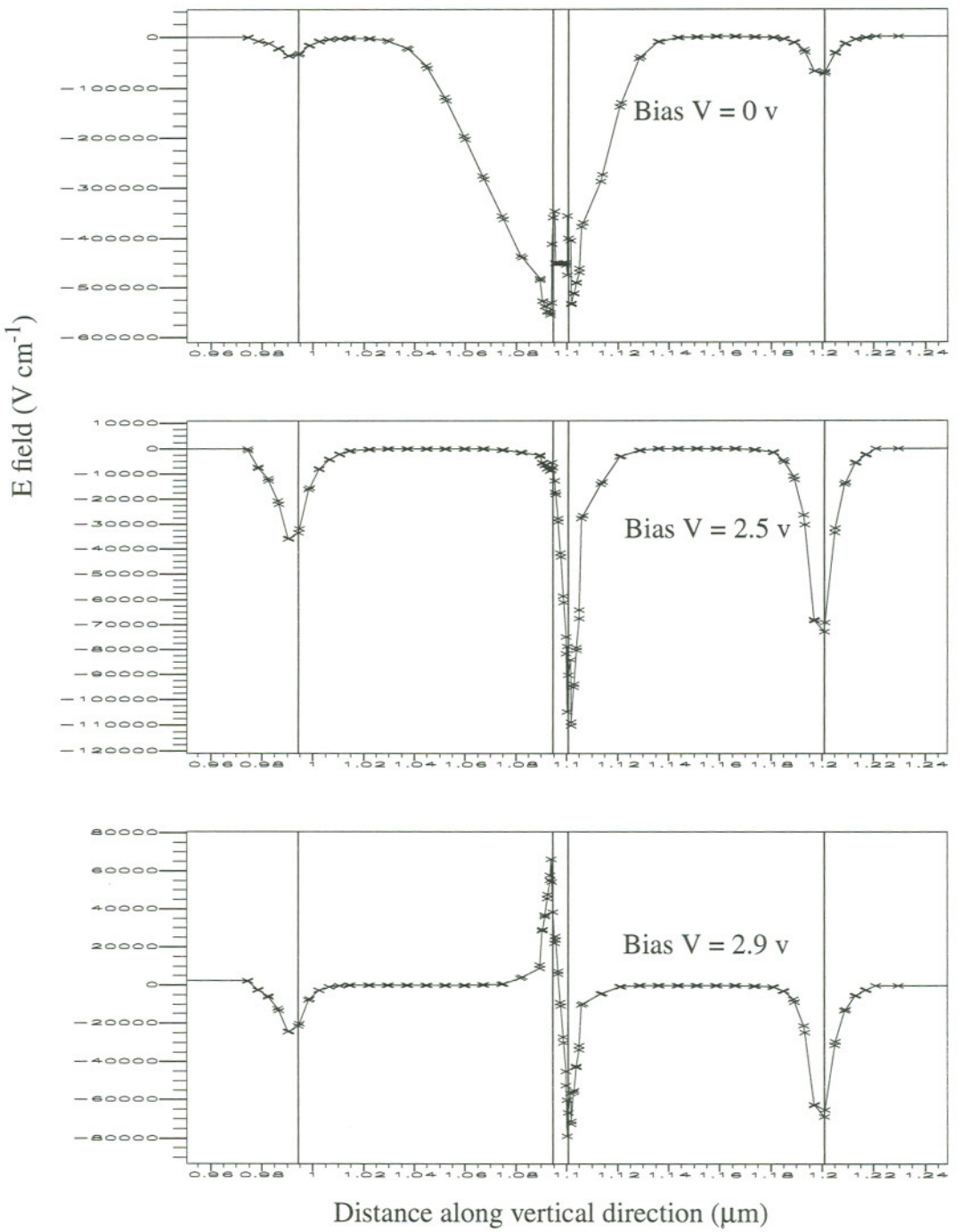

Figure 3-7: Vertical-transverse electrical field distribution.

3.3 Quantum confinement effect model

For active layer thinner than 20 nm, quantum confinement becomes significant. As mentioned early, the flat band gap in QW and barrier is a good approximation under forward bias. Also the injected carrier density in the QW region is fairly high becomes degenerated above certain bias. The detailed quantum effective modeling discussed in this section will based on these forward bias conditions. To emphasis the injected carrier induced space charge effect, it is assumed that the doping densities in both QW and barrier are negligibly low.

3.3.1 Schrödinger equation for electron envelope function

The fundamental theory necessary to provide an adequate description of the carrier distribution across a hetero-interface including quantum effect is based on the so-called envelope function approximation. The key assumption is that, within a given energy band, the electron wavefunction can be determined in terms of structural parameters such as the effective mass in both constituent crystals and the band discontinuity at the interface. In other words, the Bloch function is not a strong function of wave vector k and thus can be approximately represented by the band edge (k = 0) Bloch function.

For a one dimensional potential variation along the z axis such that U = U(z) represents the band-edge, as in the quantum-well case as shown in Fig. 3-1, we can assume the envelope function solutions to be of the form:[38]

$$F(x, y, z) = F_z(z)\exp[i(k_x x + k_y y)] \tag{3.11}$$

The one dimensional envelope functions $F_{e,i}(z)$ of electrons and $F_{h,i}(z)$ of holes are described by the effective-mass Schrödinger equations (i is the energy eigen-value number):

$$\left(-\frac{h^2}{2m_e}\frac{d^2}{dz^2}+U_e(z)\right)F_{e,i}(z)=E_{e,i}F_{e,i}(z),$$
$$\left(-\frac{h^2}{2m_h}\frac{d^2}{dz^2}+U_h(z)\right)F_{h,i}(z)=E_{h,i}F_{h,i}(z) \tag{3.12}$$

where, m_e and m_h are the effective masses, $E_{e,i}$ and $E_{h,i}$ are the quantized energy levels for confined states, $U_e(z)$ and $U_h(z)$ are the conduction and valence band-edge potentials, as defined in Fig. 3-8.

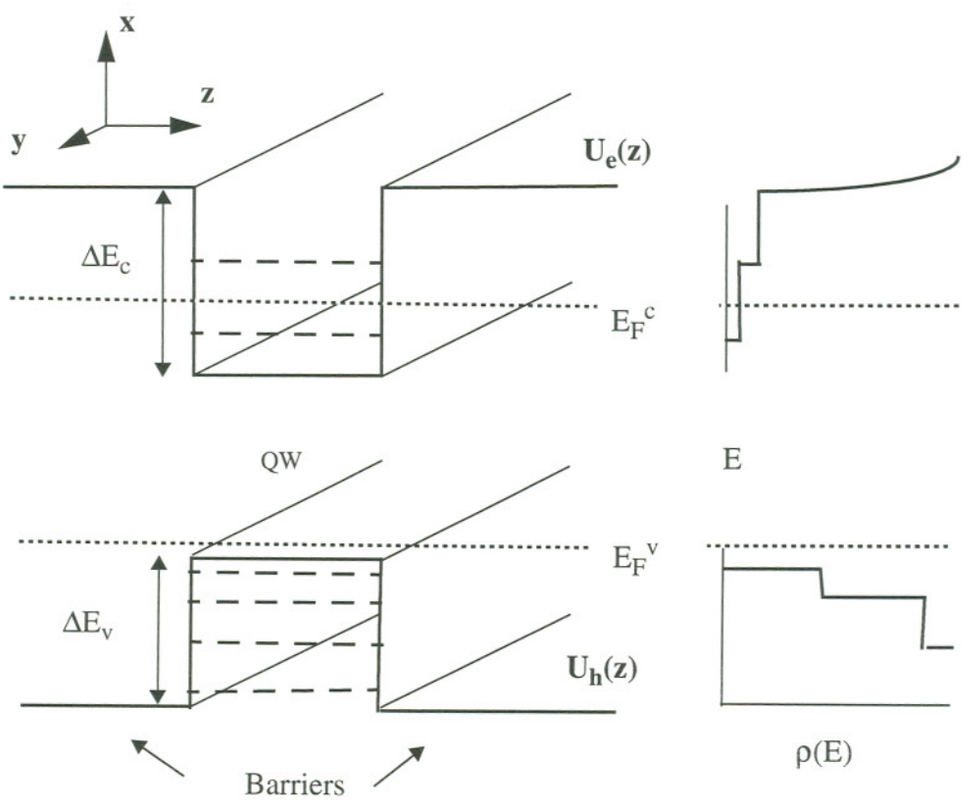

Figure 3-8: Quantum-well structure and density of states.

3.3.2 Carrier distribution and space charge effect in QW

Under the assumption that the quasi-Fermi levels across the hetero-junction are continuous. The carrier densities following the Fermi-Dirac distributions according to equations (3.6) and (3.7), are modulated by the quantum confinement effect. The two-dimensional carrier density distribution in the z-direction can be described by

$$\begin{aligned} n(z) &= k_B T \sum_i \left|F_{e,i}(z)\right|^2 \times \rho_{c,i} \times ln(1 + e^{(E_F^c - E_{e,i})/(k_B T)}), \\ p(z) &= k_B T \sum_i \left|F_{h,i}(z)\right|^2 \times \rho_{v,i} \times ln(1 + e^{(E_F^v - E_{h,i})/(k_B T)}) \end{aligned} \tag{3.13}$$

where k_B is Boltzmann constant and T is the temperature; and $\rho_{c,i}$ and $\rho_{v,i}$ are the density-of-states functions of electrons and holes of the i-th QW subband. Here, the sum is over all the confined states. For simplicity, band-mixing effects in the valence band are neglected and effective masses are assumed to be energy independent. So in a bulk semiconductor, the density-of-states is a parabolic function of energy. In QW, due to the energy split in z-direction, the density-of-states is step function. The total density-of-states function of both QW and barrier has been included in Fig. 3-8. The confined density of states (2-D) are[38]:

$$\rho_i^{2D} = 4\pi \frac{m_i}{h^2 L_z} \tag{3.14}$$

and the unconfined density of states (3-D, bulk):

$$\rho^{3D}(E) = 4\pi \left(\frac{2m}{h^2}\right)^{3/2} E^{1/2} \tag{3.15}$$

The total charge density at a given point z can be expressed by

$$\sigma_{tot} = q[p(z) - n(z)] \tag{3.16}$$

It is assumed that the doping densities in QW and barrier are negligibly low. If σ_{tot} is not equal to zero, as in the example discussed later in section 3.3.3, which is caused by the imbalance of electron and hole spatial distributions, then there is a space charge effect which will generate an electrostatic potential V(z) (in addition to U(z) in Fig. 3-8,) that is

described by the Poisson equation (3.1) in one dimension:

$$\frac{d^2}{dz}V(z) = \frac{q^2}{\varepsilon_o}[n(z) - p(z)]. \tag{3.17}$$

This additional V(z) will then be coupled with the original band profile U(z), and hence, alter the mobile carrier distributions. Thus, the effective-mass Schrödinger equations become:

$$\begin{aligned} \left(-\frac{h^2}{2m_e}\frac{d^2}{dz^2} + U_e(z) + V(z)\right)F_{e,i}(z) &= E_{e,i}F_{e,i}(z), \\ \left(-\frac{h^2}{2m_h}\frac{d^2}{dz^2} + U_h(z) - V(z)\right)F_{h,i}(z) &= E_{h,i}F_{h,i}(z) \end{aligned} \tag{3.18}$$

An accurate picture of carrier and potential distributions can be obtained through iteratively solving the coupled set of above Poisson and Schrödinger equations. The numerical solutions of the above problem are described as the flow chart in Fig.3-2. For detail of numeral methods see Appendix A.

3.3.3 Injection induced carrier confinement effect

In a QW laser diode, the carriers (electrons and holes) are mainly confined by the band offsets ΔE_c and ΔE_v between QW and barrier (core of optical guide). In real laser structures, ΔE_c and ΔE_v are often less than 0.2 eV. As the injection level becomes increasingly higher, the quasi-Fermi levels are raised and carrier distributions in the barriers increase. This carrier spill-over from the QW may become significant, especially in diode lasers operating at high temperature or in laser structures with low band offsets (poor carrier confinement). Generally, due to the structural difference between conduction and valence band, (e.g. electron-to-hole effective mass ratio is about 1/6 in ZnCdSe/ZnSSe based lasers), the spill-over of electrons and holes tend to be different. This will result in an internal electrostatic field which works to reduce the difference of the electron and hole

distributions, leading to the modification of the band profile, as described in section 3.3.2.

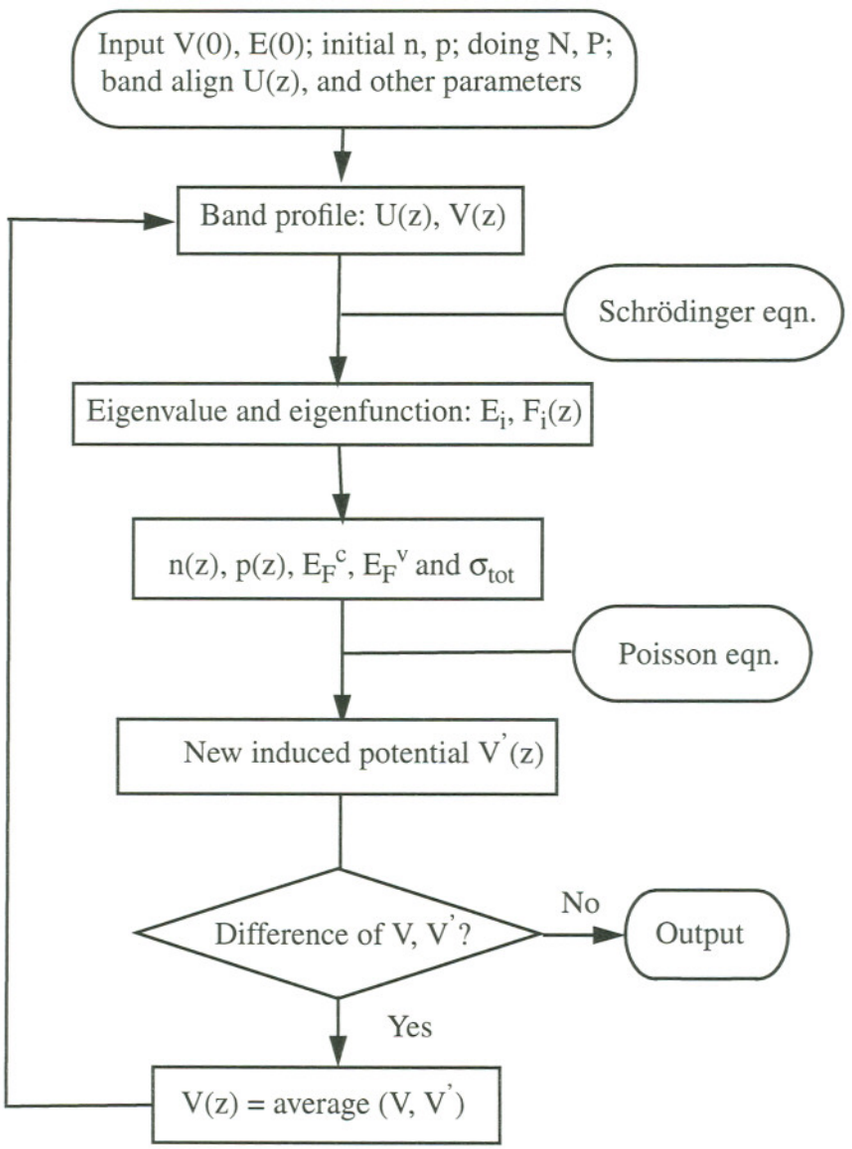

Figure 3-9: Flow chart of numerical solution.

An extreme case of this kind of injection-induced carrier confinement can be found in some laser structures where one of the conduction or valence band is completely flat or even slightly type-II. In such a case, it is still possible to get some carrier localization due to the electrostatic attraction generated by space charges as demonstrated in reference[39]. Even with structures that have type-I band alignment, the required threshold carrier density for lasing may be very high and thus the carrier confinement is relatively poor, as in many wide band-gap II-VI compounds based lasers. With the model described in section 3.3.2, it is possible to evaluate this injection-induced electrostatic confinement effect in gain/threshold current calculations for device design and optimization. Additionally, the quantitative modeling of this effect can help us gain more understanding about the influence on device performance of the band offset ratio $Q_c = \Delta E_c/(\Delta E_c+\Delta E_v)$, whose value at this time is still very difficult to predict, and help us to develop an effective band offset approach for more accurate carrier distribution calculation under the Q_c uncertainty.

As an example, the QW and barrier of previous studied device (SCH SQW $Cd_{0.2}Zn_{0.8}Se/ZnS_{0.06}Se_{0.94}$ 6.5 nm QW, 100 nm barrier) is used again to perform our numerical calculations based on the carrier distribution model developed in the previous sections. For simplicity and emphasis on the injected carriers, the net doping in both QW and barrier region is set to zero. The energy eigenvalues and wavefunctions are then calculated by solving the Schrödinger equations (3.12) in conduction and valence band, separately. The example of calculated energy levels have been shown in Figure 2-4. The calculated wave functions of the four energy levels of heavy hole are plotted in Figure 3-10. Once the wave functions are obtained, the carrier distribution can be calculated by equation (3.13) as shown in Figure 3-11. The initial band configuration is shown in Fig. 3-11a, as estimated from the strain effect and the common anion rule, as discussed in section 2.4.2. The Q_c value (refers to the split-off heavy hole band-edge) is about 0.62 in this case. The injection level n_{tot} or p_{tot} (measured by the total carrier density including contributions from both QW and barriers) is chosen to be about 5×10^{18} cm^{-3} which is close to the

threshold carrier density measured in the experiments. As we keep the total charge neutrality in the combined barrier and QW region (n_{tot} = p_{tot}), the locally unbalanced carrier distribution at this injection level is shown in Fig. 3-11c, where in this particular case there are more electrons in the QW and more holes in the barriers. The modification of the band profile due to the locally unbalanced carrier distribution, as shown in Fig.3-11b, is obtained by iteratively solving the coupled set of Poisson and Schrödinger equations as outlined in section 3.3.1 and section 3.3.2. The injection induced carrier confinement can be clearly observed when comparing the carrier distributions plotted in Fig.3-11c and 3-11d.

3.3.4 Effective band offset approach for QW structure simulation

As we mentioned earlier in section 2.4.2, the band offset of II-VI materials is quite uncertain at this time. However, from the above carrier distribution calculations we can see that the final carrier distribution and position of quasi-Fermi levels are not directly dependent on the original band offset value due to the re-adjustment of band profile. Thus, we can develop the following simplified approach and avoid the relatively complicated Poisson/Schrödinger iteration procedure for calculating the carrier distribution for each particular case.

The basic feature of this approach assumes that the injection induced space-charge distribution generates an interface dipole sheet, and this dipole sheet only changes the built-in potential of the hetero-junction. In other words, we use the band offset Q_c as an adjustable parameter to obtain the same quasi-Fermi levels as obtained by the comprehensive model. Interestingly, this is nearly equivalent of adjusting Q_c for charge neutrality in the QW as suggested from Fig. 3-11d.

Thus, an effective band offset Q_c (which, in general, could be injection level dependent) can be derived based on a square well calculation only, in which case an analytical solution is available. Hence, we can calculate the gain spectrum and the radia-

tive current including the influence of barrier recombination, in a simplified way. For simplicity, we will use a fixed effecitve Q_c in these examples. The detailed gain/current calculation examples using this approach will be given in chapter 4.

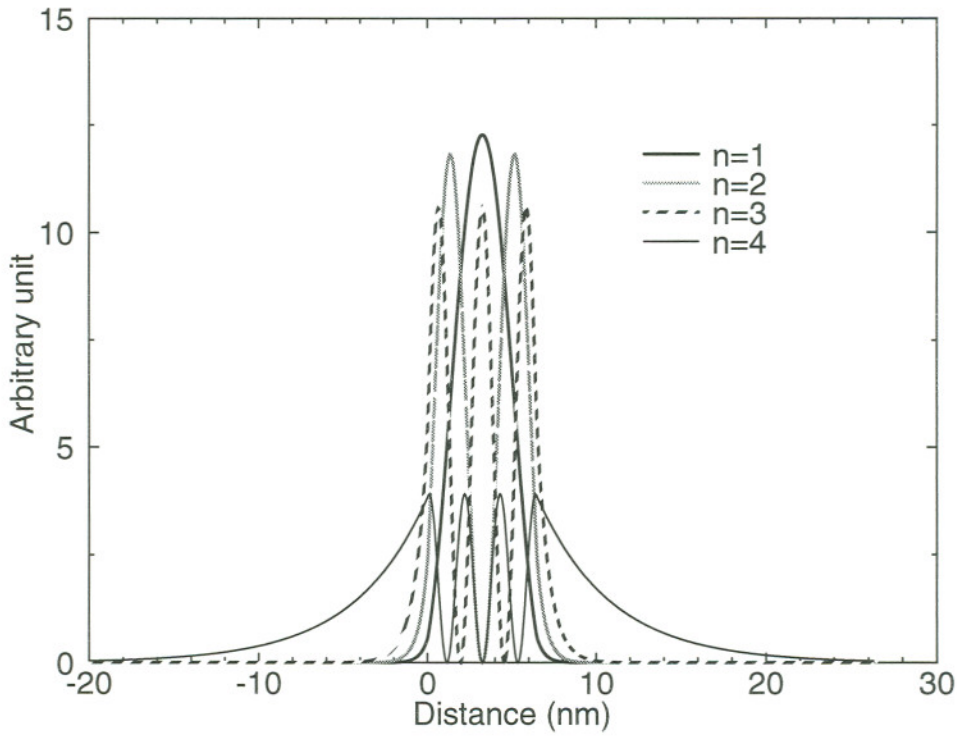

Figure 3-10: Heavy hole wave-functions in CdZnSe/ZnSSe QW.

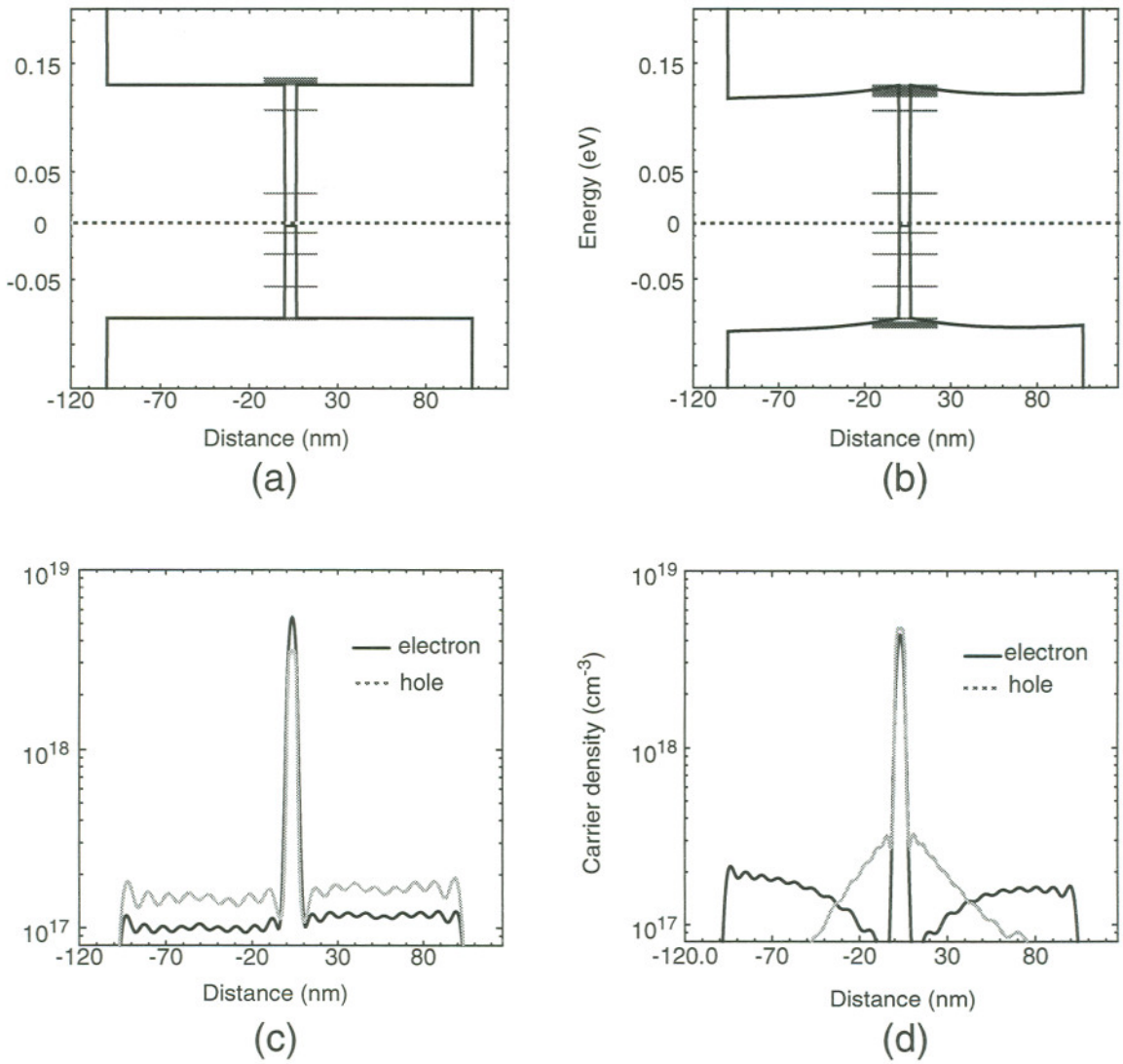

Figure 3-11: Band profile (without QW band gap) and carrier distribution.

(a) Initial band diagram. (b) Band diagram including injection induced carrier confinement(c) Unbalanced carrier distribution of configuration (a). (d) balanced carrier distribution ofconfiguration (b)

3.4 Summary

In this chapter, the electrical model for both bulk heterostructure and QW have been developed. Electron and hole distributions of a CdZnSe/ZnSSe/MgZnSSe QW laser diode in both cases have been studied in detail. In the bulk model, carrier and current distribution have been obtained under the incomplete ionization conditions. Although the free carrier density is relatively low in the cladding, sufficient carrier injection in QW still can be obtained at room temperature without field ionization involved. Relatively high field have been observed locally in barrier region close to QW during the bulk simulation. I - V characteristic is also calculated including the radiative recombinations.

The long-range Coulomb interaction between electrons and holes in the barrier and QW regions has been taken into account and the injection induced carrier confinement in the QW has been modeled. The above carrier distribution model is very important in other device modeling applications. A well known example is the HEMT (high electron mobility transistor), in which case only one carrier (electron) has to be considered. In some special cases of QW laser modeling, this model is also important, and more generally, it can provide us an effective band offset concept, which is very helpful for device simulation of heterojunctions which band offsets have not been very well characterized. In this chapter, the numerical model of a HEMT simulator has been expanded to a more general case in which both electrons and holes are taken into account at the same time. An effective band offset approach has been developed for simplifying of Poisson equation calculations. In the next chapter, this approach will be applied to the local optical gain modeling of a SCH QW laser.

Chapter 4 DESIGN AND SIMULATION OF II-VI QW LASER DIODE

4.1 Introduction

Based on the material studies and electrical models developed in chapter 2 and 3, this chapter discusses the computer simulation of II-VI QW laser diodes with the incorporation of optical modeling. For the current development stage of II-VI blue green laser diodes, the threshold characteristics are of major concern. Thus, only the steady-state model is considered and the optimization is aimed at low threshold operation. Simulation results on the structure dependence of the optical gain coefficient and the threshold current density J_{th} for CdZnSe/ZnSSe/MgZnSSe SCH SQW diode lasers will be presented. Device optimization in both vertical and lateral transverse dimensions will be discussed.

The challenge of developing an effective modeling approach is that, due to the complicated device structure such as a QW laser, one often needs to deal with different levels of physical detail at a different scale. In QW laser modeling, the description of electron behavior in the QW region requires solving the Schrödinger equation as described in section 3.3, while in the barrier and cladding regions a conventional DD model is sufficient. In this chapter, two types of device models will be used to obtain an accurate description of the device performance with great computational efficiency allowing to explore the influence of a variety parameters. A one-dimensional in-house simulation program based on a full physical description including the quantum confinement effect (as described in section 3.3) is used to determine local optical gain spectra as a function of vertical-transverse parameters such as QW and barrier length, L_{qw} and L_{ba}, as well as band gap and refractive steps. A semi-empirical approach which combines QW calculation results with a versatile commercial two-dimensional device simulator (SILVACO

ATLAS-LASER), which is based on the conventional model described in section 3.2, has been employed for lateral properties and modeling of the above-threshold laser characteristic. The approach has the advantages that it can handle both electrical and optical behavior in a two-dimensional fashion (lateral and vertical) without losing the local detail of the quantum effect for the QW local gain and spontaneous emission rate.

In this chapter, the optical model and optical-electrical interaction in a laser diode, which will be used in 2-D laser modeling, is introduced first. Followed by a physical modeling of local optical gain and spontaneous emission rate in the QW. From which, vertical parameters optimization for low threshold operation are obtained and phenomenological gain and spontaneous emission coefficients are derived. Then, a 2-D simulation of QW laser are performed, based on phenomenological model and the optical-electrical interaction calculations, with emphasized on the lateral effects modeling.

4.2 Electrical and optical interaction in laser diode

The simulation of a laser diode requires both electrical and optical behavior modeling. By introducing the optical wave equations as additional basic equations, optoelectronic devices such as DH lasers can also be simulated with the conventional model introduced in section 3.2. Currently, most of the available LD simulation CAD tools are based on such an approach.[6,40-43]

4.2.1 Optical field modeling

As a good approximation, the electrical model can be defined by equations (3.1) - (3.2) described in section 3.2. The optical model follows the so called effective permittivity formalism, as outlined by Wilt and Yariv[40]. The optical field *E(y, z)* of TE mode in the transverse y, z plane is given by a 2-D Helmholtz equation:

$$\nabla^2_{yz} E(y,z) + \left(\frac{\omega_m^2}{c^2} \varepsilon_\infty(y,z) - \beta^2 \right) E(y,z) = 0 \tag{4.1}$$

where, ω_m is the frequency corresponding to longitudinal mode m; c is the velocity of light in vacuum and $\varepsilon_\infty(y, z)$ is the high frequency dielectric permittivity, which is related to the local optical gain as follows:[6]

$$\varepsilon_\infty(y,z) = n_o^2 + (-\alpha + i)\frac{c n_o g(y,z)}{\omega} \tag{4.2}$$

where n_o is the real refractive index, α is a line width broadening factor, and g(y, z) is the local optical gain. A physical gain model of the QW will be discussed in section 4.3.1.

The photon density S_m of longitudinal mode m is given by the photon rate equation:

$$(G_m - R_L)S_m + R_{sp}^m = 0 \tag{4.3}$$

where G_m is the mode gain of longitudinal mode m, R_L is the total cavity loss and $R_{sp}{}^m$ is the spontaneous-emission rate coupled into mode m.

4.2.2 Radiative recombinations

The net stimulated-emission recombination rate is related to the photon density S and optical field **E** as:

$$R_{st} = \frac{c}{n_{eff}} g S |\boldsymbol{E}|^2 . \tag{4.4}$$

An empirical spontaneous-emission recombination rate is given by:

$$R_{sp} = B(np - n_{ie}^2) \tag{4.5}$$

where n_{ie} is the effective intrinsic carrier concentration[6], B is the radiative constant which depends on carrier density and temperature. It can be derived from the physical spontaneous-emission rate which will be introduced in section 4.3.

Equations (4.1) - (4.5) along with the equations (3.1) -(3.6) give a full description of the laser diode operation.

4.2.3 Threshold condition of laser diode

In the photon rate equation (4.3), the model gain G_m is related to local gain g_m as:

$$G_m = \Gamma g_m \tag{4.6}$$

The optical confinement factor Γ represents the fraction of the mode energy contained in the QW active gain region.

The total losses are

$$R_L=\alpha_m + \alpha_{int}. \tag{4.7}$$

where

$$\alpha_m = \frac{1}{2L}\ln\left(\frac{1}{R_1 R_2}\right) \tag{4.8}$$

is the mirror loss and accounts for the radiation escaping from the FP cavity because of finite facet reflectivities R_1 and R_2, and α_{int} describes the internal losses in the wave guide, such as free-carrier absorption. The threshold condition of laser diode is given by $G_m = R_L$.

4.3 1-D (vertical) modeling of ZnCdSe/ZnSSe/MgZnSSe SCH QW laser

QW laser structures have superiority in performance over conventional double-hetero (DH) structures. A fundamental advantage of QW laser is that it delivers more gain per injected carrier than the conventional DH lasers, which results in lower threshold currents. In the QW region, the optical field change can be neglected. The local optical gain and spontaneous-emission spectrum can be calculated based on the effective band offset approach developed in section 3.3.4, as will be described in section 4.3.1. Then, the

peak-gain and radiative current vs. carrier density relations will be derived. Based on the material studies of chapter 2, a variety of composition combinations of barrier and cladding, which are all lattice matched with the GaAs substrate, have been interpolated. The composition, band gap and refractive index of these alloys are plotted in Figures 4-1 and 4-2, where the label A, B.. stand for the alloys used for barrier and cladding in device simulation. Thus, the different devices can be identified according to their barrier/cladding combinations, such as A/C. The calculation is first performed on the commonly used laser structure with a $Cd_{0.2}Zn_{0.8}Se$ QW, a $ZnS_{0.06}Se_{0.94}$ barrier (composition A) and a $Mg_{0.1}Zn_{0.9}S_{0.14}Se_{0.86}$ cladding layer (composition C)[47], whose electrical behaviors have been discussed in chapter 3. Then the model is applied to the other barrier/cladding combinations with the same QW. Finally, the influence of QW is considered. Based on the above steps, the vertical parameters of a ZnCdSe/ZnSSe/MgZnSSe QW laser are established.

4.3.1 QW gain spectra calculation

The relationship between gain, and injected carrier density in laser diode is highly structure dependent and therefore the modelling of the gain/carrier density relation will provide invaluable insight for device design. The goal of our studies is to arrive at a flexible modeling program that allows to elucidate trends in a large parameter space and can be easily applied to a variety of different material systems, rather than a sophisticated procedure that generates highly accurate data for specialized situations. Hence, we adopted a simplified theoretical approach to the gain/injection rate calculations[38] based on the electron-hole plasma picture (EHP). The controversial issue of the possible strong exciton effects, as argued by Ding et al.[44] will not be consider here.

Once we have obtained the carrier densities, following the approach described in section 3.3.2, the quasi-Fermi levels can be derived by equations (3.6)-(3.7) in both conduction and valence band. For simplicity, continue quasi-Fermi levels across the

heterojunctions are assumed. Then the gain spectra can be calculated from the so-called band-to-band recombination formalism (EHP assumption). The EHP model has been demonstrated to be very successful in III-V type laser modeling and also has been applied to II-VI blue green lasers[45].

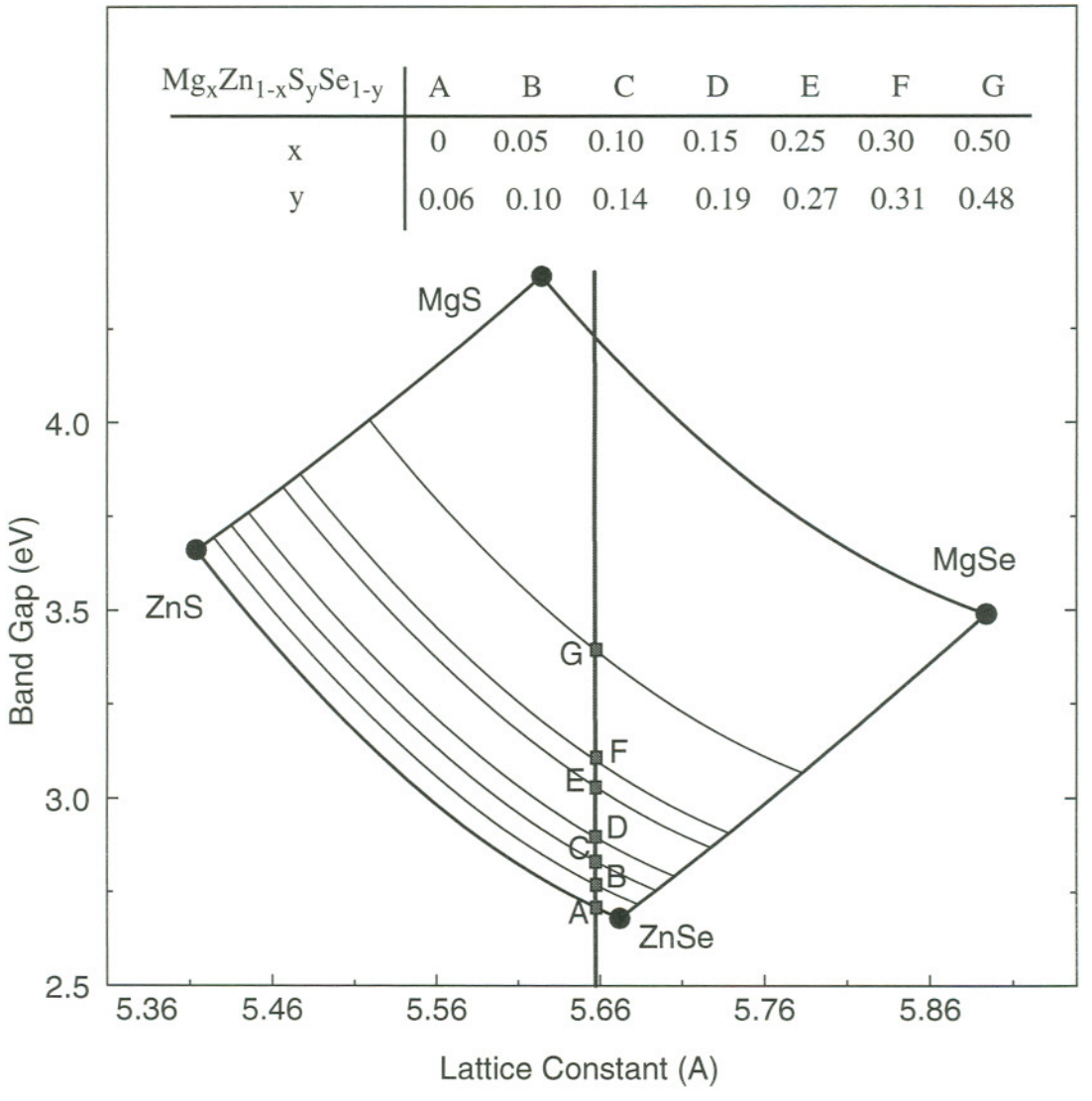

Figure 4-1: MgZnSSe alloys lattice matched with GaAs.

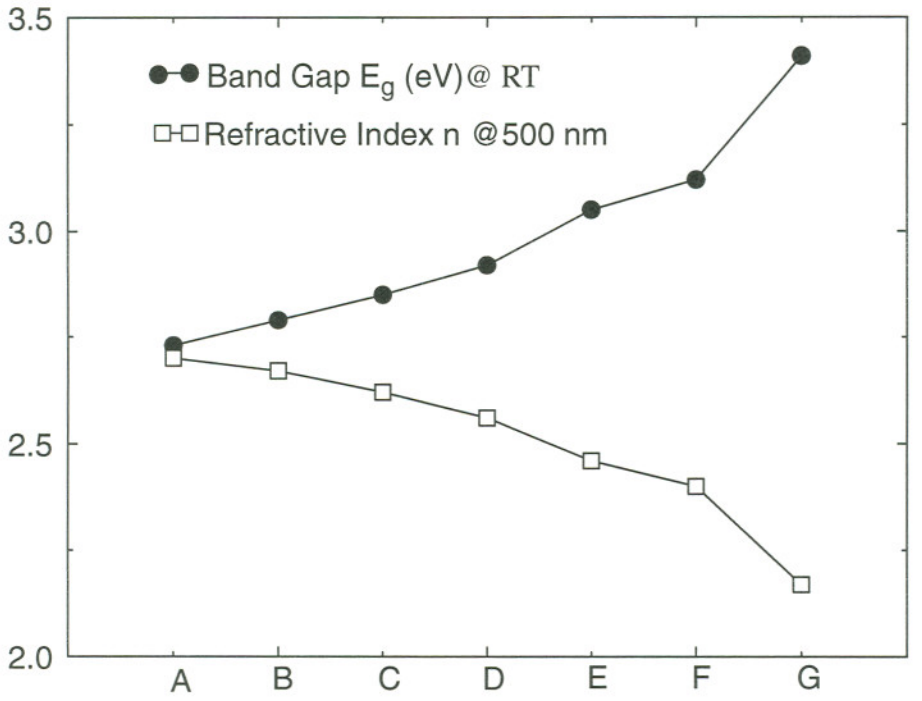

Figure 4-2: Refractive index at 500 nm wavelength and band gap at 300 K of the alloys A, B, C....

The detailed gain calculation procedure follows closely Ref.[38]. The optical gain experienced by an incoming photon with energy hω is determined by:

$$g(h\omega) = \left(\frac{1}{h\omega}\right)\frac{\pi q^2 h}{\varepsilon_0 n c m_0^2} u_{jn} M_T^2 \rho(E_{eh} - E_g)(f_c - f_v) \quad . \tag{4.9}$$

where, $\rho(E_{eh}\text{-}E_g)$ is called the reduced carrier density of states, and M_T is the bulk transition matrix element. The polarization effect for the stimulated transition (i.e. TE vs. TM) due to the anisotropy of the QW structure and compressive strain effects were included in the term u_{jn}.

The intraband relaxation effect on the optical gain spectra was taken into account assuming combined Lorentzian broadening of electron and hole states with a fixed intraband relaxation time τ_s, providing the following broadening formulation

$$L(E_{eh}) = \frac{1}{\pi}\frac{(h/\tau_s)}{(E_{eh} - h\omega)^2 + (h/\tau_s)^2} . \tag{4.10}$$

Where the broadened gain follows from the convolution

$$g(h\omega) = \int g(h\omega) L(E_{eh}) dE_{eh} . \tag{4.11}$$

The spontaneous emission rate is also calculated as:

$$R_{sp}(h\omega) = \left(\frac{1}{h\omega}\right)\frac{\pi e^2 h}{\varepsilon_0 n c m_0^2} u_{jn} M_{ave}^2 \rho(E_{eh} - E_g) f_c (1 - f_v) , \tag{4.12}$$

where $M_{ave}^2 = 1/3\ M_T^2$. The total radiative current is then obtained from

$$J_{rad} = q \int R_{sp}(h\omega) d(h\omega) . \tag{4.13}$$

In our model, the gain and spontaneous emission due to the barriers are also calculated and added to the total gain and spontaneous emission spectra.

The total radiative current density J_{rad} has a QW component J_{qw} and a barrier component J_{ba}, so $J_{rad} = J_{qw} + J_{ba}$. Each component can be calculated from the sponta-

neous emission:

$$J_{qw} = qL_{qw}\int_{E_n} R_{sp}^{qw}(h\omega)d(h\omega) \tag{4.14}$$

$$J_{ba} = 2qL_{ba}\int_{E_b} R_{sp}^{ba}(h\omega)d(h\omega) \tag{4.15}$$

where q is the electronic charge, L_{qw} and L_{ba} the thickness of the QW and single-side barrier regions, respectively; E_n is the QW spectral range and E_b is the barrier spectral range.

An effective band offset $Q_c = 0.53$ has been derived by comparing the quasi-Fermi levels as calculated from the simple square well Schrödinger equation with those calculated from the comprehensive model based on the coupled Poisson and Schrödinger equations at injection levels near threshold (see section 3.3). Using this fixed effective Q_c, for all injection levels considered, the band configuration of a simple square well is used for the gain modeling program (gns.f, see Appendix B). The inputs of the program include device geometry parameters, temperature, band offset ratio, intraband relaxation time τ_s and injected carrier density. Based on different injection levels as measured by the total carrier density at certain temperature, gain and spontaneous emission spectra are calculated. Examples are plotted in Figure4-3 and 4-4 for device A/C.

4.3.2 Threshold current density and temperature relation

The total radiative current is then obtained by integrating the spontaneous emission spectrum at each injection level. The position of the maximum gain peak of the gain spectra is automatically located for each injection level by a data process program (fdpk.sel, see Appendix B). The peak gain vs. injected carrier density n and radiative current J_{rad} vs. n relations are thus obtained. Examples are plotted in Figures 4-5 and 4-9. The threshold current density can be determined from the threshold gain which is about

1300 cm^{-1}, as estimated from the total cavity loss (assume uncoated facet) and the confinement factor Γ. A computer program for the calculation of complex modes of electromagnetic wave propagation in plane-layered dielectric structures called MODEIG [46], is used for optical wave guide modeling and Γ calculation. The total cavity loss is estimated as about 23 cm^{-1} by assuming a 1 mm long cavity length and 8.1 cm^{-1} internal loss with an uncoated facet. The temperature dependence of both internal losses and the intraband relaxation time are neglected for simplicity of calculations.

The above procedure for threshold current density is repeated for the temperature region from 85K to 394K. From the J_{th} vs. temperature relation plotted in Figure 4-7, one can see that the modeling results agree well with experimental data[47] when choosing an intraband relaxation time τ_s = 0.1 ps. This value is somewhat larger than reported for a more complicated model[45,48] but consistent with GaAs data. It should be noted that for simplicity, a possible temperature dependence[45] of τ_s and α_{int} has been ignored in this approach.

4.3.3 Design and optimization of vertical parameters

The next step is to use the above gain modeling approach for optimizing the structure parameters of the CdZnSe/MgZnSSe SCH QW laser diode for low threshold current density operation. The design and optimization of vertical parameters are basically based on trade-off between electrical and optical confinement. The the optical waveguide modeling shows that for the commonly used laser structure with a $Cd_{0.2}Zn_{0.8}Se$ QW, a $ZnS_{0.06}Se_{0.94}$ barrier and a $Mg_{0.1}Zn_{0.9}S_{0.14}Se_{0.86}$ cladding layer (device A/C), the barrier size L_{ba} on each side of the QW which provides the maximum Γ is about 100 nm as compared with 250 nm used in Ref. 47, as shown in Figure 4-7. Thus, at RT J_{th} could be reduced from 554 to 399 A cm^{-2} just by optimizing the barrier size. However, a

$ZnS_{0.06}Se_{0.94}$ barrier still provides only a relatively small band gap difference to the strained $Cd_{0.2}Zn_{0.8}Se$ QW, leading to an insufficient band offset for preventing carrier spill-over into the barrier.

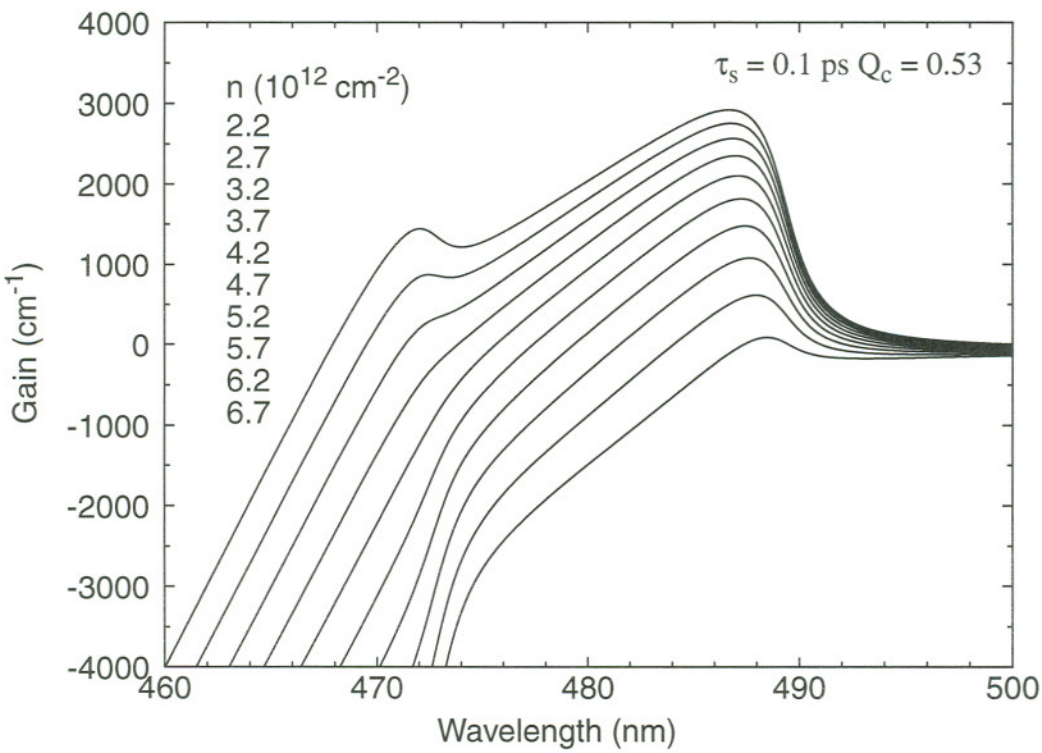

Figure 4-3: Local gain spectra (TE) at different injection levels of device A/C at 300 K.

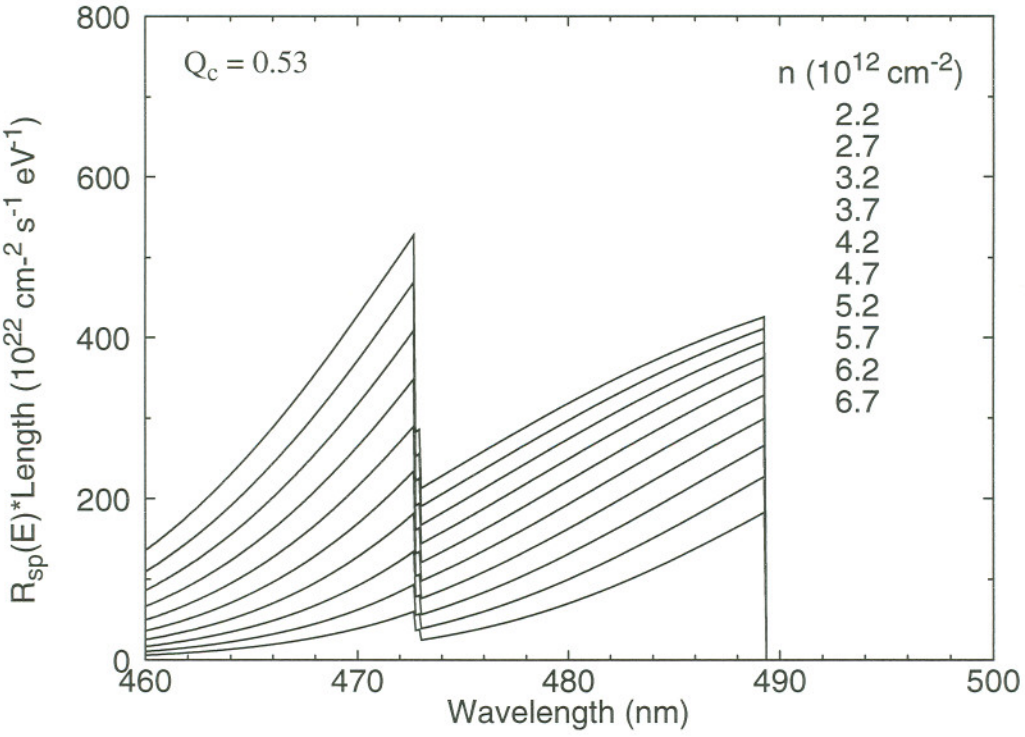

Figure 4-4: Spontaneous emission spectra at different injection levels of device A/C at 300K (without broadening).

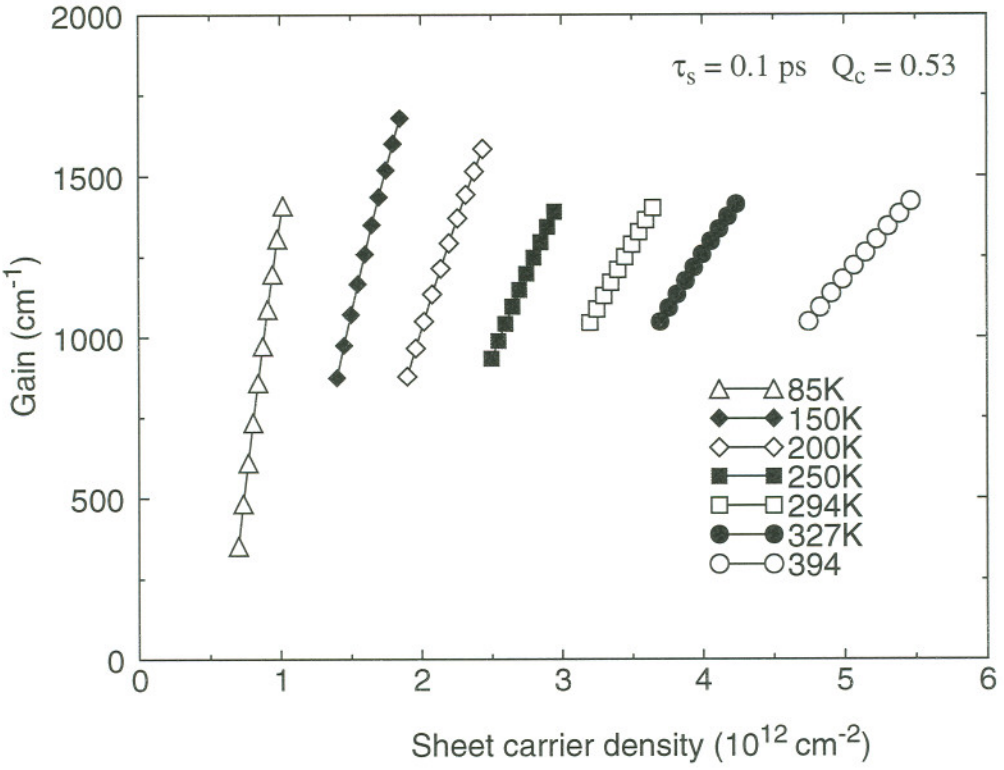

Figure 4-5: Gain peak vs. injection levels for different temperatures.

Regression of set 0 results to set 1
Number of observations = 10
A[0] is the constant, A[i] is the coefficient for ith power of X
A[0] = -69.6548521
A[1] = 6.46586909e-11
A[2] = 2.38910303e-23
R square = 0.9999688
Avg Y = 740.4537
Sdev Y = 422.259
Avg X = 4.45e+12
Sdev X = 1.513825e+12

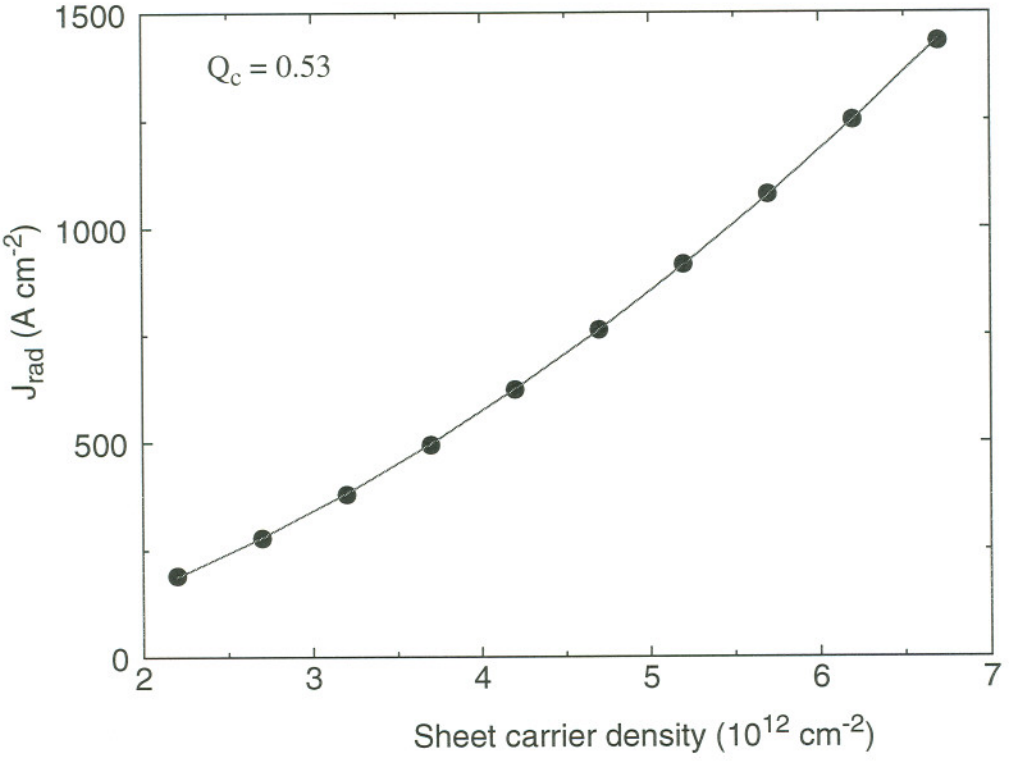

Figure 4-6: Radiative current vs. injected carrier density at 300 K and regression results.

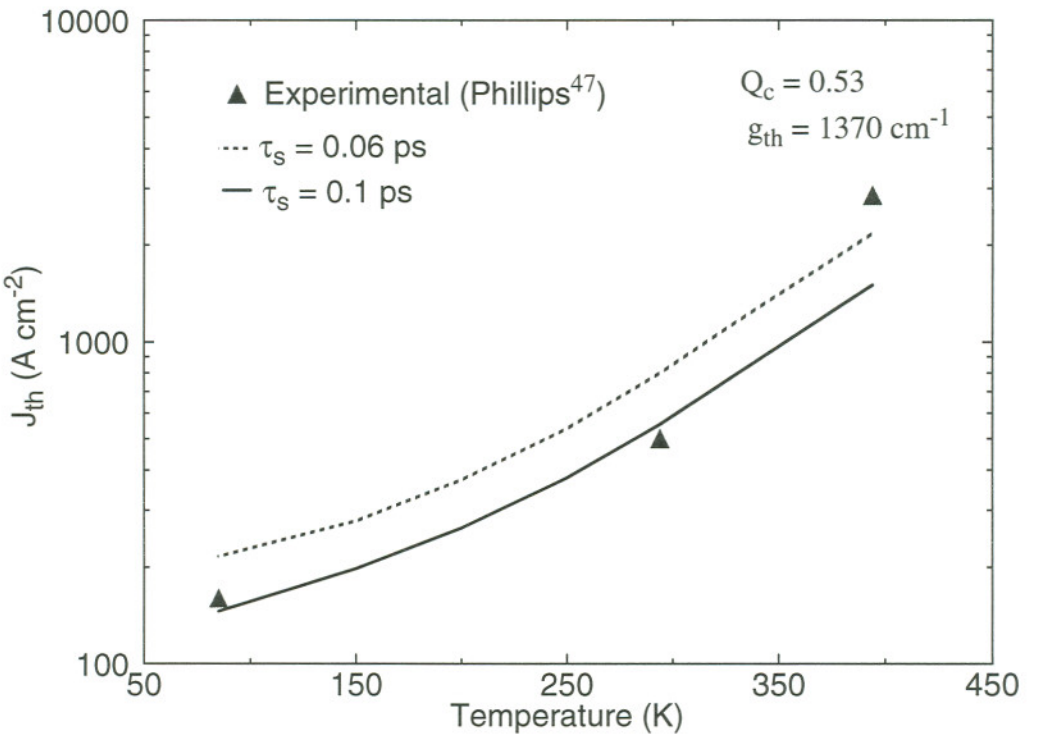

Figure 4-7: Calculated threshold current density of device A/C.

To eliminate such spill-over, we propose an improved configuration by using a $Mg_{0.05}Zn_{0.95}S_{0.1}Se_{0.9}$ layer (composition B) with a larger band gap E_g = 2.79 eV as barrier material. This reduces the optimized J_{th} value to 376 A cm^{-2}. For better optical confinement, the cladding layer requires increased Mg content as summarized in Figures 4-1 and 4-2. The optimized J_{th} at RT for a $Mg_{0.5}Zn_{0.5}S_{0.48}Se_{0.52}$ cladding layer (composition G) is predicted to be as low as 224 A cm^{-2}.

Finally, the threshold current density vs. QW thickness L_{qw} relations are calculated for a $Cd_{0.2}Zn_{0.8}Se$ QW with the two different barrier/cladding combinations as shown in Figure 4-9. It appears that the optimized L_{qw} is in the range of 4.5-6.5 nm in both case.

Thus, the vertical structure parameters of ZnCdSe/MgZnSSe SCH SQW diode lasers were optimized for low threshold current density operation by modeling the optical gain based on the electron-hole plasma theory, and the optical confinement factor Γ in the SCH waveguide. A substantial reduction in threshold current density from 554 A cm^{-2} in the commonly used laser structure to as low as 224 A cm^{-2} is predicted.

4.4 2-D simulation of ZnCdSe/ZnSSe/MgZnSSe SCH QW laser

In practical laser diode devices, the current in the lateral direction is often confined through various fabrication techniques to reduce the total operation current and control the optical mode laterally. In a gain-guided SCH QW laser structure as shown in Figure 2-5 as well as its cross section shown in Figure 3-1, the stripe geometry is used for this purpose. The variation in the optical gain g(y) in the lateral direction leads to the confinement of the lateral modes. Carrier diffusion plays an important role here. The problem of lateral-mode determination for a gain-guided laser diode is an extremely complicated process, a numerical approach is generally required. In this section, the coupled electrical and optical equations will be solved self-consistently in both vertical and lateral (y and z) directions for a

gain-guided ZnCdSe/ZnSSe/MgZnSSe SCH QW laser based on the model introduced in section 4.1 combined with some phenomenological parameters based on results from section 4.3. The threshold dependence on stripe width of such device will be determined.

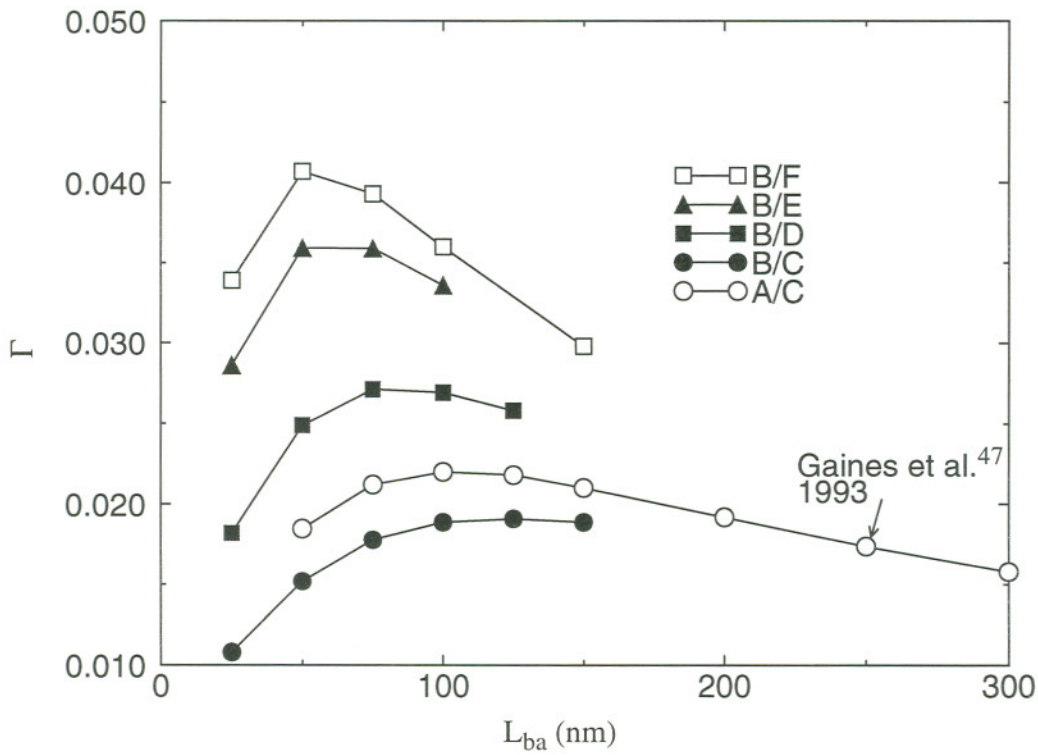

Figure 4-8: Optical confinement factor vs. barrier width of different barrier/cladding combinations, with the same QW ($Cd_{0.2}Zn_{0.8}Se$, L_{qw} = 6.5 nm).

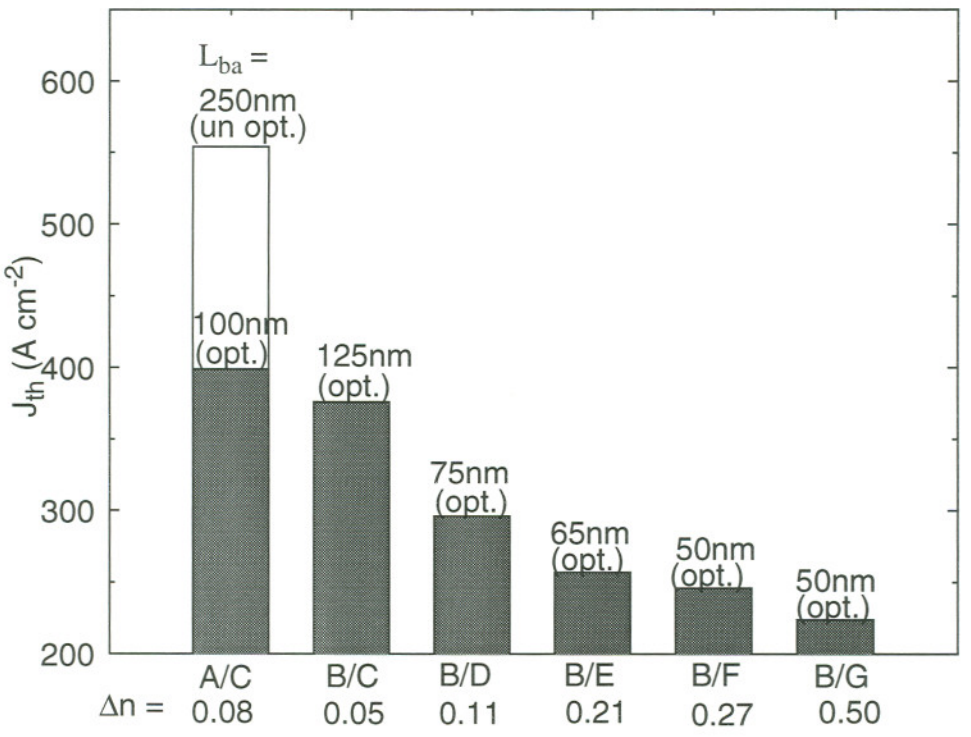

Figure 4-9: Threshold Current Density J_{th} of Different Barrier/Cladding.

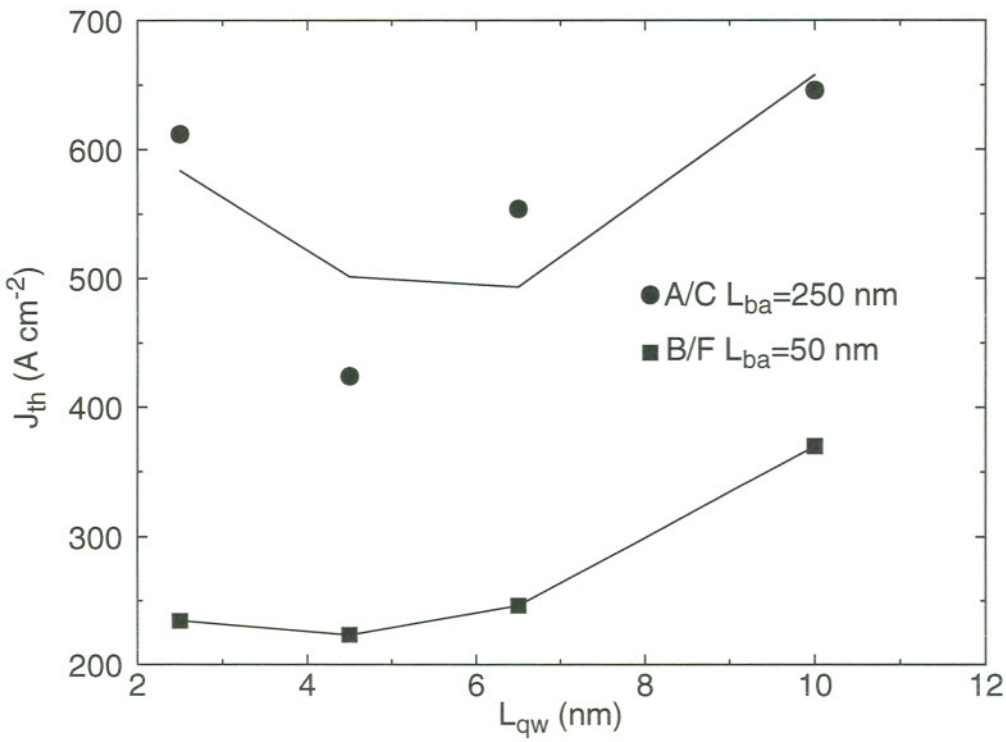

Figure 4-10: Threshold current density vs. L_{qw} of device A/C and B/F.

4.4.1 Phenomenological gain and spontaneous-emission model

A phenomenological gain relation is defined by the following equation:[6]

$$g(x, y) = g_{00} + g_{1n} \cdot n + g_{1p} \cdot p + g_{2np} \cdot np + g_{1min} \cdot min(n, p). \quad (4.16)$$

Parameters g_{00} ~ g_{1min} can be determined by fitting the gain - carrier density relationship obtained by 1-D calculation of previous section.

In this case we have n=p and by linear fitting the g - n relation (Figure 4-5) and quadratic fitting the J - n relation (Figure 4-6) around the injection range close to estimated threshold carrier densities, the following results for room temperature operation are obtained:

g_{00} = -1988 (cm^{-1}), g_{1min} = 6.6 x 10^{-16} (cm^{-1}), and g_{1n} = g_{1p} = g_{2np} = 0.

B = 9.8 x 10^{-11} (cm^3 s^{-1}).

These results along with the other material parameters are used as independent input data for the 2-D device simulation.

4.4.2 Stripe geometry structure design based on 2-D model

The dependence of threshold current on stripe width in gain-guided QW lasers has been extensively studied in III-V devices.[66] It has been observed that the gain-induced anti-guiding effect is extremely strong in strained-layer InGaAs/GaAs QW lasers which is totally different from unstrained GaAs/AlGaAs QW lasers.[67] For strained CdZnSe/ZnSSe/ ZnMgSSe SCH QW lasers, various stripe widths such as 5 μm,[68] 20 μm[10] and 50 μm[47] have been used by different research groups. However, a systematical study on the threshold current dependence vs. on stripe width in these device has not been reported yet. The 2-D numerical model of QW lasers developed in this section provides a useful tool to investigate this problem theoretically as illustrated below.

First, consider the widely used laser structure device A/C with a $Cd_{0.2}Zn_{0.8}Se$ QW, a $ZnS_{0.06}Se_{0.94}$ barrier and a $Mg_{0.1}Zn_{0.9}S_{0.14}Se_{0.86}$ cladding layer. The cross section of

this device has been shown in Figure 3-1, which has a stripe contact of width W = 10 μm. The electrical behavior, such as the V - I characteristic, was obtained in section 3. When the applied bias exceeds 2.5 volts, the optical field calculation and electron-photon interaction are included in the simulation. The initial effective index, photon density and cavity losses are specified as input parameters. Only one longitudinal mode is considered in the simulation with a specified wavelength (500 nm). As the bias voltage goes above 2.9 V, laser oscillations begin to occur. With the coupled optical field modeling, the optical mode pattern at 3.2 volts, the L-I curve, G-I curve and V-I curve were calculated as well as shown in Figure 4-11. The plotted currents are normalized to the longitudinal dimension (cavity length L=1mm). Thus, the threshold current for the chosen 1 mm cavity length is about 137 mA in this case. The corresponding average current density value is about 1.4 kA/cm^2, which is substantially higher than the result previous calculated in the 1-D model. This is so because in the 2-D model, the density-of-state function is using a parabolic function instead of step function in QW case. Thus the carrier density in the QW is underestimated. In the future work, this problem can be solved by incorporation of a step function in the density-of-states. The current density distribution of the 10 μm stripe device at 3.2 V bias is shown in Figure 4-12. The lateral carrier distribution along a cut line placed in the center of QW is plotted in Figure 4-13, under the bias voltages both below (2.9 V) and above (3.2 V) threshold. The line width broadening factor α is chosen to be equal to 4 in the above calculations. As a consequence of the finite α in eqn. (4.2), the dip in the lateral carrier distribution observed above threshold (3.2 V) causes an the increase of the refractive index in this region, which leads to the so-called self-focusing effect. In the region under the strip, the electron and hole concentrations are relatively close, while in the region away from the strip edge, the hole concentration drops to much smaller values than the electron concentration. This is due to the relatively smaller lateral spreading of the hole current as compared to the electron current.

The above procedure is repeated for devices with different stripe widths,

providing the L-I curves as shown in Figure 4-14. The threshold current vs. stripe width relation of the 1 mm long device A/C is thus obtained as plotted in Figure 4-15. Figure 4-15 shows that the threshold current vs. stripe width behavior of strained CdZnSe/ZnSSe/ZnMgSSe SCH QW lasers is more like the behavior observed in unstrained GaAs/AlGaAs QW lasers, unlike the strained-layer InGaAs/GaAs QW lasers. This is due to the fact that although the strain effect in CdZnSe can increase the heavy hole mobility in the lateral direction, the value is still quite low compared with the hole mobility in InGaAs. The effect of the low hole mobility in CdZnSe is two fold: first it reduces lateral current spreading; second, it induces a stronger self-focusing effect which works towards reducing the anti-guiding effect. The self-focusing effect is especially significant in devices with large W, as shown in Figure 4-16 in a device with W = 50 μm. The fundamental lateral mode is maintained even with such large stripe width due to the self-focusing effect. This is consistent with the experimental results.[10,47]

4.5 Summary

In this chapter, the optical field guiding model and the local optical gain model have been introduced and evaluated in combination with the 2-D electrical model. The simulation and optimization of the gain-guided stripe-geometry ZnCdSe/MgZnSSe SCH SQW diode laser has been performed. Starting from vertical transverse 1-D simulation, the gain/spontaneous emission spectra and injected carrier density relations of such devices were obtained from which a phenomenological gain model as well as radiative (spontaneous-emission) coefficient were established. This phenomenological gain and spontaneous-emission coefficient are then combined with a comprehensive double hetero-structure (DH) laser simulator (SILVACO LASER),[6] which is based on solving the coupled Poisson and Helmholtz equations, to perform a full two-dimensional simulation that includes above-threshold modeling. V-I, G-I and L-I curves of such device have been

obtained. For low threshold current (density) operation, the transverse device parameters are obtained first by the 1-D model and then the lateral related parameter (stripe width) is calculated by the 2-D model. The calculated results on stripe width dependence of lateral optical mode size are consistent with the published experimental observations. Finally, the interrelationships of the different models used in chapter 3 and 4 are summarised as illustrated below.

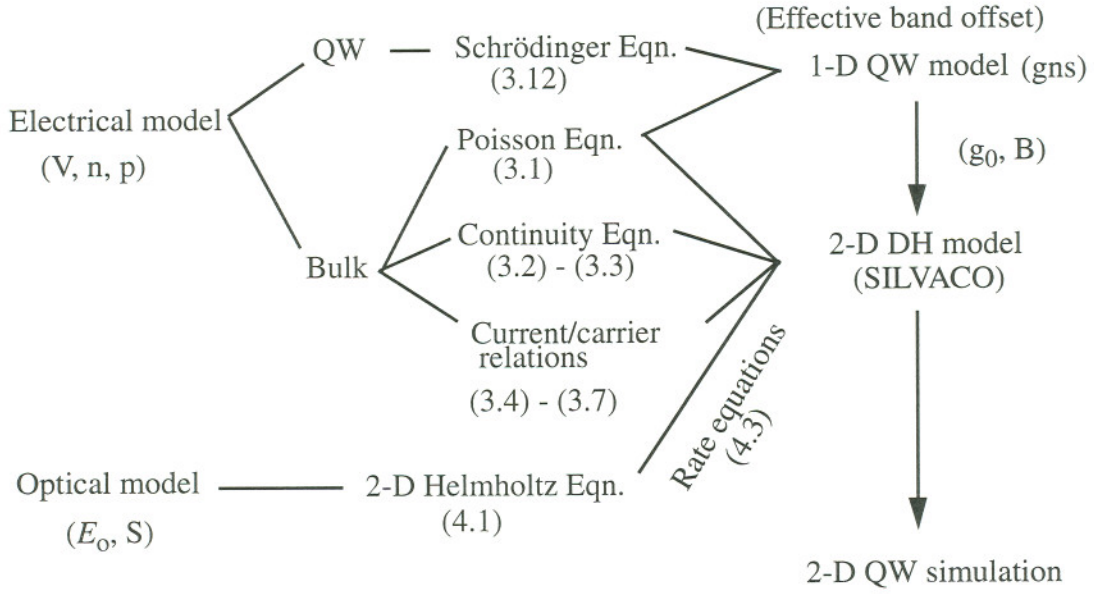

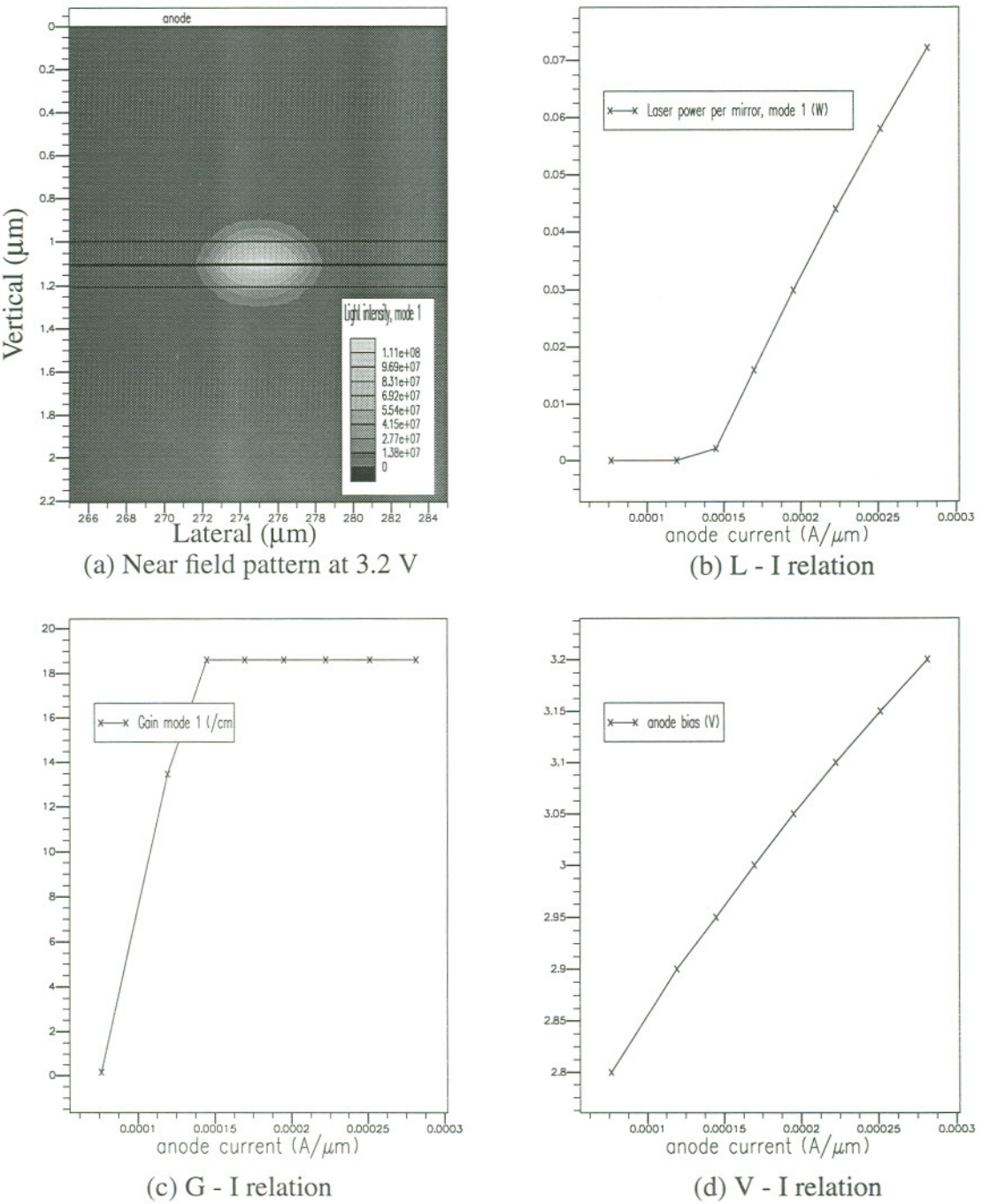

(a) Near field pattern at 3.2 V

(b) L - I relation

(c) G - I relation

(d) V - I relation

Figure 4-11: 2-D simulation results of gain guided 10 μm stripe QW laser
Current is normalized to the longitudinal dimension (cavity length L=1mm).

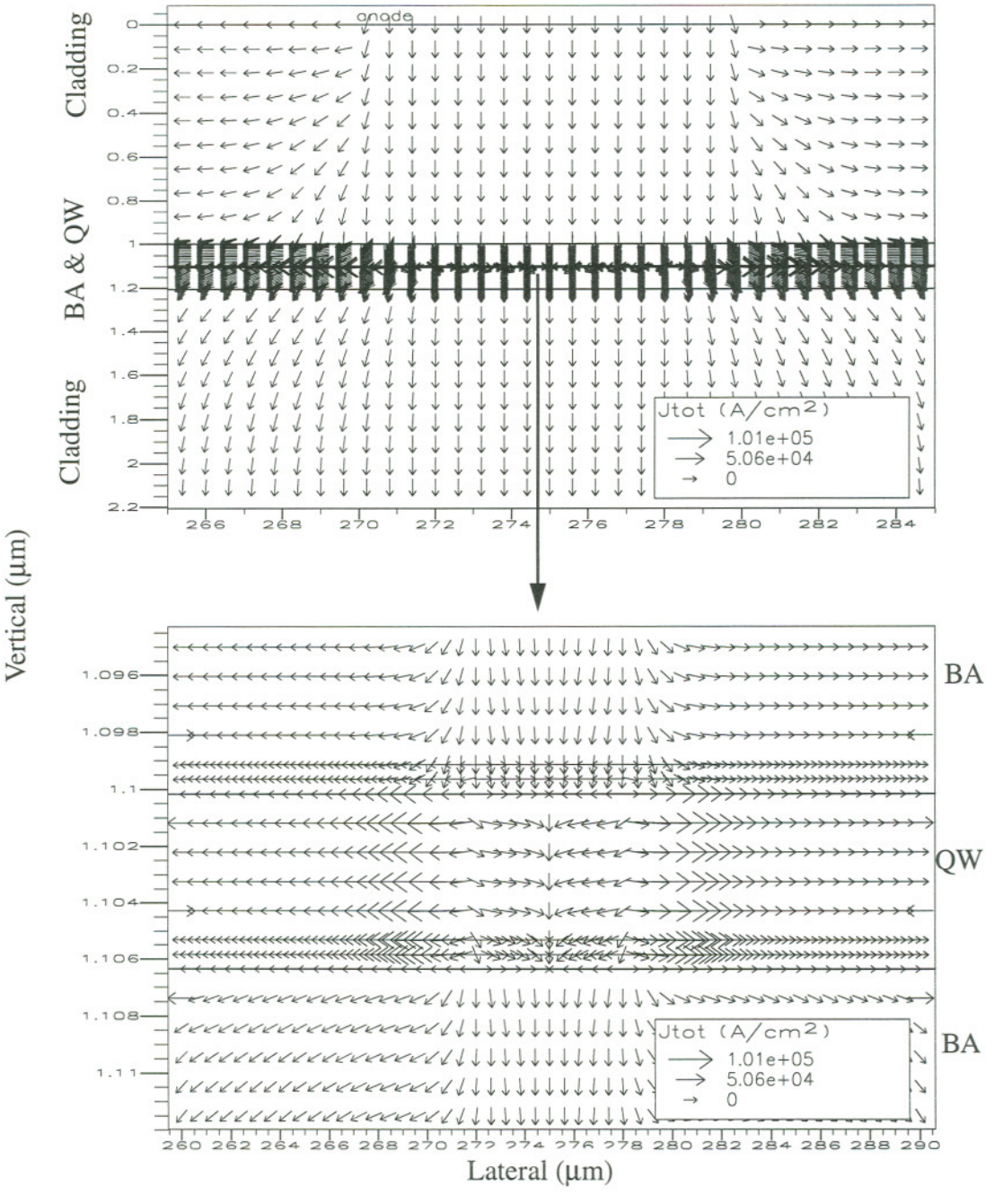

Figure 4-12: 2-D current density distribution of gain guided 10 μm stripe QW laser.

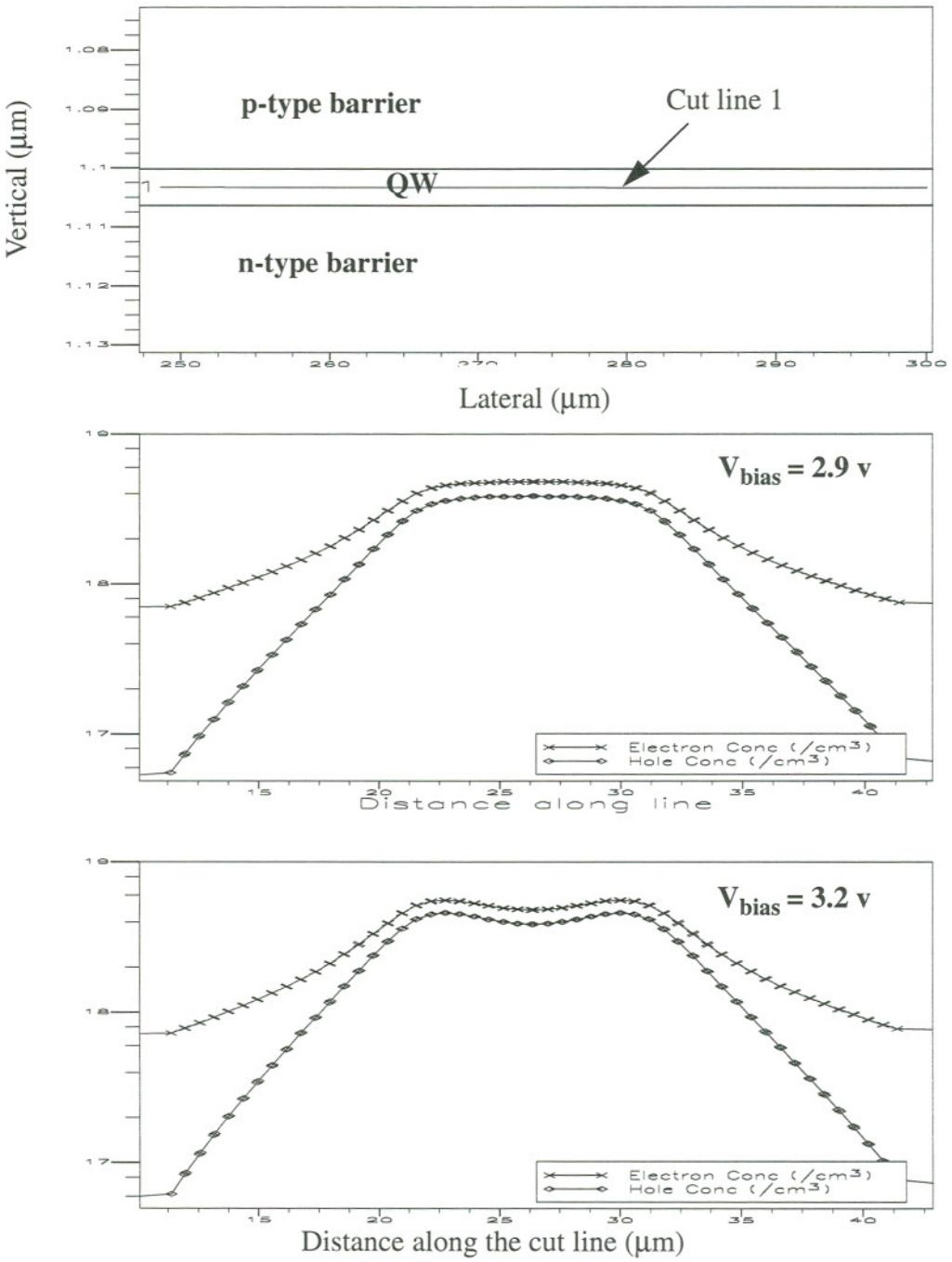

Figure 4-13: Lateral carrier density distribution of gain guided 10 μm stripe QW laser.

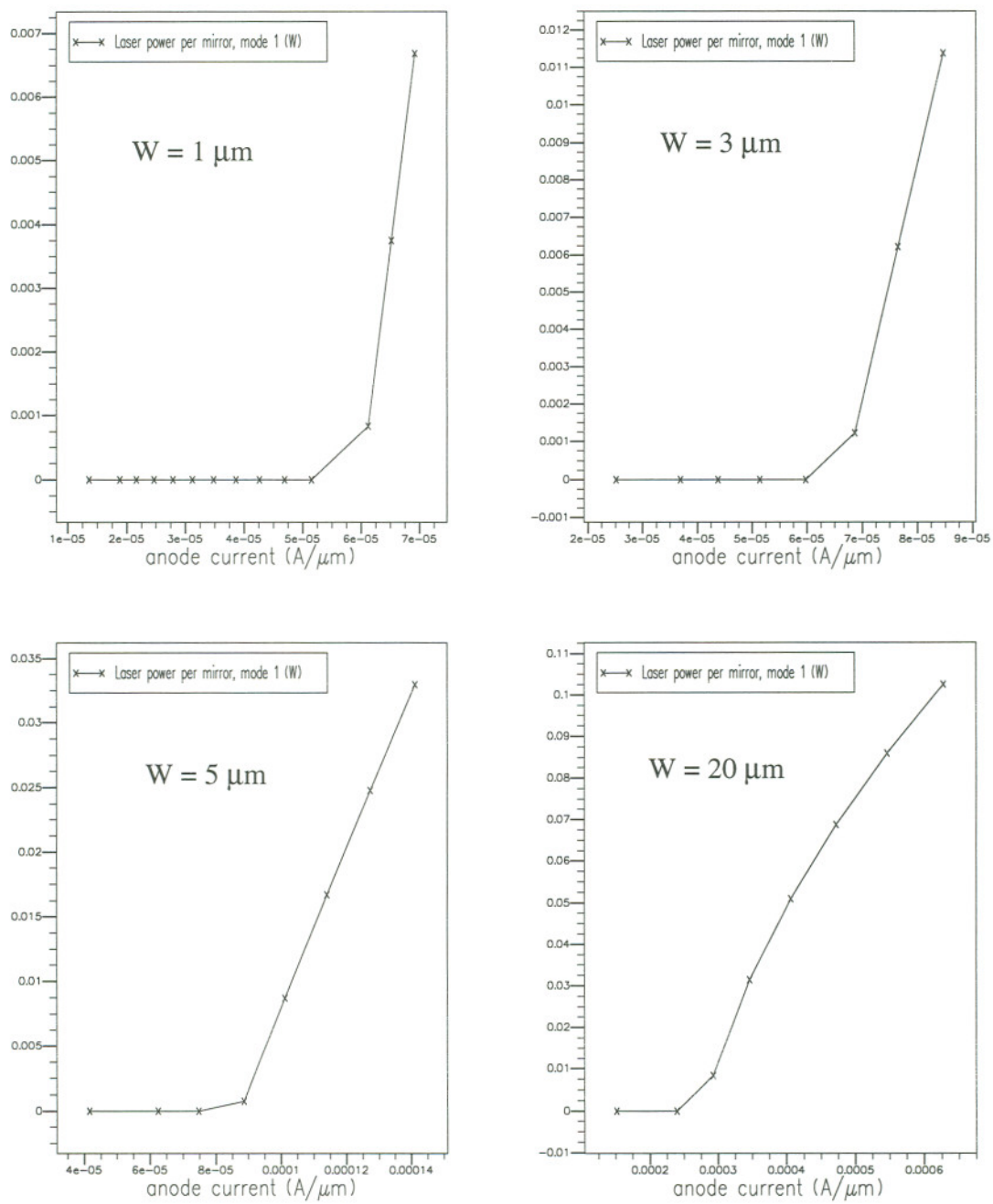

Figure 4-14: Comparison of the L-I curves of the devices with different strip width W (See figure 4-11 (b) for W=10 μm).

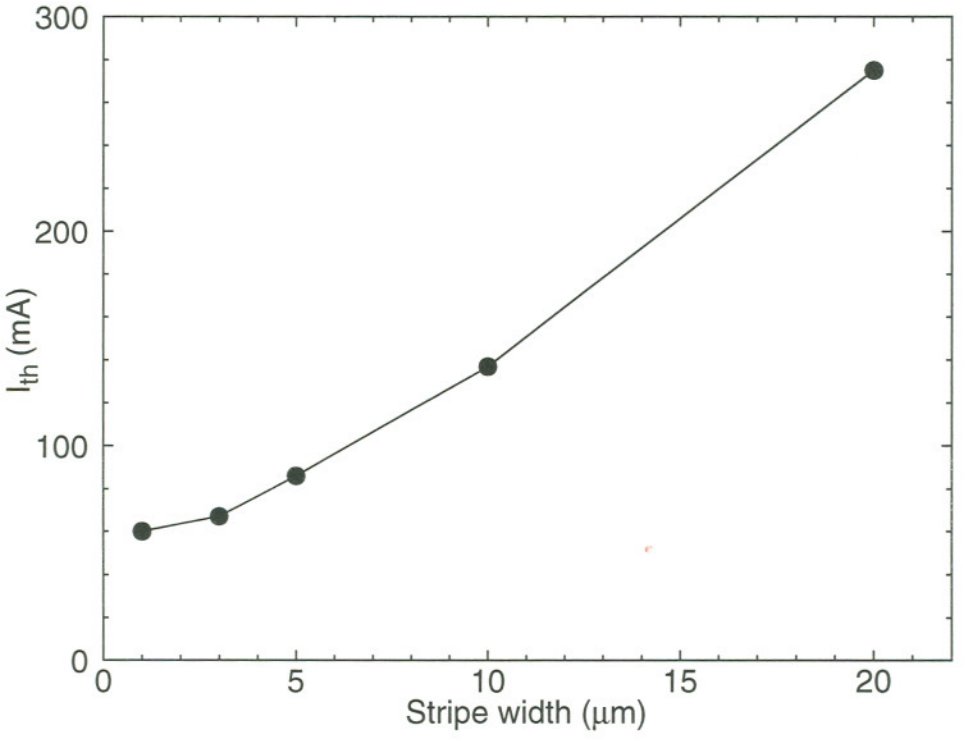

Figure 4-15: Threshold current vs. stripe width W.

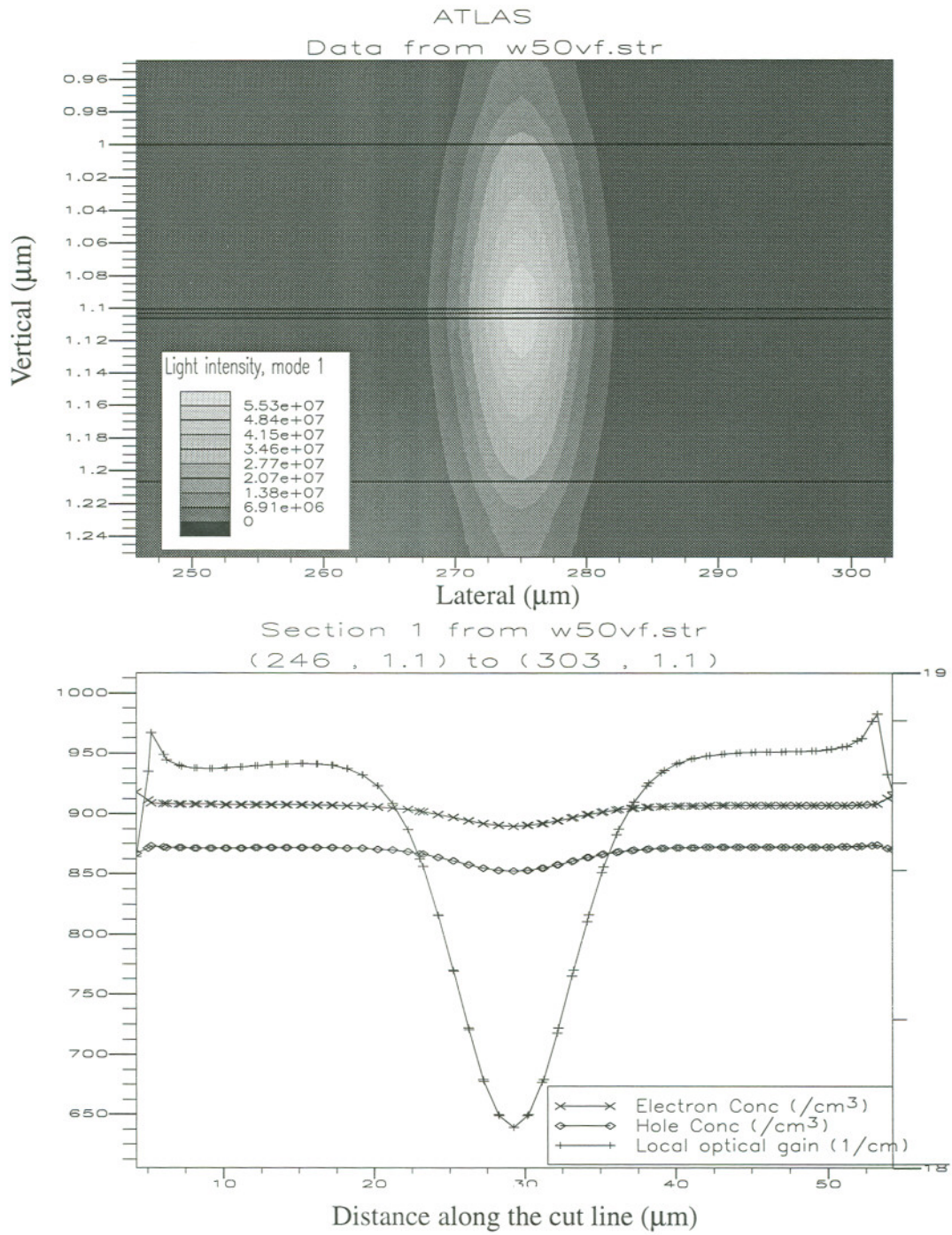

Figure 4-16: Near field pattern and lateral carrier/gain distribution of device with 50 μm stripe at 3.2 V.

Chapter 5 NOVEL II-VI HETEROSTRUCTURE DEVICES

5.1 Introduction

The rapid development in ZnSe based material technology also stimulated the investigation on hetero-structures based on other material systems. In this chapter, we will discuss two novel heterostructure devices which take advantage of the recent and potential future improvement of the technology. The first device is a laser diode based on MgZnTeSe which is using an alternative approach for improving of p-type conductivity. The second device is related to the electronic application of wide band gap semiconductors for HBT emitters. In this device, a ZnS emitter is analyzed in a Si bipolar transistor configuration. The advantages, as well as detailed device structures of these proposed device will be discussed.

5.2 Novel blue green laser diode based on MgZnSeTe

ZnSe is known to have residual n-type conductivity. Although a breakthrough in p-type doping was achieved by applying the nitrogen radical doping technique in molecular beam epitaxy (MBE),[9] the doping levels remain moderate (at most 10^{18} cm^{-3}) with a relatively deep acceptor level (> 100 meV).[12] This leads to difficulties in forming ohmic contacts and results in high electrostatic fields necessary in the p-layer for ionizing the acceptors, (as discussed in chapter 3) which makes a reliable practical device operating CW at room temperature still unavailable. It is known that ZnTe is the only binary of the wide band-gap II-VI semiconductors which can be highly doped with p-type impurities

($> 10^{19}$ cm^{-3})[50]. In fact, ZnTe has been introduced in a ZnTe/ZnSe graded superlattice as a quasi-Ohmic contact layer to p-type ZnSe[49]. Also, low-resistance Ohmic contacts for p-type ZnTe were obtained recently[51]. It was already established in the 1960's that the alloy $ZnSe_{1-y}Te_y$, as prepared by a vapor phase growth technique, could be doped both p- and n-type (bi-polar conductivity property) in the composition range of $0.5 < y < 0.6$ using impurity diffusion[52]. But a double-hetero (DH) structure for both electron and hole confinement can not be realized in such a system, due to the relatively small band gap energy difference and the type II alignment of the ZnTe/ZnSe hetero-junction. Additionally, of course, lattice matching is not possible in such a hetero-structure. Incorporation of the IIa element Mg into the ZnSeTe system would open up the available band gap range for DH structure design, which has been demonstrated in the MgZnSSe system. Compared with MgS and MgSe, MgTe has less ionicity in the bonding. The ionicity is only 19% for MgTe compared with 30% for MgSe and 35% for MgS, as estimated from the difference of electronegativity shown in Fig. 2-1. Thus, MgTe can be more easily formed in the zinc-blende (ZB) structure[53]. Adding Mg does not change the doping property very much[54]. Thus, by engineering the new material MgZnSeTe, a DH laser can be obtained with improvements in carrier confinement, high p-type doping and low Ohmic contact resistance, as proposed previously by Cai and Engelmann[55] and more recently by Chadi[56]. Here, we first describe a separate-confinement-hetero (SCH) single quantum well (SQW) laser structure using the early work of M. Aven[52]as a guide, then introduce a modified configuration reflecting the recent developments in experimental work.[57]

The lattice constant of ZB binaries can be calculated from the tetrahedral covalent radii, which we found quite consistent with available experimental data, as discussed in section 2.3.1. Thus this method was used to obtain the lattice constant of ZB MgTe. The band gap of MgTe is estimated at about 3.3 eV for the ZB structure at room temperature based on Ref. [54]. The bowing parameter b and band gap of ternary and quaternary of

MgZnSeTe are then determined by following the procedure described in section 2.3.1.

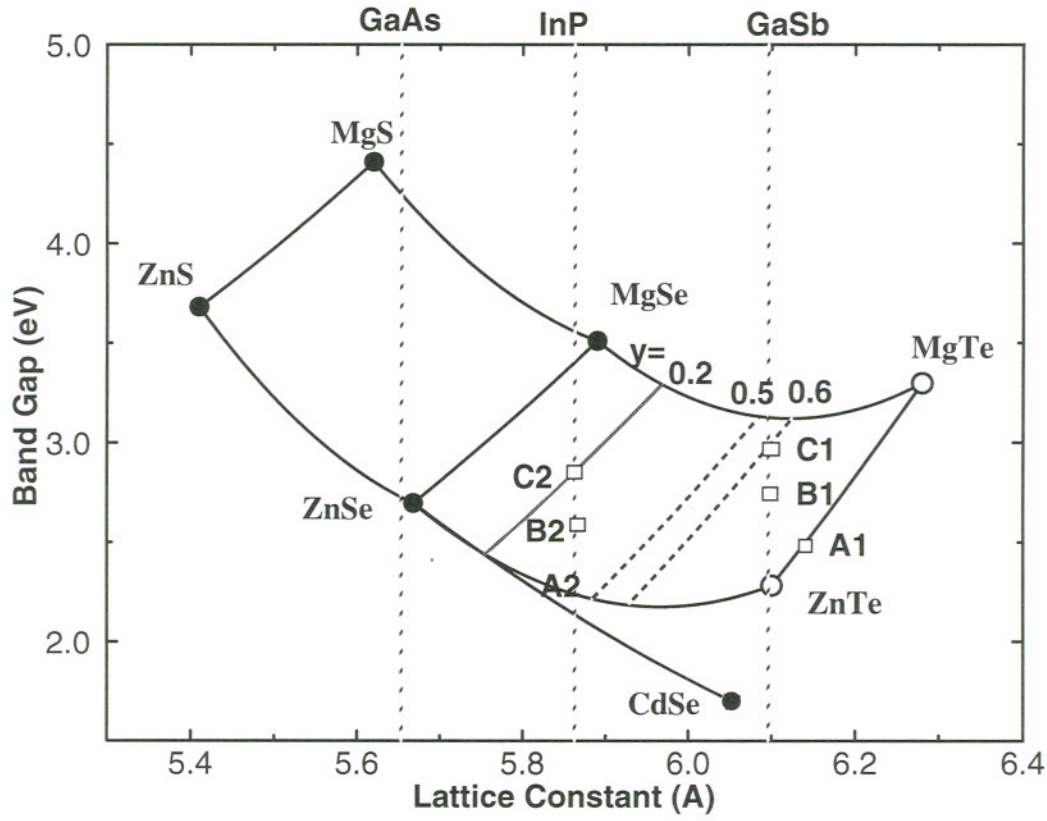

Figure 5-1: Band gap *vs.* lattice constant of the relevant zinc blende II-VI compounds at room temperature. In the above figure, the region in between the two dotted lines connecting the ZnSeTe and MgSeTe band gap valleys represents the composition where the bi-polar conductivity is expected. C1: cladding ($Mg_{0.85}Zn_{0.15}Se_{0.4}Te_{0.6}$), B1: barrier ($Mg_{0.6}Zn_{0.4}Se_{0.3}Te_{0.7}$) and A1: QW ($Mg_xZn_{1-x}Te$, x = 0 - 0.2) for SCHI. C2 and B2 are the cladding and barrier for SCH-II.

Notice that $MgSe_{1-y}Te_y$ has a similar bowing characteristic as $ZnSe_{1-y}Te_y$. Also, the doping property of $Mg_xZn_{1-x}Te$ is very similar to that of ZnTe for x as high as 0.75 [54]. Hence, we expect that the engineered zinc-blende $Mg_{1-x}Zn_xSe_{1-y}Te_y$ quaternaries between the dotted lines in Fig. 2-1 ($0.5 < y < 0.6$), have a similar bi-polar conductivity property as their ternary counterpart $ZnSe_{1-y}Te_y$ ($0.5 < y < 0.6$). Thus, by choosing $Mg_{1-x}Zn_xSe_{1-y}Te_y$ cladding layers with y in the range of 0.5 - 0.6 the preparation of a pn diode structure should be feasible. For blue-green light emission, the band gap of the cladding should be close to 3 eV. Hence, $Mg_{0.85}Zn_{0.15}Se_{0.4}Te_{0.6}$ is chosen as cladding layer material (C1 in Fig.5-1), which is lattice matched to GaSb, a commercially available substrate. For the barrier and active layers, doping is of minor concern, but the band offset is the most important issue. Based on the general band alignment picture and Ref. [30], it is the advantage of the MgZnSeTe system that the Se/Te ratio can be adjusted to provide a reduced valence band offset, thus overcoming the type II alignment problem of the ZnSe/ZnTe system, as shown in Fig. 5-2. The barrier can be easily chosen to be lattice matched with the cladding, as B1 ($Mg_{0.6}Zn_{0.4}Se_{0.3}Te_{0.7}$, Eg=2.8 eV) in Fig.5-1. The simple binary ZnTe could be the choice for an unstrained QW, emitting in the green (538 nm). To obtain blue emission, preferably a compressively strained QW such as A1 in Fig. 2-1 ($Mg_xZn_{1-x}Te$) could be incorporated. With a Mg composition x of about 0.2, emission at a wavelength of about 490 nm can be achieved. Figure 5-2 demonstrates the pronounced hole-barrier lowering for ZnTe with respect to the MgZnSeTe alloys as compared with ZnSe, which is favorable for Ohmic contact formation to the p-type cladding layer. A ZnTe top layer can be used for both Ohmic contact formation and shielding the hygroscopic MgZnSeTe cladding layer against exposure to air. In order to reduce the barrier for electrons between the n-type MgZnSSe cladding and GaSb substrate, a graded AlGa(As)Sb layer can be incorporated. The complete proposed device structure is shown in Fig.5-3.

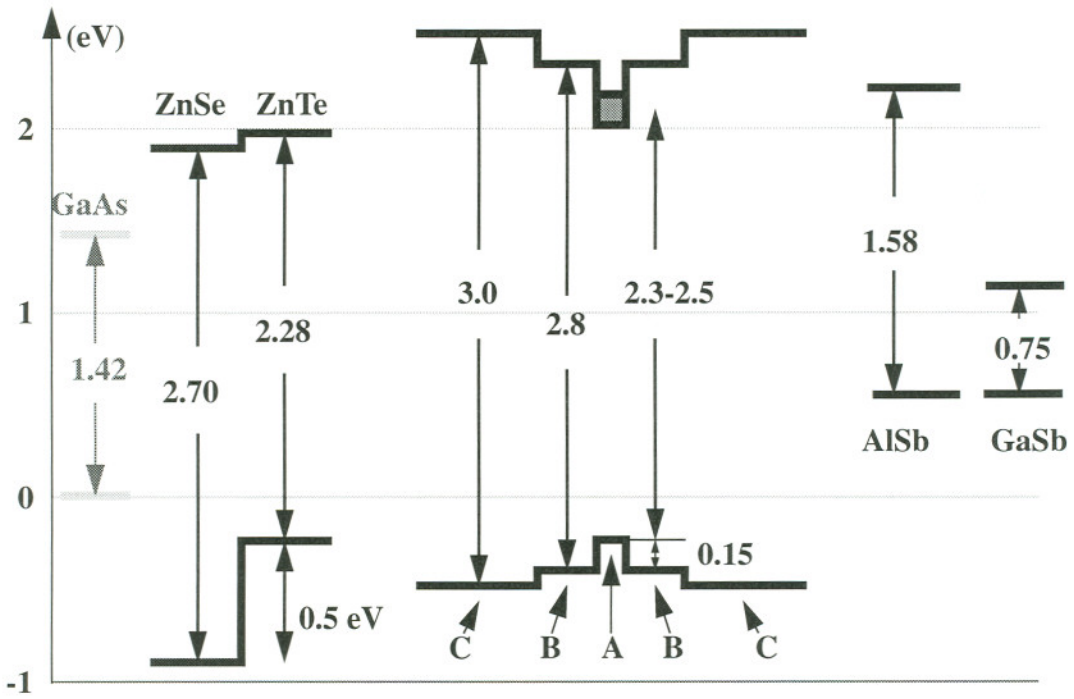

A: $Mg_xZn_{1-x}Te$ (x=0-0.2) B: $Mg_{0.6}Zn_{0.4}Se_{0.3}Te_{0.7}$ C: $Mg_{0.8}Zn_{0.2}Se_{0.4}Te_{0.6}$

Figure 5-2: Band alignment of SCH-I using GaAs as the energy reference;
Improved carrier confinement of the MgZnSeTe/(Mg)ZnTe system as compared with the ZnSe/ZnTe system is demonstrated. Also note the lower electron barrier in the MgZnSeTe/AlSb heterojunction than in the MgZnSeTe/GaSb heterojunction.

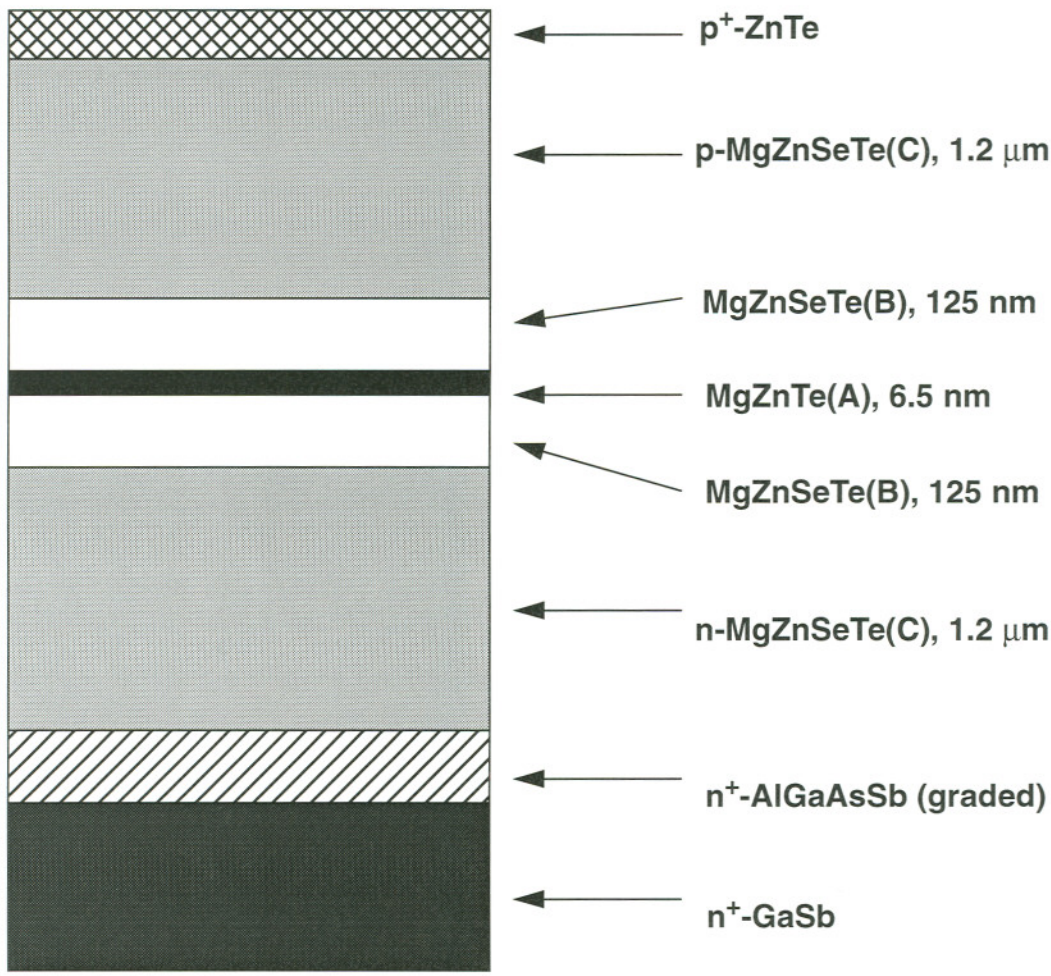

Figure 5-3: Schematic structure of proposed MgZnSeTe SCH SQW laser SCH-I with AlGa(As)Sb graded transition layer and ZnTe cap layer, grown on GaSb substrate.

Recently, W. Faschinger et al. [57] have investigated the doping behavior of ZnSe/ ZnTe short period superlattices grown by MBE. They showed that averaged Te content has a strong positive effect on p-type doping and negative effect on n-type (by Cl) doping. At average Te concentrations above 20% the measured electron concentrations are below 10^{16} cm^{-3}. With such a technology, a second SCH structure can be designed which is lattice-matched to an InP substrate, for which the cladding and barrier are also shown in Fig.2.1, as C2 and B2 respectively. A ZnSeTe QW layer A2 can be chosen in this case either compressively or tensively strained. The band alignment techniques combined with the graded AlGa(As)Sb layer described above can be also applied in this case.

5.3 ZnS/Si heterojunction bipolar transistor (HBT)

Many material systems are currently under study for use in HBT devices. The most extensively studied is the AlGaAs/GaAs system. Because the silicon based devices will continue to dominate the electronic industry, many efforts also have been put into a Si based HBT. The SiGe HBT, in which a low band gap material SiGe alloy has been used as base, has been demonstrated to have high speed performance.[58] Wide gap emitters for Si such as GaP and SiC, have been reported before.[59, 60] ZnS, which has a lattice constant of 5.410 Å, (very close to that of Si which is 5.43 Å, mismatch is only about 0.3%), and a very wide band gap of 3.66 eV, should also be a very attractive material to be used as an emitter. Exact lattice matching can be realized by incorporation of small amount of Cd or Se to form the ternaries CdZnS or ZnSSe. Epitaxial layers of ZnS have been grown on Si substrates in a variety of growth methods, including sputtering, evaporation, MBE, MOCVD and ALE[8, 62]. The heterojunction of ZnS/Si has also been investigated in solar cell studies.[61] Recently, through the rapid development of the ZnSSe based blue-green diode laser technology, epitaxial growth and doping of ZnSe and ZnS based alloys have

been extensively studied. An Ohmic contact to n-type ZnSSe is also readily available with In or Au. Thus, a semiconductor device based on the ZnS/Si heterostructure system becomes a realistic possibility.

The major material properties of ZB ZnS is listed in table 5-1 along with those of Si..

Table 5-1: Comparison of material properties of ZnS and Si

	ZnS	Si
Band gap E_g	3.66 eV	1.1 eV
Lattice constant a	5.410 Å	5.431 Å
Electron affinity	3.9 eV	4.1 eV
Effective mass m_n/m_o	0.18-0.34	0.19
Effective mass m_{hh}/m_o	1.76	0.54,
Effective mass m_{lh}/m_o	0.23	0.15
Donor level	0.014 eV (Iodine)	0.039 eV (Sb)
Donor level	0.11 eV (Cl)	0.049 eV (P)
Donor level	0.18 eV (Al)	0.049 eV (As)
Ohmic contact	Au, In	Al

The band gap of ZnS is 3.66 eV, much large than that of Si, which is only 1.12 eV. This large band gap difference (more than 2.5 eV) leads to several very interesting device applications. The exact band alignment is still uncertain at this time. Fig 2.4 gives three possible band alignments of the ZnS/Si heterojunction. If the conduction band offset remains relatively small, as estimated by the affinity rule at ~0.1 eV, a Si based npn type

heterostructure bipolar transistor (HBT) with ZnS (or its alloy) as an emitter can be fabricated. The simulation of such a device can be done on the numerical model developed in chapter 3. The results show that the a DC common emitter current gain β of 100-1000 and a current gain cut-off frequency f_T of 50-175 GHz can be obtained with an uniformly doped still un-optimized structure. An example of the simulation results is shown in Figure 5-5. If, on the other hand, the conduction band offset is relative large, as estimated from the Harrison-Tersorff model [30] at ~0.4 eV, a hot electron HBT which would operate at higher speed may be fabricated. If the conduction band offset is so large that it is greater the band gap of Si, as reported by Maierhofer et al. [62], then a so called Auger transistor with a current gain larger than one can possibly result. The simulation of the device operation in these situations will be performed in the future.

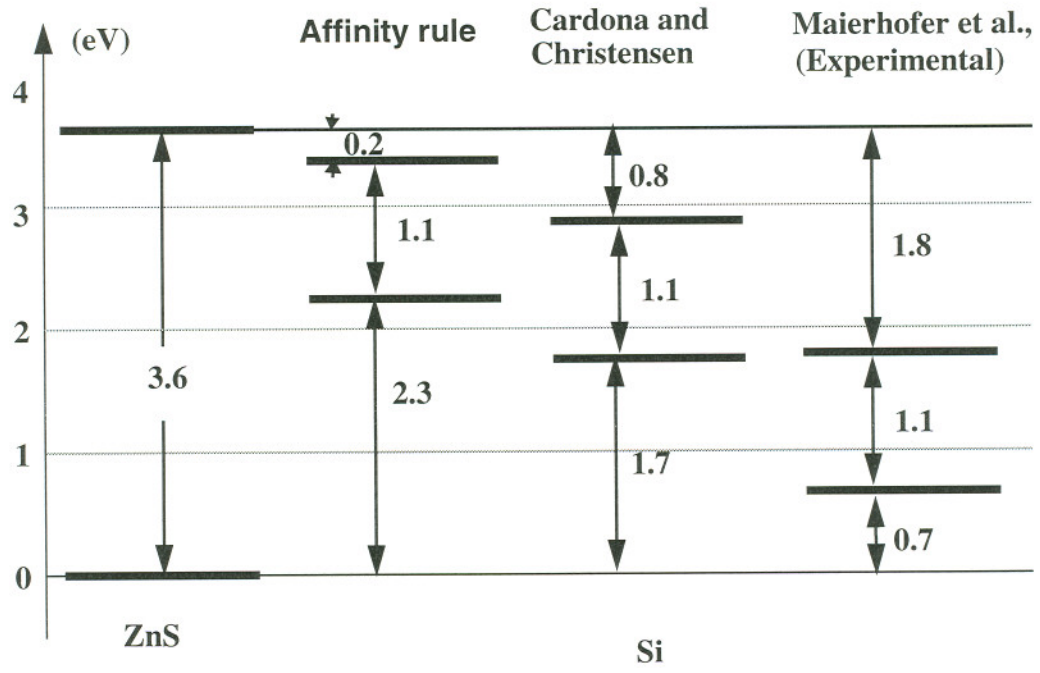

Figure 5-4: Possible band offset of ZnS/Si hetero-junction.

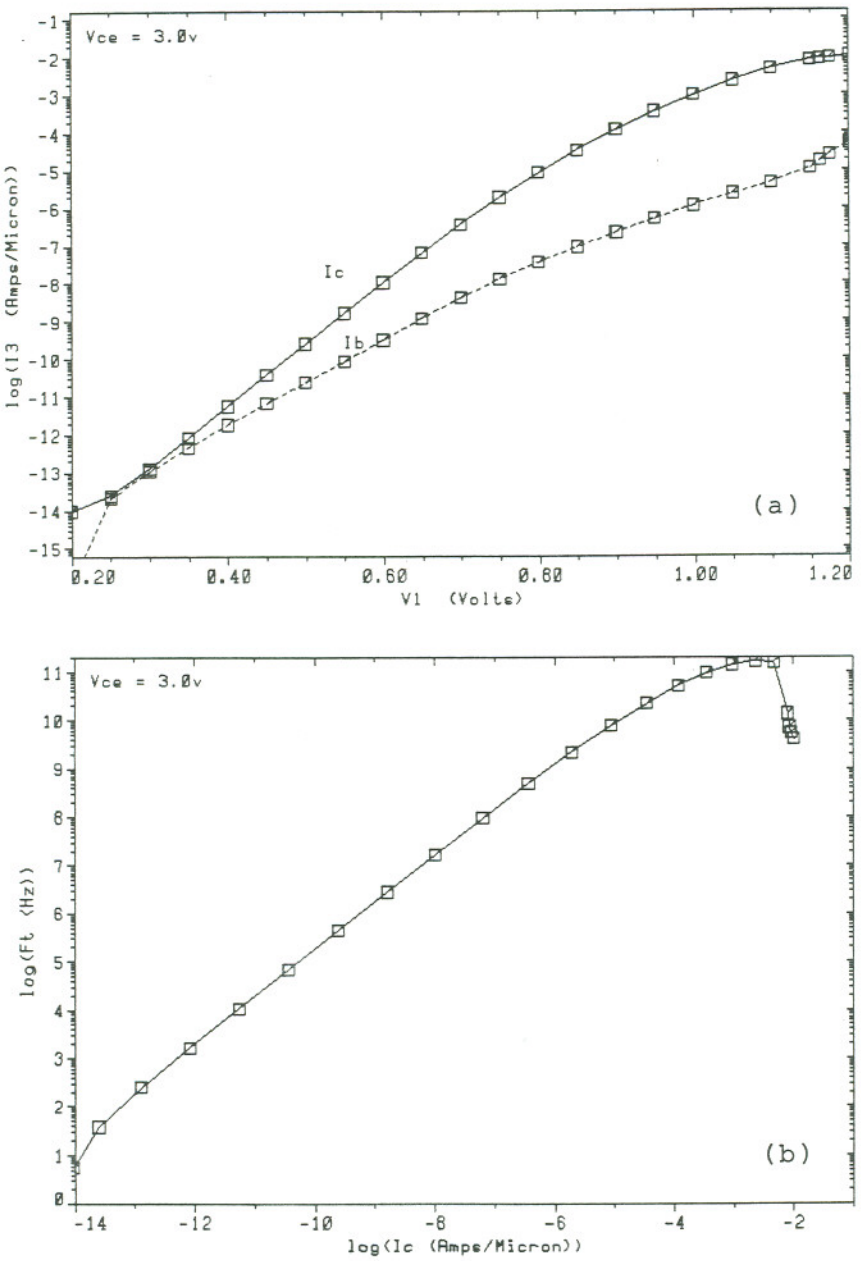

Figure 5-5: Simulation results of ZnS/Si HBT assuming a small conduction band offset. (a) I_c & I_b vs. V_{be}. (b) f_T vs. I_c.

5.4 Summary

In conclusion, we have presented the design of novel diode laser structures based on the MgZnSeTe quaternary alloy system. The basic idea is to take advantage of the possibility of bi-polar doping in ZnSeTe and add Mg to increase the band gap energy to get good carrier confinement. Also an AlGaAsSb layer can be employed for reducing the possible difficulties in electron transport. SCH SQW structures can be prepared with improvements expected in diode laser performance for blue-green light emission.

A novel heterojunction transistor based on ZnS/Si has also been discussed. The extremely large band gap difference between ZnS emitter and Si based may lead to some interesting effects depending on the actual band alignment, which is currently not well established yet.

Chapter 6 CONCLUSIONS AND SUGGESTIONS FOR FUTURE WORK

Just like the device fabrication technology, the device simulation and modeling of II-VI semiconductor devices is far from mature compared with Si and GaAs technology. Most of the work presented in this dissertation is initiative in nature, follow-up work is necessary in the future.

The atomic bonding of the compounds was chosen as a fundamental concept for material property study. Based on the covalent bond parameters, the lattice constant and energy band bowing parameter were obtained; in addition, impurity solubility limitation were explained; and strain effect and elastic module relations between WZ and ZB structure were evaluated.

The design and simulation of II-VI semiconductor devices are benefited from the above mentioned material property study, which lead to more accurate modeling of the CdZnSe/ZnMgSSe based QW laser diode, as well as generated the idea of a novel ZnMgSeTe laser diode and a ZnS/Si heterojunction bipolar transistor. The accurate modeling of QW lasers involves the coupling of three types of fundamental equations: the Schrödinger and Poison equations for electrons/holes, and Helmholtz equation for the optical field. To simplify the numerical solution procedure, the model is split into two parts. The first part is used for the QW region, where the quantum confinement is important and the optical field change can be neglected. Thus, the model is constructed from the coupled Schrödinger and Poison equations in a 1-D domain. For further simplification, the solution of the Poisson equation in this case resulted in a phenomenological method of proper adjustment of the band offset at large enough injection. This method is called effective band offset approach. Based on this approach, with a separate calculation of optical

confinement factor and threshold condition, the gain and threshold radiative current density relation was obtained. The results are matched quite well with available experimental data. Additionally, the optimized vertical structure parameters for low-threshold operation of a CdZnSe/ZnMgSSe based SCH QW laser diode were obtained. The second part of the model is for the bulk regions including cladding and barrier where quantum effects can be neglected. The optical field change becomes significant in these regions, thus the model consists of Poisson and Helmholtz equations but now in a 2-D domain. The QW influence on gain and spontaneous recombination is incorporated by phenomenological parameters obtained from the first part of the model. Thus, a complete electrical and optical simulation of QW lasers has been achieved. Major trends of lateral structure parameters such as stripe-width influence on device performance were elucidated in this approach.

In the follow-up work, the 1-D model need to be improved in the following aspects. For the band filling process other conduction band valley (e.g. X, L..) need to be incorporated in future study along with a more accurate band structure calculation. A more comprehensive intra-band scattering model needs to be considered for gain modeling. The interface characteristics of II-VI heterojuntions need to be further evaluated.

The current 2-D model is still quite approximatic in some respect. As a first step for a more accurate model for the QW laser, the step like density-of-states function need to be used instead of parabolic one. Further, a full-physical model can be developed based on a more advanced numerical approach, thus the complete spectral behavior with multiple longitudinal modes can be included in the calculation. From the electrical modeling of the II-VI QW laser, one can see that space-charge induced high electrical field were observed locally near the QW region in barrier layer, this may lead to some high-field effect such as field ionization of impurities (Frankel-Poole effect) and impact ionization. The inclusion of these effects in the activation of carrier is necessary in the future work. The evaluation of such effects on device degradation will be another important issue. Hot electron effects

need to be evaluated in the ZnS/Si heterojunction bipolar transistor modeling in the case where a large conduction band offset exists.

Related experimental work is also important. The model needs to be adjusted with results from laser diode processing and characterization lab work. The novel devices proposed in this thesis need to be demonstrated in fabrication. Other wide-band-gap materials such as used in GaN based devices will be another suitable area for applying the model developed in this thesis.

References

1. R. A. Reynolds, "The II-VI compounds: 30 years of history and the potential for the next 30 years", *J. Vac Sci. Technol.* ***A*****, 7 (2)** 269, (1989).

2. B. Ray, *II-VI compounds*, Pergamon Press, Oxford, UK, (1969).

3. R. N. Bhargava, "Compact blue lasers in the near future", *J. Cryst. Growth,* **117**, 894, (1992).

4. R. Bhargava, "Blue and UV light emitting diodes and lasers", *Optoelectronics-Devices and Technologies*, **7 (1)**, 19-47, (1992).

5. H. Cheng, J. DePuydt, J. Potts and M. Haase, "Growth of p- and n-type ZnSe by molucular beam epitaxy", *J. Cryst. Growth*, **95**, 512-516, (1989).

6. User's Manual, *ATLAS 2D Device simulation framework*, SILVAC International, Santa Clara, CA, (1995).

7. T. Yao, Y. Makita and S. Maekawa, "Molecular beam epitaxy of $ZnSe_xTe_{1-x}$ ($0 < x < 1$)", *J. Cryst.Growth,* **45**, 309, (1978).

8. S. Iida, T. Yatabe and H. Kinto, "P-type conduction in ZnS grown by vapor phase epitaxy", *Jpn. J. Appl. Phys.*, **28 (4)**, L535-L537, (1989).

9. R. M. Park, M. B. Troffer, and C. M. Rouleau, "P-type ZnSe by nitrogen atom beam doping during molecular beam epitaxial growth", *App. Phys. Lett.,* **57 (20)**, 127, (1990).

10. M. A. Haase, J. Qiu, J. M. DePuydt, and H. Cheng, "Blue-green laser diodes", *Appl. Phys. Lett.,* **59**, 1272-1274, (1991).

11. D. B. Laks, C. G. Van de Walle, G. F. Neumark, and S. T. Pantelides, "Acceptor doping in ZnSe versus ZnTe", *App. Phys. Lett.,* **63 (10)**, 1375, (1993).

12. Y. Fan, J. Han, L. He, R. Gunshor, M. Frandt, J. Walker, N. Johnson, and A. Nurmikko , "Obervations on the limits to p-type doping in ZnSe", *App. Phys. Lett.,* **65 (8)**, 1001, (1994).

13. S. Nakamura, M. Senoh and T. Mukai, "Highly P-typed Mg-doped GaN Films Grown with GaN Buffer layers", *Jpn. J. Appl. Phys.*, **30 (10A)**, L1708-1711, (1991).

14. N. F. Mott and W. D. Twose, "The theory of impurity conduction", *Philos. Mag. Suppl.* **10**, 107, (1961).

15. R. H. Bube, *Photoconductivity of Solids*, John Wiley & Sons, Inc., New York, (1960).

16. B. Pauling, *The nature of Chemical Bond*, Cornell University Press, New York, (1960).

17. J. C. Phillips, *Bonds and Bands in Semiconductors*, Academic Press, New York, (1973).

18. Satya N. Sahu, *Defect Studies in Semiconductors*, Ph.D dissertation, SUNY at Albany, (1982).

19. J. Bernard and A. Zunger, "Optical bowing in zinc chalcogenide semiconductor alloys", *Phys. Rev. B*, **34 (8)**, 5992-5995, (1986).

20. R. Hill, "Energy-gap variation in semiconductor alloys", *J. Phys. C: Solid State Phys.*, **7**, 521-526, (1974).

21. J. Matthews and A. Blakeslee, "Defects in epitaxial multilayers", *J. Cryst.Growth*, **27**, 118-125, (1974).

22. P. Parbrook, B. Henderson, K. O'Donnell, "Critical thickness of common-anion II-VI strained layer superlattices (SLSs)", *J. Cryst. Growth*, **117**, 492-496, (1992).

23. T. Chong and C. Fonstad, "Theoretical gain of strained-layer semiconductor lasers in the large strain regime", *IEEE J. of Quantum Electron.*, **25 (2)**, (1989).

24. P. Lawaetz, "Valence-band parameters in cubic semiconductors", *Phys. Rev. B,* **4 (10)**, 3460-3467, (1971).

25. R. M. Martin, "Relation between elastic tensors of Wurtzite and Zinc-Blende struc-

ture materials", *Phys. Rev. B*, **6 (12)**, 4546, (1972).

26. J. Menendez and A. Pinczuk, "Light scattering determinations of band offsets in semiconductor heterosturctures", *IEEE J. Quantum Electron.*, **24 (8)**, 1698, (1988).

27. E. Yu, J. McCaldin and T. McGill, in: *Solid State Physics* **46**, Academic Press, Inc., San Diego, 12-26, (1992).

28. W. A. Harrsion, "Theory of band line-ups", *J. Vac. Sci. Technol. B,* **3 (4)**, 1231, (1985).

29. J. Tersoff, "Theory of semiconductor heterojunctions: The role of quantum dipoles", *Phys. Rev. B*, **30** (8), 4874, (1984).

30. W. A. Harrsion and J. Tersoff, "Tight-binding theory of heterojunction band lineups and interface dipoles", *J. Vac. Sci. Technol. B*, **4 (4)**, 1068, (1986).

31. C. Van de Walle, "Band lineups and deformation potentials in the model-solid theory", *Phys. Rev. B,* **39 (3)**, (1989).

32. H. C. Casey and M. B. Panish, *Heterosturcture Lasers*, Academic Press, New York, (1968).

33. R. Yamamoto, M. Inoue, K. Itoh and T. Shitaya, "Visible electroluminesecence from p-n junctions in $Cd_{1-x}Mg_xTe$", *Jpn. J. Appl. Phys.,* **6**, 537, (1967).

34. H. Okuyama, K. Nakano, T. Miyajima, and K. Akimoto, "Epitaxial growth of ZnMgSSe on GaAs substrate by molecular beam epitaxy", *J. Cryst.Growth,* **117** 139-143, (1992).

35. T. Matsuoka, A. Ohki, T. Ohno, Y. Kawaguchi, "Comparison of GaN and ZnSe-based materials for light emitters", *J. Cryst. Growth,* **138**, 727, (1994).

36. A. H. Marshak and C. M. Van Vliet, "Electrical current and carrier density in degenerate materials with nonuniform band structure", *Proc. IEEE,* **72**, 148, (1984).

37. M. S. Lundstrom and R. J. Schuelke,"Numerical analysis of heterostructure semiconductor devices," *IEEE Trans. Electron Device*, **ED-30**, 1151, (1983).

38. S. W. Corzine, R. H. Yan and L. A. Coldren, Chapter 1, *Quantum Well Lasers*, ed. P. Zory, Academic Press, San Diego, (1993).

39. J. Barrau, B. Brousseau, M. Brousseau, R. J. Simes and L. Goldstein "Novel principle of confinement in quantum-well structures", *Electron. Lett.,* **28 (8)**, 786, (1992).

40. D. Wilt and A. Yativ, "A self-consistent static model of the double-heterostructure laser", *IEEE J. Quantum Electron.*, **QE-17 (9)**, (1981).

41. T. Ohtoshi, K. Yamaguchi, C. Nagaoka, T. Uda, Y. Murayama and N. Chinone, "A two-dimensional device simulator of semiconductor lasers", *Solid-State Electron.*, **30 (6)**, 627-638, (1987).

42. K. Kahen, "Two-dimensional simulation of laser diodes in the steady state", *IEEE J. Quantum Electron.*, **24 (4)**, (1988).

43. M. Ueno, S. Asada, and S. Kumashiro, "Two-dimensional numerical analysis of lasing characteristics for self-aligned structure semiconductor lasers", *IEEE J. Quantum Electron.*, **26 (6)**, (1990).

44. J. Ding, H. Jeon, T. Ishihara, A.V. Nurmikko, H. Luo, N Samarth and J. Furdyna, "Excitonic gain and stimulated emission in ZnSe-based quantum wells up to room temperature", *Surface Science*, **267**, 616-622, (1992).

45. P. Mensz, "Electrical and optical modeling of II-VI semiconductor diode lasers", *J. Cryst. Growth*, **138**, 697-702, (1994).

46. *User Guide, MODEIG/II*, For Info.: Gary Evans, Southern Methodist University, Dallas, Texas 75275, August, (1993).

47. J. M. Gaines, R. R. Drenten, K. W. Haberern, T. Marshall, P. Mensz, and J. Petruzzello, "Blue-green injection lasers containing pseudomorphic $Zn_{1-x}Mg_xS_ySe_{1-y}$ cladding layers and operation up to 394K", *Appl. Phys. Lett.,* **62**, 2462, (1993).

48. Y. S. Park and P. S. Zory, "Temperature dependence of the threshold current density of CdZnSe blue-green quantum well lasers", *IEEE/LEOS '93 Conference Proceedings*, 648-649, San Jose, CA, Nov. (1993).

49. Y. Fan, J. Han, L. He, J. Saraie, and R. L. Gunshor, M. Hagerott, H. Jeon, and A. V. Nurmikko, G. C. Hua and N. Otsuka, "Graded band gap ohmic contact to p-ZnSe", *Appl. Phys. Lett.*, **61**, 3160, (1992).

50. J. Han, T. Stavrinides, M. Kobayashi, and R. L. Gunshor, M. Hagerott and A.

Nurmikko, "Heavy p-doping of ZnTe by molecular beam epitaxy using a nitrogen plasma source", *Appl. Phys. Lett.*, **62 (8)**, 840, (1993).

51. M. Ozawz, F. Hiei, M. Takasu, A. Ishibashi, and K. Akimoto, "Low resistance ohmic contacts for p-type ZnTe", *Appl. Phys. Lett.,* **64**, 1120 (1994).

52. M. Aven, "Efficient visible injection electroluminescence from p-n junctions in $ZnSe_xTe_{1-x}$", *Appl. Phys. Lett.,* **7**, 146-148, (1965).

53. Chin-Yu Yeh, Z. W. Lu, S. Froyen, and A. Zunger, "Predictions and systematizations of the zinc-blende-wurtzite structural energies in binary octet compounds", *Phys. Rev. B,* **45**, 12130, (1992).

54. S. G. Parker, A. R. Renberg, J. E. Pinnell, and W. C. Holton, "Preparation and properties of $Mg_xZn_{1-x}Te$", *J. Electrochem. Soc.: Solid State Science*, **118**, 979, (1971).

55. Y. Cai and R. Engelmann, "Proposal of novel blue-green diode laser based on MgZnSeTe alloys", *IEEE/LEOS 1993 Summer Topical Meeting Digest on Visible Semiconductor Lasers*, 11, (1993).

56. D. J. Chadi, "Doping in ZnSe, ZnTe, MgSe, and MgTe wide-band-gap semiconductors", *Phys. Rev. Lett.,* **72**, 534, (1994).

57. W. Faschinger, S. Ferreira and H. Sitter, "Doping of zinc-selenide-telluride", *Appl. Phys. Lett.,* **64**, 2682, (1994).

58. G. Patton, S. Iyer, S. Delage, S. Tiwari, and J. Stork, "Silicon-germanium-base heterojunction bipolar transistors by molecular beam epitaxy", *IEEE Electron Device Lett.*, **9 (4)**, 165-167, (1988).

59. H. Kroemer, "Heterostructure bipolar transistors and integrated circuits", *Proc. of the IEEE*, **70 (1)**, (1982).

60. L. Pelaz, J. Orantes, J. Vincente, L. Bailon, and J. Barbolla, "The Poole-Frenkel effect in 6H-SiC diode characteristics", *IEEE Trans. Electron Devices*, **41 (4)**, 587-591, (1994).

61. G. Landis, J. Loferski, R. Beaulieu, P. Sekula-Moise, S. Vernon, M. Spitzer and C. Keavney, "Wide-bandgap epitaxial heterojunction windows for silicon solar cells", *IEEE Trans. Electron Devices,* **37 (2)**, 372-381, (1990).

62. Ch. Maierhofer, S. Kulkarni, M. Alonso, T. Reich, and K. Horn, "Valence band offset in ZnS layers on Si(111) grown by molecular beam epitaxy", *J. Vac. Sci. Technol. B,* **9 (4)**, 2238-2243, (1991).

63. Landolt-Börnstein, *Data in Science and Technology, Semiconductors Other than Group IV Elements and III-V Compounds*, New Series, March (1992).

64. M. Ukita, H. Okuyama, M. Ozawa, A. Ishibashi, K. Akimoto and Y. Mori, "Refractive indices of ZnMgSSe alloys lattice matched to GaAs", *Appl. Phys. Lett.,* **63**, 2082, (1993).

65. C. Kittel, *Introduction to solid state physics,* Sixth edition, John Wiley & Sons, Inc., New York, (1986).

66. G. P. Agrawal and N. K. Dutta, *Long-wavelength semiconductor lasers*, Van Nostrand Reihnold Company Inc., New York, (1986).

67. C. Shieh, J. Mantz, H. Lee, D. Ackley, and R. Engelmann, "Anomalous dependence of thereshold current on stripe width in gain-guided strained-layer InGaAs/GaAs quantum well lasers", *Appl. Phys. Lett.,* **54 (25)**, 2521, June (1989).

68. N. Nakayama, S. Itoh, T. Ohata, K. Nakano, H. Okuyama, M. Ozawa, A. Ishibashi, M. Ikeda and Y. Mori, "Room temperature continous opetation of blue-green laser diodes", *Electron. Lett.,* **29**, 1488, (1993).

69. F. Prince, T. Mattos, N. Patel, D. Kasemset, and C-S Hong, "Waveguiding, spectral and threshold properties of a stripe geometry single quantum well laser", *IEEE J. Quantum Electron.*, **QE-21 (6)**, 634, (1983).

70. J. Copeland, "Single-mode stabilization by traps in semiconductor lasers", *IEEE J. Quantum Electron.,* **QE-16 (7)**, 721, (1980).

71. P. C. Chow, "Computer solutions to the Schrödinger equation", *Am. J. Phys.,* **40**, 730-734, (1972).

Appendix A

Numerical solution for coupled Schrödinger and Poisson equations

The solution of Poisson equation is based on a standard finite difference method. The boundary conditions are based on the total given charges, e.g. total injected carriers, and a point of zero potential and a certain potential gradient (field value) at another point where the potential and field value can be predicted. The program starts calculation from the point where the field has been defined, then according to this predefined field value, the potential values at the two closest point u_i and u_{i-1} can be obtained. By using a central difference approximation,

$$u_{i+1} = 2u_i - u_{i-1} - (\Delta x)^2 \rho \qquad \text{(A.1)}$$

where the Δx is the distance step. The whole potential profile can be obtained through repeating this procedure.

The solution for the Schrödinger follows the method called Numerov process as described by P. C. Chow[71] and briefly discussed below:

Using a general form of the Schrödinger equation, i.e.

$$\varphi^{(2)}(r) = (V(r) - E)\varphi(r) \qquad . \qquad \text{(A.2)}$$

where $\varphi(r)$ is the electron wave-function, V(r) is the potential and E is the energy eigen-value. The wave-function $\varphi(r)$ is expressed by a Taylor expansion around point r,

$$\varphi(r \pm h) = \sum_{n=0}^{\infty} \frac{(\pm h)^n}{n!} \varphi^{(n)}(r) \quad . \qquad \text{(A.3)}$$

The first derivative can be eliminated easily with all other odd parity terms by considering

as follows:

$$\frac{1}{2}[\varphi(r+h)+\varphi(r-h)] = \sum_{n=0}^{\infty} \frac{h^{(2n)}}{(2n)!}\varphi^{(2n)}(r) \tag{A.4}$$

Further, by differentiating twice,

$$\frac{1}{2}[\varphi^{(2)}(r+h)+\varphi^{(2)}(r-h)] = \sum_{n=0}^{\infty} \frac{h^{(2n)}}{(2n)!}\varphi^{(2n+2)}(r) \tag{A.5}$$

The result is the Numerov recursion formula with an error in the sixth order.

This approach has been implemented in the software package SPS (Appendix B).

Appendix B

Computer program/software used for II-VI device simulation

The following programs/software have been obtained/modified/generated for II-VI device simulation:

Program alloyx2-6.f

- Program to calculate lattice constant and band gap of semiconductor alloys. Bowing parameters are calculated by Hill's methods. Written by Yijun Cai. Last modified Nov. 11, 1993.

Program gns.f

- This program calculates the gain spectra of a ZnSe based SCH SQW laser structure. It is an extension of the following InGaAs/AlGaAs QW laser gain modeling programs.

i) gainspec.f by John Ebner, Oregon State University, 4/11/89

ii) engfind.f by Nu Yu, EEAP/OGI, 12/8/90

Modified for carrier spill-over calculation and amended for II-VI parameters by Yijun Cai. Last modified 8/17/93.

The following assisting programs have been added for data processing of gns.f

Program fdpk.sel

- Automatically searches for peak value in the gain spectra file. Written by Yijun Cai.

Program ctj.c

- Converts carrier density to current density. Written by Yijun Cai.

Program SPS package (Schroe.f etc.)

- Program for self-consistent solution of the coupled system of Schrödinger and Poisson equations for a single carrier (electron) one-dimensional domain. Originally written by Claus Fischer, and Cristiano Sala (Institute for Microelectronics, Technical University Vienna, Austria), and Ralf Deutschmann (Siemens Munich, Germany), 1993. The program was originally designed for HEMT device simulation; it was modified for simultaneously calculating electron and hole (two carrier) distributions and applied to QW structure modeling by Yijun Cai. Last modified May 9, 1995. Courtesy of Claus Fischer.

Program MODEIG/II

- For transverse optical field and optical confinement factor calculation. Runing on Macintosh. Coutesy of Gary Evans, Southern Methodist University.

SILVACO ATLAS package (BLAZE, LASER and TONYPLOT)

- For 2-D heterostructure device modeling. BLAZE is used for compound semiconductor heterostructure electronic modeling. LASER is used for DH diode laser modeling. TONYPLOT is used for data plot.

Appendix C Major material properties of wide-band-gap compounds

Table 1: II-VI Compounds

	Str.	Static and dynamical lattice parameters		Band structure parameters				Bonding ionic [3] %	Ref
		a [Å]	c_{ik} [10^{11} N m^{-2}]	E_g [eV] at T [K]	m [m_0]	Luttinger parameter	$dE_{g,dir}/dT$ [$meVK^{-1}$]		
BeS	ZB	a: 4.865		$E_{g,dir}$: 6.10 calc. $E_{g,ind}$: 4.17 calc. $E_{g,opt}$: < 5.5				22	[1]
BeSe	ZB	a: 5.139		$E_{g,dir}$: 4.73 calc. $E_{g,ind}$: 3.61 calc. $E_{g,opt}$: 4...4.5				19	[1]
BeTe	ZB	a: 5.625		$E_{g,dir}$: 1.45 calc. $E_{g,ind}$: 2.89 calc. $E_{g,opt}$: 2.7				9	[1]
MgS	ZB	a: 5.62 *5.635 est.*		$E_{g,dir}$: 4.5 at 77				35	[2], [3]
MgSe	ZB	a: 5.89 *5.866 est.*		$E_{g,dir}$: 3.6 at 77				30	[2], [3]

Table 1: II-VI Compounds

	Str.	Static and dynamical lattice parameters		Band structure parameters				Bonding ionic [3] %	Ref
		a [Å]	c_{ik} [10^{11} N m^{-2}]	E_g [eV] at T [K]	m [m_0]	Luttinger parameter	$dE_{g,dir}/dT$ [$meVK^{-1}$]		
MgTe	ZB	a: *6.28 est.*		$E_{g,dir}$: 3.3 at 300				19	[4]
ZnS	ZB	a: 5.410 *5.427 est.*	c11: 9.81 c12: 6.27 c44: 4.483	$E_{g,dir}$: 3.78 at 19 3.68 at 295	m_n: 0.34 0.18 4 $m_{p,h}$: 1.76 $m_{p,l}$: 0.23		-0.45	19	[1], [3]
	WZ	a: 3.822 c: 6.260		$E_{g,dir\|\|}$: 3.74 ...3.78 at 300 $E_{g,dir\perp}$: 3.78 ...3.87 at 300	m_n: 0.28 $m_{p\|\|}$: 1.4 $m_{p\perp}$: 0.49				

Table 1: II-VI Compounds

	Str.	Static and dynamical lattice parameters		Band structure parameters				Bonding ionic [3] %	Ref
		a [Å]	c_{ik} [10^{11} N m^{-2}]	E_g [eV] at T [K]	m [m_0]	Luttinger parameter	$dE_{g,dir}/dT$ [$meVK^{-1}$]		
ZnSe	ZB	a: 5.668 *5.658 est.*	c11: 9.00 c12: 5.34 c44: 3.96	$E_{g,dir}$: 2.82 at 10 2.70 at 295	m_n: 0.13 ...0.17 m_p: 0.57 ...0.75	γ_1: 4.3 γ_2: 1.14 γ_3: 1.84	-0.455	15	[1], [3]
	WZ	a: 4.003 c: 6.540		$E_{g,dir}$: 2.834 at 300 $E_{g,dir\perp}$:2.79 at 300					
ZnTe	ZB	a: 6.10 *6.074 est.*	c11: 7.13 c12: 4.07 c44: 3.12	$E_{g,dir}$: 2.394 at 1.6 2.28 at 293	m_n: 0.13 m_p: 0.6	γ_1: 3.9 γ_2: 0.83 γ_3: 1.30	-0.28	6.5	[1], [3]
CdS	ZB	a: 5.825 *5.82 est.*		$E_{g,dir}$: 2.50	m_n: 0.14 m_p: 0.51			15	[1], [3]
	WZ	a: 4.136 c: 6.714							

Table 1: II-VI Compounds

	Str.	Static and dynamical lattice parameters		Band structure parameters				Bonding ionic [3] %	Ref
		a [Å]	c_{ik} [10^{11} N m^{-2}]	E_g [eV] at T [K]	m [m_0]	Luttinger parameter	$dE_{g,dir}/dT$ [$meVK^{-1}$]		
CdSe	ZB	a: 6.052 *6.05 est.*		$E_{g,dir}$: 1.9 calc.	m_n: 0.11 m_p: 0.44 calc.			12	[1], [3]
	WZ	a: 4.300 c: 7.011							
CdTe	ZB	a: 6.482 *6.466 est.*	c11: 5.33 c12: 3.65 c44: 2.04	$E_{g,dir}$: 1.606 at 2 1.49 at 300	m_n: 0.09 $m_{p,h}$: 0.72 ...0.8 4 $m_{p,l}$: 0.12			4	[1], [3]
CaS	ZB ?	a: *6.2 est.*		$E_{g,dir}$: *4.1*				43	

Table 2: III-V(Nitride)

Subs-tance	Struc-ture	Static and dynamical lattice parameters		Band structure parameters		Bond-ing ioni [3] %	References
		a [A]	c_{ik} [10^{11} N m^{-2}]	Eg [eV] at T [K]	m [m_0]		
BN	ZB	a: 3.6157		$E_{g,dir}$: 14.5 at RT $E_{g,ind}$(X) : 6.4(5) at RT	m_n: 0.752 $m_{p,h}$: 0.375 0.926 $m_{p,l}$: 0.150 0.108	22	[1], [3]
AlN	ZB	a: 4.37 *4.53 est.*		$E_{g,dir}$: *6.18 at RT*		43	[5]
	WZ	a: 3.11 c: 4.98		$E_{g,dir}$: 6.2 at 300			[1], [3]
GaN	ZB	a: *4.53 est.*		$E_{g,dir}$: *3.34 at RT*		39	[5]
	WZ	a: 3.160 ...3.190 c: 5.125 ...5.190		$E_{g,dir}$: 3.503 at 1.6 3.44 at 300	m_n: 0.27 m_p: 0.8		[1], [3]

Table 2: III-V(Nitride)

Subs-tance	Struc-ture	Static and dynamical lattice parameters		Band structure parameters		Bond-ing ioni [3] %	References
		a [A]	c_{ik} [10^{11} N m^{-2}]	Eg [eV] at T [K]	m [m_0]		
InN	ZB	a: *4.94 est.*		$E_{g,dir}$: *1.79 at RT*		34	[5]
	WZ	a: 3.5446 c: 5.7034		$E_{g,dir}$: 2.11 at 78 1.89 at RT	m_n: 0.12 $m_{p,h}$: 0.5 $m_{p,l}$: 0.17		[1], [3]

Reference

1. Landolt-Börnstein : Numerical Data and Functional Relationships in Science and Technology, New Series III/22a, (1992).
2. H. Okuyama *et al.*, J. Crystal Growth **117**, 139-143 (1992).
3. L. Pauling, *The nature of chemical bond*, Cornell University Press, 1960.
4. S. G. Park *et al.* , *J. Electrochem. Soc.* **118**, 979 (1971)
5. All the data in italic are estimated by Yijun Cai.

Vita

Yijun Cai was born in Huhehot, Inner Monglia, China on October 26, 1964. He attended Peking University in Beijing, China, and received the degree Bachelor of Science in June 1986. Subsequently, he joined the Institute of Aeronautical Material Research, Beijing, as an engineer. His duty includes material characterization and alloy diffusion study by means of electron beam microprobe analysis.

In January 1991, he began his graduate studies at the Oregon Graduate Institute of Science & Technology. He received the degree Master of Science in Electrical Engineer in January 1994. Continuing at the same institution, he worked towards his Ph.D and completed all requirements for the degree Doctor of Philosophy in Electrical Engineering in August 1995.

His research interests are high speed semiconductor device/circuit design and simulation, optoelectronics and optical communication.

He is leaving to accept a position of senior design engineer at Vitesse Semiconductor Corporation, Sunnyvale, California.

Publications/Presentations:

1. Yijun Cai and Reinhart Engelmann, "Design of Novel Blue/Green Diode Laser Based on MgZnSeTe alloy", *Solid-State Electronics*, **38 (3)**, 735, (1995)

2. Yijun Cai and Reinhart Engelmann, "Device Physics of ZnS/Si Heterojunction Transistor", *Proceedings of the Oregon Academy of Science*, **XXX**, 60 (53nd Annual Meeting of OAS, 26 Feb 1995).

3. Yijun Cai and Reinhart Engelmann, "Reduction of threshold current density of CdZnSe/MgZnSSe blue-green quantum well diode lasers", *CLEO'94 Technical Digest Series Volume 8*, 221, Anaheim, CA, May 1994, paper CWH24

4. Yijun Cai and Reinhart Engelmann, "Numerical modeling of injection induced carrier confinement in quantum well (QW) structures", *Proceedings of the 3rd International Workshop on Computational Electronics*, 314-317, (Portland, OR, May 1994.)

5. Yijun Cai and Reinhart Engelmann, "Proposal of novel blue-green diode laser based on MgZnSeTe alloys", *IEEE/LEOS 1993 Summer Topical Meeting Digest on Visible Semiconductor Lasers*, 11, (July 21, 1993.)

6. Y. Cai, R. Engelmann and R. Raghuraman, "Simple model for carrier spill-over in quantum-well lasers consistent with local charge neutrality", *OSA 1992 Annual Meeting Technical Digest*, 23, (September 20-25, 1992.)